Organic spin valves: hole injection from ferromagnetic materials into tris-8-hydroxyquinoline (Alq_3) in the presence of interface states

by

Hongtao Zhang

School of Physics and Astronomy

Queen Mary, University of London

Supervisor – Dr. Alan Drew

Prof. William Gillin

Dr. Theo Kreouzis

July 2014

Submitted for the degree of Doctor of Philosophy

Declaration

I declare that all the work contained within this thesis is accomplished by myself during my study at Queen Mary University of London.

Hongtao Zhang

Abstract

This thesis presents the result of the charge carrier injection and the subsequent transport from ferromagnetic material into organic semiconductor in the Alq_3 based organic spin valves.

In order to study the dominant charge carrier polarity in the Alq_3 based spin valves, a number of single (Alq_3) layer and double (Alq_3 and *N*,*N*'-bis(3-methylphenyl)-*N*,*N*'-diphenylbenzidine (TPD)) layer organic semiconductor diode devices are constructed using both conventional electrode materials as well as ferromagnetic electrodes. Single layer devices are characterised by time of flight (ToF) and dark injection (DI) transient techniques with or without ferromagnetic anodes. Double layer devices are characterised using current-voltage-luminescence (j-V-L) measurements with or without ferromagnetic cathodes. Despite Alq_3 being considered an electron transport material, we measure long range hole transport within the devices with matched electron and hole mobility at large electric fields. The substitution of a conventional Al cathode with a ferromagnet drastically suppresses electroluminescence in double layer devices, due to poor electron injection from the large work function ferromagnet.

DI measurements using a ferromagnetic anode display characteristic charge trapping consistent with the presence of hybridized interface states (HINTS) between anode and organic semiconductor. The temperature dependent DI and ToF measurements demonstrate a reduced hole injection barrier in the presence of the HINTS in the ferromagnetic/organic interface that enables Alq_3 based organic spin valves operate at small bias. We conclude that the dominant charge carriers in Alq_3 based spin valves are holes, contrary to conventional wisdom, and that hole injection under small bias conditions is aided by HINTS.

Acknowledgements

Firstly, I would like to express my sincere and deep thanks to all my supervisors: Dr Alan Drew, Prof. William Gillin, and Dr Theo Kreouzis. I am thankful for their continuously support and valuable expertise during all the stages of my PhD study. Without their excellent guidance, this thesis would not have been completed.

I would also like to thank and acknowledge Mr Geoff Gannaway, Dr Ignacio Hernadez, Dr Pratik Desai and Dr Ken Scott for their valuable time for helping me with using and fixing the experimental facilities. I would not run my experiments so smoothly without their prompt help.

Many thanks to my colleagues and friends I have worked with at different times in Queen Mary University of London Maureen Willis, Nicola Rolfe, Filippo Boi, Zhe, Li, Carlos Aristizabal, Yu Peng, Huanqing Ye, Shuo Han, Ke Wang, Haizhou Lu, Hang Gu and Phil Baker for all your help and the precious time we spent. I would like to especially thanks to my colleague and previous flat mate Sijie Zhang for his help in both accommodation and research at the beginning of my PhD.

I would also like to thanks to my parents and the rest of my family who have been incredibly supportive to my PhD study. I am thankful to the China Scholarship Council (CSC) for funding my PhD studentship.

Last, but most importantly, I have to thanks my beloved wife, Sai Yang, for her understanding and patience through this time of my life.

Contents

List of figures

List of Publications

- **H.T. Zhang**, P. Desai, Y.Q. Zhan, A.J. Drew, W.P. Gillin, and T. Kreouzi, The importance of holes in aluminium tris-8-hydroxyquinoline (Alq3) devices with ferromagnetic contacts, Applied Physics Letter **104**, 013303 (2014)
- **H.T. Zhang**, S. Han, P. Desai Y.Q. Zhan, W. Li, W. Si, A.J. Drew, W.P. Gillin, S.J. Zhang and T. Kreouzis Ferromagnetic-organic interfacial states detected by transient conductivity and their role on low voltage current injection in organic spin valves, Applied Physics Letter, in press.
- A. Droghetti, S. Sanvito, **H.T. Zhang**, M. Wills, A.J. Drew, and W. P. Gillin. Electronic and magnetic properties of the interface between metal-quinoline molecules and cobalt, Physics Review B, **89**, 094412 (2014)
- N. A Morley, A. J. Drew, **H. Zhang** and M. J. R. Gibbs Study of the magnetic-organic interface in organic spin-valves, Appl. Surf. Sci. **313** (0), 850 (2014).
- **H.T. Zhang,** S. han, S.J Zhang, P. Desai, T. Kreouzis, W.P. Gillin and A.J. Drew, Bias Dependent of Magnetoresistance in organic spin valves, in preparation

Chapter 1 Background and introduction

1.1 Organisation of this thesis

This work is devoted to the understanding of charge carrier injection and subsequent transport from ferromagnetic material (FM) into organic semiconductors (OSC) in organic spin valves (OSVs). The main topics of interest are the electronic properties of FM/OSC interface and the charge carrier transport nature in the bulk of OSC, namely，which type of charge carriers dominate and how charge carriers are injected transported and extracted. The FMs used in this thesis are transition metals and their alloys such as Co, Fe and NiFe. The OSC chosen in this work is tris (8-hydroxyquinolinato) aluminium (Alq_3) a typical small molecular solid. Several complementary techniques have been used and summarized below.

In this chapter, some basic understandings of OSC and OSC based devices，such as, organic light emitting diodes (OLED) and OSVs, are given. Following this, the disorder model for carrier transport in OSC and a literature review of organic spintronics are introduced. This chapter is intended as an overview of some of the physics investigated in this thesis and not as an in-depth review.

Chapter 2 contains the experimental methods used in this thesis covering the whole device fabrication process and subsequent characterizing techniques. The main characterizing methods used in this thesis are mobility measurements time of flight (ToF) and dark injection (DI).

Chapter 3 shows the experimental results for OSC devices, which contains current-voltage-luminescent characterisation results for OLEDs with ferromagnetic cathode. ToF and DI measurements results on organic spin vale like devices are included.

Chapter 4 contains temperature dependent DI and ToF results for the devices used in chapter 3 to investigate the interface states in the devices.

A summary of the conclusions for the whole thesis and discussion of possible future work can be found in chapter 5.

1.2 Introduction to organic semiconductors (OSCs)

Organic semiconductors are organic materials with semi-conducting properties. Different from inorganic semiconductors, they are generally undoped and intrinsically semiconducting. Their semiconducting nature originates from a common π-conjugate chemical structure, in which the highest energy electrons are delocalized, forming free electrons for conducting over the entire extent of the π-conjugation [1]. OSC based devices are showing promising applications due to their low cost, low weight, mechanical flexibility, chemical tunability and bottom up fabricating properties [2].

Properties of the OSC and typical OSC devices organic light emitting diodes (OLEDs) and organic spin valves (OSVs) are introduced in this section.

1.2.1 Organic molecules and organic solid

OSCs are categorized into two groups, small molecules and polymers. Thin films of small molecules with low molecular weight are normally fabricated using vacuum evaporation techniques, while polymers are prepared by spin-coating, screen printing, drop casting, etc. [3]. This thesis focuses on a typical small molecule OSC tris-8-hydroxyquinoline (Alq_3). The molecular diagram of Alq_3 and the benzene rings it consist of are shown in figure 1.1. The benzene structure well explains the semiconducting behaviour of OSCs.

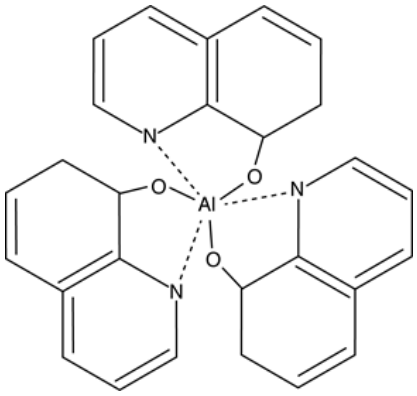

Figure 1.1： Molecular diagram of Alq_3

The benzene ring is made of six carbon atoms and each carbon atom has six electrons, in the ground state (figure 1.2), occupying *1s*, *2s*, and *2p* orbitals. The *s* orbitals are

spherically symmetrical, while the 2*p* orbital shaped like dumbbells originate at right angles to each other, labelled as $2p_x$, $2p_y$ and $2p_z$. In order to form three bonds between carbon atoms in benzene, the carbon requires more unpaired electrons. Hence, one electron promoted from the 2s state to the empty $2p_z$ state (excited state in figure 1.1). In order to from the trigonal planar structure seen in the bonding, by mixing the 2s orbital with two *p* orbitals, three equivalent sp^2 hybridized orbitals are formed. As shown in figure 1.3a, the three sp^2 orbitals are at the angle of 120°to each other on one plane, and the p_z orbital is left perpendicular to them. The two carbon atoms can then be bonded by formation of an orbital overlap of two sp^2 orbitals (figure 1.3b). This bond is called σ bond, which has a quite large energy gap between unoccupied and occupied orbitals (above 8eV). However, as shown in figure 1.3b and c, the p_z orbitals form additional π bonds. These bonds have much smaller energy difference between occupied and unoccupied orbitals (1.5 to 3 eV between π and π* orbitals respectively).

In the case of benzene rings, as shown in figure 1.3d and e, each carbon atom form three strong hybridized σ bonds with the overlapping of sp^2 bonds; two with neighbouring carbon atoms, and one with a singular hydrogen atom that sits in the same plane. The remaining p_z orbitals, which are perpendicular to the benzene ring overlap and form relatively weak π bonds or π-conjugation, where the unpaired electrons are delocalized and can move freely form one orbital (figure 1.3f). Therefore, the highest occupied orbital molecular orbital (HOMO) and the lowest unoccupied

orbital (LUMO) is analogous to the valence and conduction band of inorganic semiconductors.

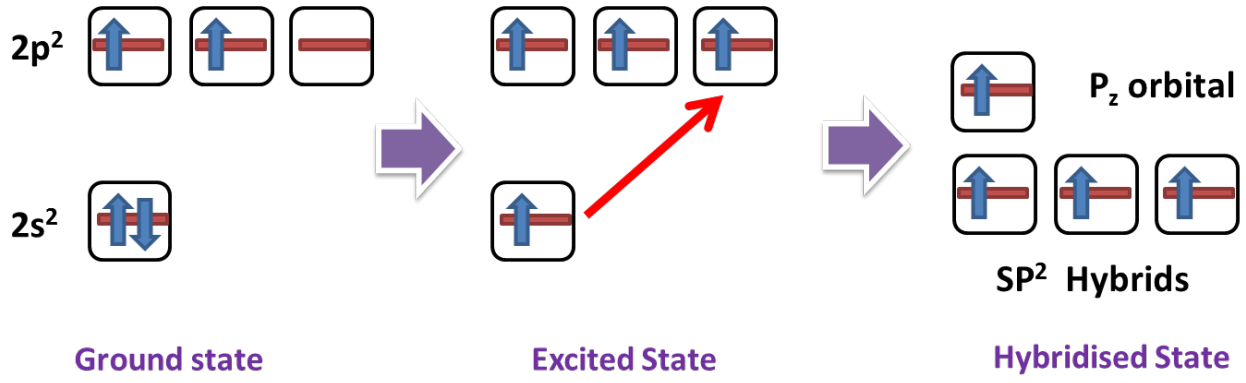

Figure 1.2: Hybridisation process

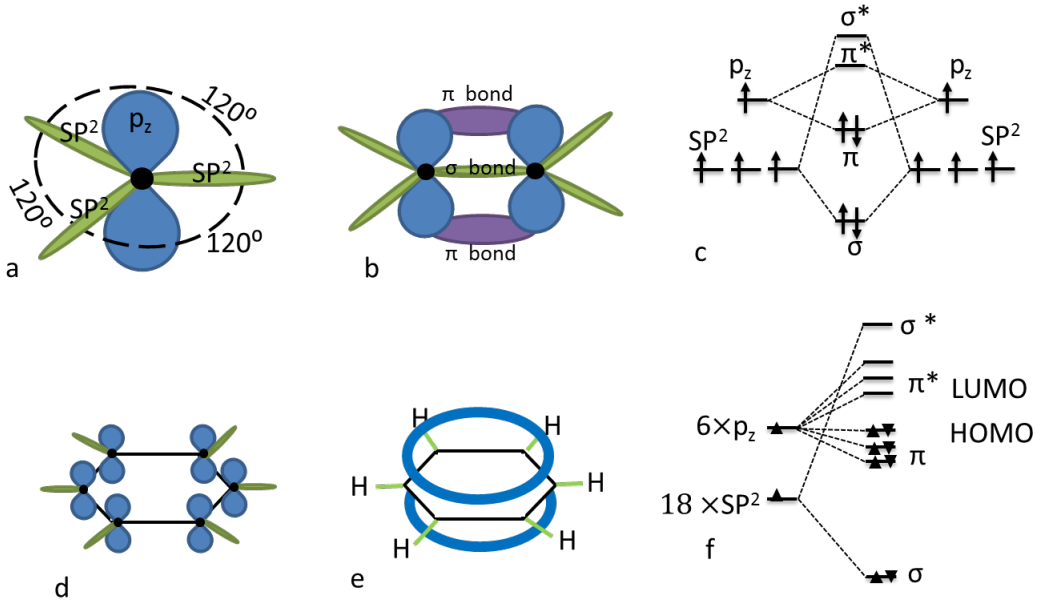

Figure 1.3: (a) sp^2 Hybridised orbitals of a carbon. (b) Orbitals and bonds for two sp^2 hybridised carbon atoms. (c) Scheme energy structure of two sp^2 hybridised carbon atoms. (d) Hybridised orbitals of carbon in a benzene ring. (e) π orbitals of benzene. (e) Scheme of the energy structure of benzene.

In OSC solids, the molecules are bonded with π orbitals and interact by the weak van der Waals interaction. Figure 1.4 explains the formation of an OSC solid starting from a single atom in perspective of electronic structures. The potential well of a single hydrogen atom is shown in figure 1.4a; various atomic orbitals are formed in this well, an electron occupying the lowest 1s orbital. Above the potential well is the vacuum level (VL), where electron can escape from the atom. Figure 1.4b shows the electronic structure of an OSC molecule or molecule group that is formed by the atomic nuclei and other electrons. The wells of the nuclei are merged forming a broad well, where deep atomic orbitals (σ orbitals) are still localized as core levels. The top of the well is also the VL, and orbitals in between are delocalized molecular orbitals (π orbitals). When molecules come together to form an OSC solid, the electronic diagram becomes like figure 1.4c. Unlike inorganic semiconductors, where the formation of energy bands is due to atomic orbital splitting and overlapping, HOMO and LUMO are normally localized in each molecule, and cannot be regard as forming the band-like structure. The HOMO-LUMO gap is relatively small, typically less than 3eV, which contribute to the semiconducting behaviour. Transition of excited electrons from the LUMO to HOMO yields luminescence in the visible range of light. This is the luminescent principle for light emitting diodes (OLEDs) and will be discussed in next section. The electronic diagram of OSC solids is often simplified to figure 1.4d. It is worth noting that due to Pauli exclusion principle, one molecular state can only hold two electrons of opposite spin orientation. Therefore, the excited electrons or holes in the LUMO or HOMO with different combinations of spin

orientations form exitons, which are categorized into two types, namely singlets and triplets. And the light emitting of OLEDs is a result from singlets recombination.

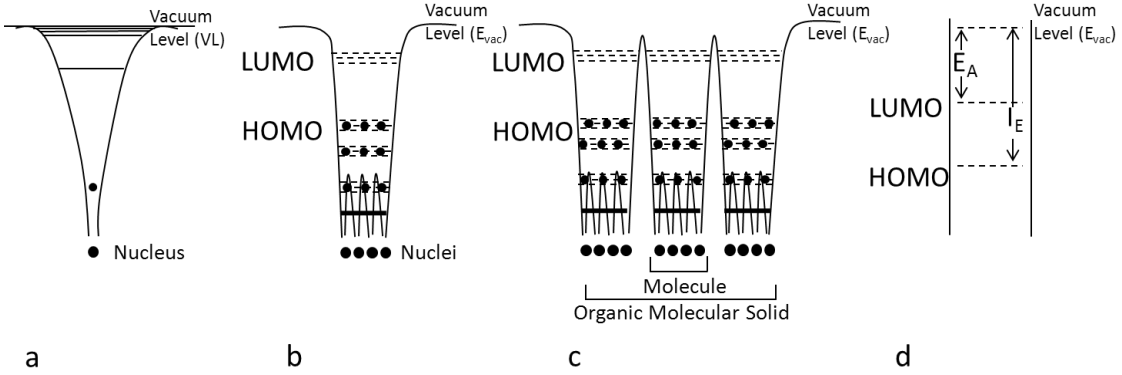

Figure 1.4: Electronic structures represented with potential wells

(a) Hydrogen atom. (b) Atomic molecule. (c) Organic semiconductor solid

1.2.2 Organic light emitting diodes

The modern OLEDs are based on small molecule organic materials and polymers, which are first demonstrated by Tang *el al*.[4] and Burroughes *et al*.[5] As shown in figure 1.5a, a typical OLED is a sandwich of one or more semiconducting organic materials between two electrodes. The operation of the device involves the carrier injection, carrier transport, exiton formation and recombination to emit light.

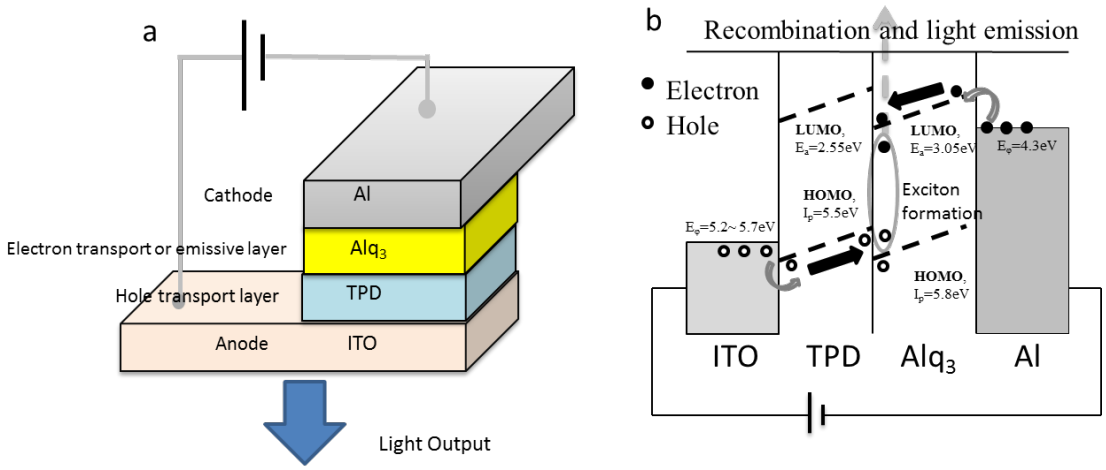

Figure 1.5: Schematic of modern OLED and energy levels

(a) Shows the schematic of a typical Alq_3 based thin film OLED. (b) Shows the energy diagram of the OLED with applied electric bias

Here we use indium oxide (ITO) as the anode, *N*,*N*'-bis(3-methylphenyl)-*N*,*N*'-diphenylbenzidine (TPD) as the hole transport layer, Alq_3 as the electron transport layer and aluminium (Al) as the cathode (figure 1.5 a). When forward bias is applied on the device, holes are injected from ITO to the HOMO of TPD and electrons are injected from Al to the LUMO of Alq_3 by overcoming the energy barriers between them. For the purpose of increasing the work function of ITO and reducing the hole injection barrier, ITO is usually treated with oxygen plasma before use, and it is been found that the work function of ITO was increased to 5.7eV after the treatment [6-9]. Apart from Al, low work function metals or alloys such as Li, Ca, Mg and Mg:Ag are wildly used as the cathode to match the LUMO of electron transport layer. In order to lower the work function of the cathode, a thin insulation layer (LiF) is usually used [10, 11] although the mechanism responsible for the

improved electron injection is not properly understood. It is worth knowing that energy level diagram present in figure 1.5b is idealized, in reality; the electrode surface topography is not perfect. The occurrence of clustering, oxidation, diffusion of the electrode into the organic layer [12], band bending [13], and dipole interactions, all of which will contribute to discontinuity of the vacuum level over the interface between the electrode and the organic material [14]. More details about energy level alignment and interfacial electronic structures at organic/ metal interfaces will be discussed in section 2.4.

1.2.3 Organic spin valve (OSV)

Compared with an OLED, a spin valve has a similar sandwich structure, two ferromagnetic electrodes separated by a non-magnetic spacer. Once forward bias is applied, spin polarized charge carriers can be injected into the non-magnetic spacer. In fact, both OLEDs and OSVs are organic-metal hybrid systems, and the non-magnetic spacers are organic semiconductors.

As shown in figure 1.6, the magnetic orientation of the two electrodes can be changed from parallel to antiparallel configuration by an external magnetic field [2]. Usually in spin valves the electronic resistance is higher in antiparallel configuration than that in parallel configuration. This effect is known as the giant magnetoresistance (GMR) effect or tunnel magnetoresistance (TMR) effect, which depends on how spin

polarized charge carriers transport, by tunnelling or by hopping. Both GMR and TMR are spin valve effect, which will be discussed in section 1.4.

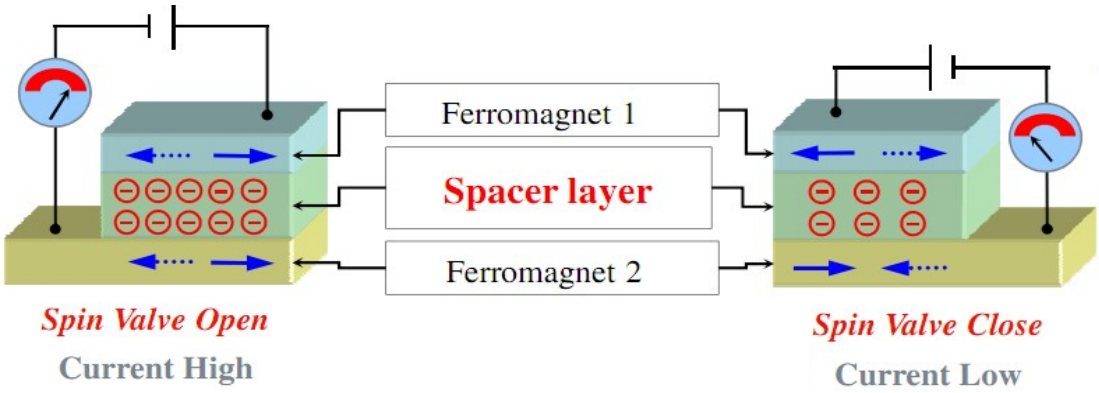

Figure 1.6: Schematic diagram and function of a spin valve, the amount of "-" indicates the current density.

1.3 Carrier injection and transport

For electrical applications of OSCs, OLEDs or OSVs, metal electrodes are needed to inject and extract charges carriers into and from the OSC spacer(s). As in traditional inorganic semiconductors, the energy level alignment of metal/OSC interface, and how charge carriers are injected and transported in OSCs, are critical for OSC devices.

1.3.1 Energy level alignment

Charge carrier injection from metal into semiconductors depends on the energy barrier at metal-semiconductor interface. Ideally, this barrier is the difference between

the Fermi level of the injecting metal and the energy band (HOMO or LUMO for OSCs) of the semiconductors, where metal and semiconductor share an aligned vacuum level and there are no interference states between metal and semiconductor layer. However, this is not often the case. Given different Fermi level of metal and semiconductors, in equilibrium, to form a uniform Fermi level, there must be electron transfer or electron cloud redistribution on the metal/organic interface. In the case of metal-inorganic semiconductor contact, if the metal has a lower Fermi level, electrons will diffuse from semiconductor to metal, and the holes will be left behind forming space charging zone in the semiconductor. The charges in the space charging zone will bend the energy band and form the Schottky Barrier [15](Figure 1.7). For OSCs, the situation is more complicated. The energy gap between LUMO and HOMO is usually between 1.5eV~3eV [13], which is much higher than energy of thermal motion in room temperature (26meV), and normally without doping, electrons on the LUMO and holes on the HOMO are negligible. As a result, the formation of the Schottky Barrier seems rare. However, in the real system, a few atomic-layers thick dipole or interface states layer were found using the ultraviolet photoelectron spectroscopy (UPS) method [16], when the organic film was deposited on the metal substrate. The interface states or dipoles cause an energy shift between metal/OSC vacuum levels, which form a Schottky like barrier (Figure 1.8).

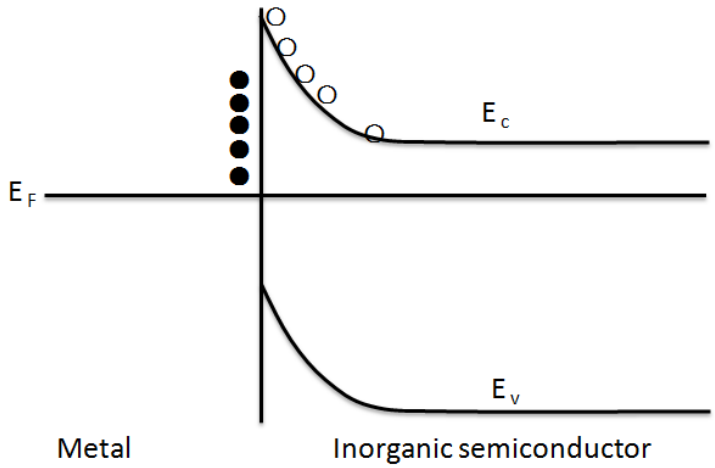

Figure 1.7: The schematic of Schottky barrier for metal/inorganic semiconductor conduct (●electron; ○hole).

The interface states have various origins such as electron transfer and redistribution of electron cloud [17, 18], one of which is chemical absorption that corresponds to the formation of chemical bonds and/or defects between the OSC and metal. When metal is vacuum deposited on the surface of OSC, the defects or organometallic complex will be introduced, which act as occupied or unoccupied electronic (hole trap or electron trap) states in the metal/OSC interface. One typical example is the reaction between Al or Mg and Alq_3 that has been extensively studied. This result in the formation of interface states that pin the Fermi level in the upper part of the Alq_3 gap reducing the electron injection barrier (figure 1.6b) [19-22]. Such reaction can also be found when doing molecular evaporation on top of metals [21]. In the case of ferromagnetic material/OSC interface, similar interface states are found to be introduced and will be discussed in section 1.4.3.

As shown in figure 1.8, the barrier height, Φ_{Be} and Φ_{Bh} represent how difficult it is to inject electrons and holes from the metal contact to the OSC. So if we know the energy structure and energy level alignment of both metal and OSC, we can easily discriminate which type of charge carriers should dominate the injection. Unfortunately, however, the determination of energy-level diagrams in OSCs seems more complex than the metal contact. The energetic position of the HOMO is usually experimentally detected by optical method such as UPS. The position of LUMO is subject to much more uncertainty than that of HOMO, as it is difficult to use optical method to precisely detect the LUMO position. The methods that are commonly used to determinate LUMO of OSC monolayer or thin film are inverse photoemission (IPES) [23], two-photon photoemission (2PPE) [24, 25], and measurement of the standard reduction potential in an electrochemical cell [26]. However, the values obtained by these methods differ as much as 1eV[27].

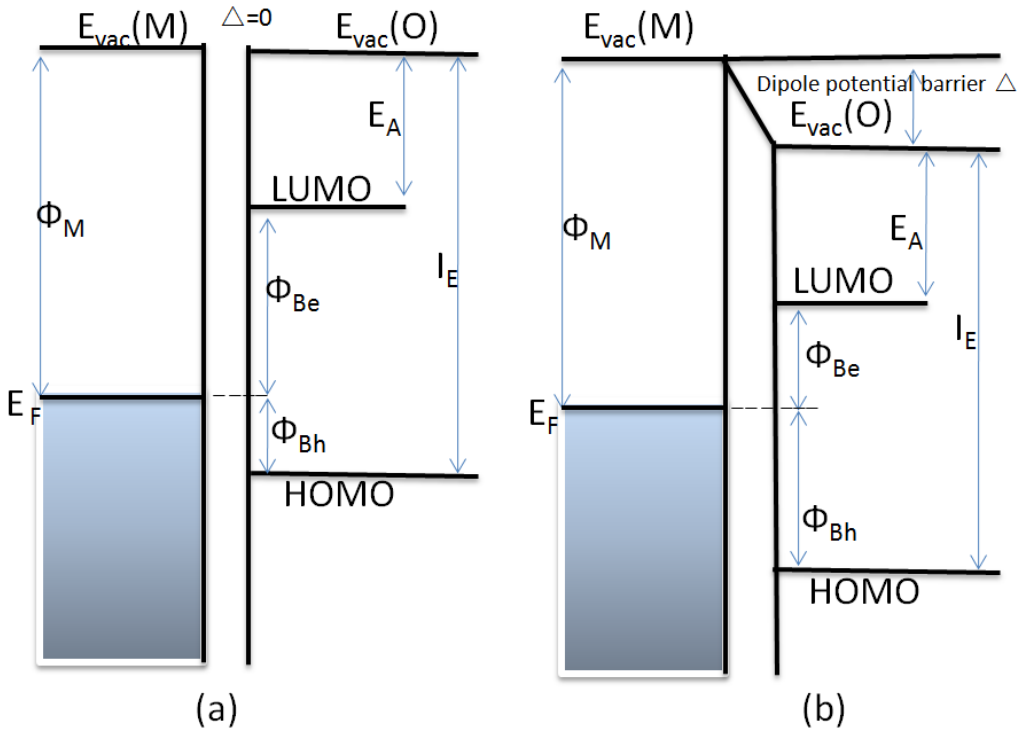

Figure 1.8: Schematic of interface energy level (a) without the dipole layer. (b) with the dipole layer

$E_{vac}(M)$ or $E_{vac}(O)$ is the vacuum level of metal or OSC, E_A or I_E is electroaffinity or ionization energy of OSC. Φ_{Be} or Φ_{Bh} is the energy barrier for electron injection or hole injection. Δ is the energy barrier generated by dipole layer

1.3.2 Carrier injection and transport

Ideally, for OSC devices, when applying an electric field, charge carriers can overcome the metal/organic energy barrier (Φ_{Be} or Φ_{Bh} in figure 1.8) and inject into organic layer. So the current in OSC devices is limited by two factors, carrier injection and carrier transport. The barrier heights observed at the metal/organic contacts are usually high （>1eV） which limit the efficient charge injection at the

contacts. With the introduction of interfacial dipoles or a correctly chosen contact material, one can decrease the barrier height and achieve the ohmic contact. In this case, the current of the device is only limited by the transport properties of the OSC, resulting a space charge limited current (SCLC). The relationship is given by Mott-Gurney Eq. [28], where, ε is the electric permittivity, μ is either electron or the hole mobility, and V is the voltage across the device of thickness L

$$J_{SCLC} = \frac{9}{8}\mu\varepsilon\frac{V^2}{L^3} \qquad 1.1$$

It is worth noting that this equation is only valid when only one type of charge carriers dominates the injection and transport, and the mobility is assumed to be independent of the electric field.

Transport of charge carriers in OSCs is quite different from that in traditional inorganic semiconductors such as Si and Ge [29]. With perfect overlap of their electronic wave functions, it is reasonable to consider that electrons and holes move almost as if they were free, in the band like energy levels. However, like Alq_3, most OSC molecules are weakly bonded with weak Van Der Waals force in π bonds as introduced in section 1.2 [9], and as such with localized charge carriers. Thus, the elementary transport step, known as transport sites, exists as shown in figure 1.7. The number of sites per energy is often assumed to be a Gaussian distribution (the Gaussian model will be discussed in next section). With applied electric field, the

injection of carriers into OSCs is a thermally assisted tunnelling across the inorganic/organic interface, followed by carrier diffusion into the bulk of the OSC, in terms of a phonon assisted site to site hopping [13](Figure 1.9). Electrons on LUMO and holes on HOMO, hop from molecule to molecule with very low mobility.

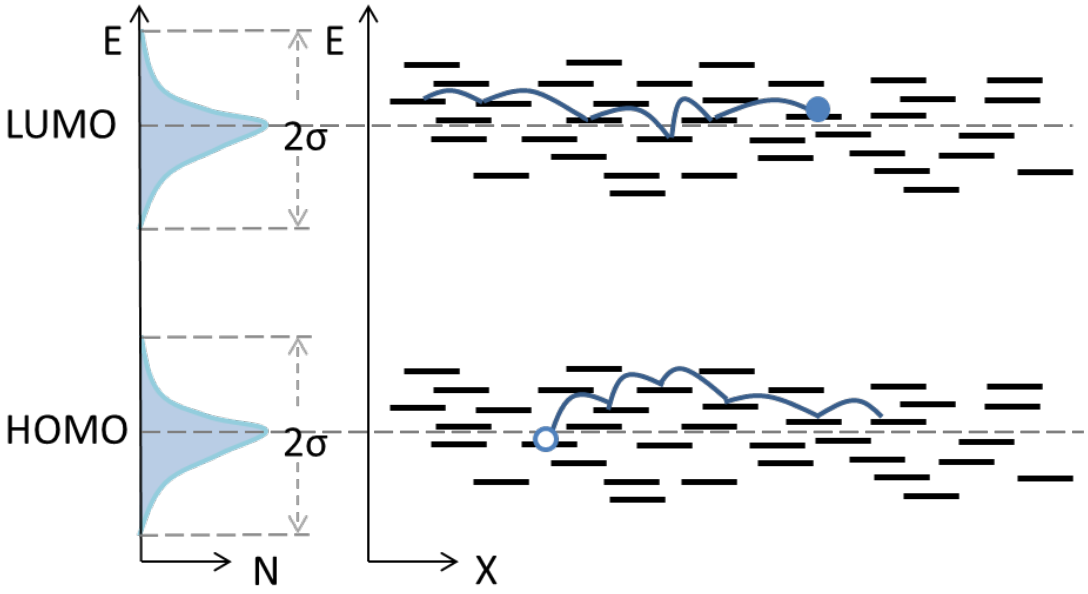

Figure 1.9: Energy site distribution diagram and site to site hoping in OSC solids.

The number of sites per energy follows a Gaussian density of states with the width σ (left). The hopping of the holes on HOMO and electrons on LUMO are illustrated.

1.3.3 The Gaussian disorder model for charge carrier transport

The presence of localized sites put a lot of restrictions on hopping transport of charge carriers in OSCs, in which the models used to describe charge carriers transport in inorganic semiconductors are not valid any more. However, in disordered OSC

systems, it was discovered that the mobility of the charge carrier is normally dependent on electric field and fit well with the so-called Poole-Frenkel relation, which is named after Yakov Frenkel and H.H. Poole in the 1930s [30]. This relation characterises how an electrical insulator can conduct electricity, shown below, where, μ is the mobility of charge carrier, μ_{pf} is mobility pre-factor, β is the Poole-Frenkel coefficient, and E is the applied electric filed

$$\mu = \mu_{pf} \exp(\beta\sqrt{E}) \qquad 1.2$$

This relation is basically describing the reduction of required thermal energy to remove a charge carrier from a localized site (coulomb well) in the presence of increasing applied electric field, so that the charge carrier can move more frequently with a higher mobility.

The Poole-Frenkel behaviour of charge carrier mobility in most disordered OSCs has later been explained in relation to the Gaussian Disorder Model (GDM) that was published in the 1990s by Bassler and co-workers [31]. GDM was developed by Monte Carlo simulation assuming Gaussian distribution of transport site energy E, (figure1.9),

$$g(E) = \frac{1}{\sqrt{2\pi\sigma}} \exp\left(-\frac{E^2}{2\sigma^2}\right) \qquad 1.3$$

implying the localization of all the states. The standard deviation σ is called the disorder parameter, which denotes the width of the Gaussian site energy distribution. Experimental values of σ are in the range of 50-150 meV [31]. Bassler also assumes that the charge carriers can hop between these localized sites according to a Miller-Abraham's equation with hopping rate $K_{ij,}$ where v_0 is pre-factor represents the attempt-to-escape frequency, and Σ is dimensionless overlap parameter that is represent the distribution of inter-site distances in a disordered system, or a Gaussian distribution of spatial disorder, E_i and E_j represents energy on site i and site j.

$$K_{ij} = \nu_0 exp(-\Sigma) \times \begin{cases} exp(-\frac{E_j - E_i}{k_B T}) & if\ E_j > E_i \\ 1 & if\ E_j < E_i \end{cases} \qquad 1.4$$

Once the parameters of Eq.1.3 and 1.4 are determined, an empirical expression of the charge carrier mobility, μ as a function of electric field (E) and temperature (T) was obtained by Mote Carlo simulation, which is shown in Eq. 1.5

$$\mu(T,E) = \mu_0 exp[-(\frac{2\sigma}{3k_B T})^2] exp\{C_0\sqrt{E}[(\frac{\sigma}{k_B T})^2 - \Sigma^2]\} \qquad 1.5$$

In this equation, the mobility pre-factor μ_0 is a hypothetical mobility at infinite temperature and zero electric field and C_0 is simply an empirical constant.

The dispersive transport nature of OSCs is denoted from Eq. 1.5, as the relaxation of charge carriers towards thermal equilibrium starting at an arbitrary point within the

DOS exhibit a logarithmic decay law. The temperature dependent behaviour of disordered OSC system can also been obtained from this equation. Most importantly, as we can see, Eq. 1.5 well explains the typical Poole-Frenkel type behaviour, as the natural log of the charge carrier mobility is proportional to the square root of the applied electric field ($ln\mu \propto \sqrt{E}$). A typical Pool-Frenkel plot in various temperatures is shown in figure 1.10.

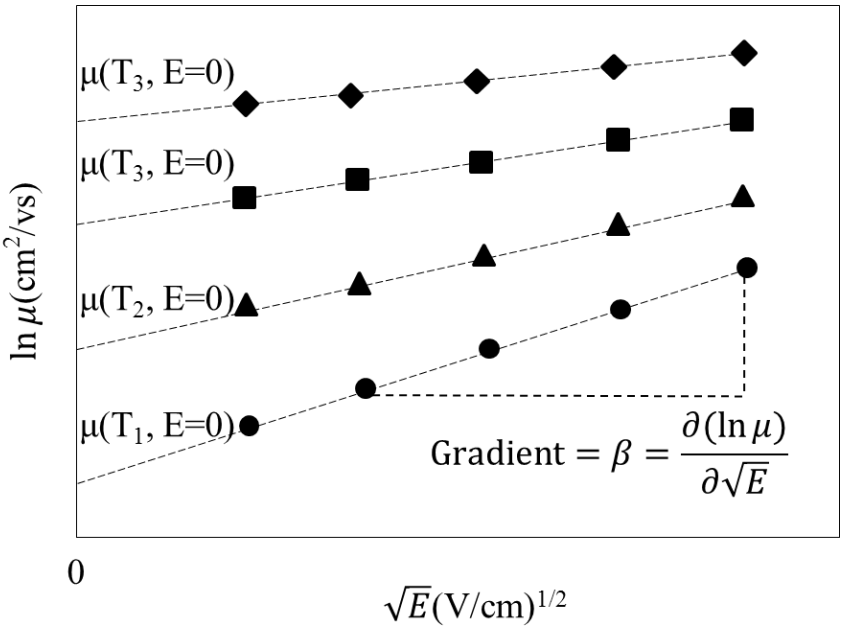

Figure 1.10: Schematic of a Poole-Frenkel plot of charge carriers mobility versus squire root of applied electric field.

The zero field mobility μ(E=0) and the Poole-Frenkel coefficient β can be extrapolated from this plot. The zero field mobility μ(E=0) is not the real mobility at zero field and is a parameter ,

Hence, Eq. 1.5 can be used as a very powerful tool to analyse mobility data. When *E=0*, the zero field mobility of Eq. 1.5 can be depicted as:

$$\mu(T, E = 0) = \mu_0 e^{-(\frac{2\sigma}{3k_B T})^2} \quad 1.6$$

or

$$\ln \mu\,(T, E = 0) = \ln \mu_0 - (\frac{2\sigma}{3k_B T})^2 \quad 1.7$$

As indicated from figure 1.8 and Eq. 1.7, zero field mobility of each temperature is simply intercept at y-axis. So the value of pre-factor μ_0 and disorder parameter σ can be recovered by plotting $\ln \mu\ (E = 0)$ versus $1/T^2$ as shown in figure1.11.

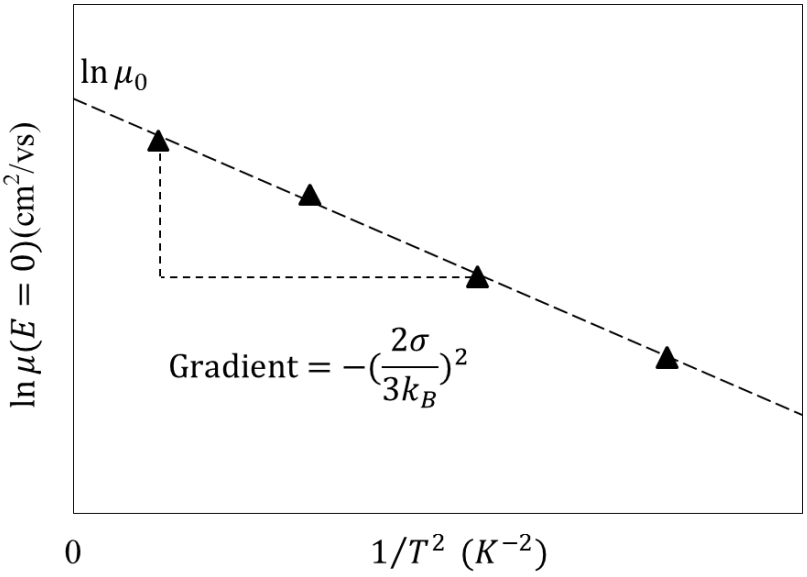

Figure 1.11: Temperature dependent zero field mobility

The Pre-factor μ_0 and disorder parameter can be calculated from this plot.

When fitted the data with linear equation $y=Ax+B$, the intercept B at y-axis refers to $ln\,\mu_0$ and the gradient of the fitted line A is corresponds to $-(\frac{2\sigma}{3k_B})^2$.

In order to get the remaining parameters C_0 and Σ we take the natural log on both side of Eq. 1.5:

$$ln\,\mu = ln\mu_0 - (\frac{2\sigma}{3k_BT})^2 + C_0\sqrt{E}(\left(\frac{\sigma}{k_BT}\right)^2 - \Sigma^2) \qquad 1.8$$

And differentiate with $\sqrt{E}$:

$$\frac{\partial \ln \mu}{\partial(\sqrt{E})} = -\Sigma^2 C_0 + C_0(\frac{\sigma}{k_BT})^2 \qquad 1.9$$

As indicated in Eq. 1.9, $\frac{\partial \ln \mu}{\partial(\sqrt{E})}$ is simply Poole-Frenkel coefficient β mentioned in Eq. 1.2. So the remaining of the parameters can be obtained from the plot of β against $(\frac{\sigma}{k_BT})^2$ as shown in figure 1.12

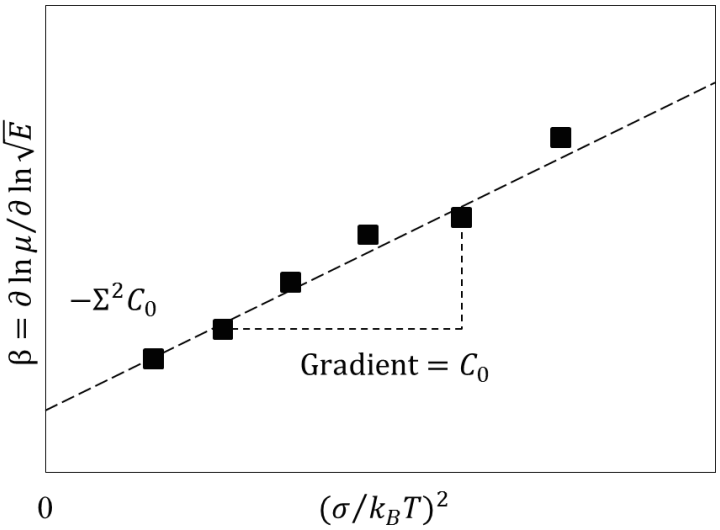

Figure 1.12: A typical plot of β versus $\left(\frac{\sigma}{k_BT}\right)^2$

Overlap parameter Σ_0 and the empirical constant C_0 can be calculated from this plot.

When the data is fitted with linear equation $y=Ax+B$, the intercept B at y-axis refers to $-\Sigma^2 C_0$ and the gradient of the fitted line A is corresponds to C_0.

The GDM also has a few limitations, the main one of which is the discrepancy between simulation and experimental results of charge carrier mobility at low electric field (below $10^5 Vcm^{-1}$), where charge carrier mobility can still have the Poole-Frenkel behaviour, which the GDM simulation failed to predict. Such discrepancy occurs because of the underlying assumption in GDM that no correlation or coupling between neighbouring sites for the Gaussian DOS. However Gartstein and Conwell [32] showed that such an assumption is not entirely true, since adjacent sites should have some level of coupling. Later on, Dunlap and co-workers developed a corrected disorder model (CDM) and resolved this discrepancy [33]. The other drawback of GDM is that it is based on the pure materials and neglects the presence of trapping states in most of OSC systems. Other proposed models are developed by various groups [34-36] trying to include the effect of impurity or charge trapping within the system, which is beyond the scope of this thesis.

1.4 Mobility measurements

Charge mobility (μ) is one of the key parameters in OSCs, which characterize how quickly electrons and holes transport in the material under the applied electric field. Mobility of charge carriers is given by Eq. 1.10, where v_d is the drift mobility, E is the

electric field applied, *d* is the film thickness of the measured sample, *t* and *V* refers to the transit time and applied bias respectively.

$$\mu = \frac{v_d}{E} = \frac{d}{Et} = \frac{d^2}{Vt} \qquad 1.10$$

There are several experimental methods to measure charge mobilites in OSCs. Generally they can be divided in to two types: transient methods, such as time of flight transient (ToF) technique and dark injection (DI) transient and steady state methods such as field transistor or space charge limited current voltage (SCL-IV) characteristics. In this section, ToF and DI is mainly discussed, other methods will be introduced as well.

1.4.1 Time of Flight

Since firstly introduced by Kepler [37] and Leblance [38] , in 1960s, the time of flight (ToF) technique is widely used to investigate charge transport. One of the advantages of this technique is the capability of selectively measuring the mobility of both electrons and holes. In this method, photo current is generated on one electrode of the sample and transport to the counter electrode under the applied electric field.

A typical ToF experiment setup is shown in figure 1.13a. A reversed bias is applied on a device to provide an electric field but minimise the current injection from

electrodes. Then a short light pulse irradiates one side of the device. By choosing the irradiation electrode (semi-transparent), one can choose the type of photo charge carriers. In figure 1.13a, for instance, the light exposure at the anode creates a thin sheet of electron and hole pairs, where electrons are absorbed by the anode leaving a sheet of remaining holes to traverse across the sample under the applied electric field. The transient photocurrent is monitored with a high-resolution digital oscilloscope.

As shown in figure 1.13b (ii) in the ideal case, the constant photo current will transport through the device and abruptly fall to zero as the sheet of carriers reaches the counter electrode (see figure 1.13b (ii) red line). However in a real situation, this ideal shape will never be observed. Firstly, the absorption depth of the incident light is finite, resulting in a finite thickness of sheet of charges. Secondly, the distribution of drifting charges and the mobility variations are diffusively broadened. As a result, if most of the carriers assumed have similar drift velocities, the observed ToF signals would be like the green curve present in figure 1.13b (ii). This transport is known as non-dispersive transport. In this case, the current remains constant until the frontier edge of the carriers reaches the counter electrode resulting in a plateau of corresponding ToF transient, then the current drops with a typical dropping tail observed in the current transient. This tail is the signature of broadening of charge carrier velocities. In many cases, especially for most of organic materials, the photo generated charge carriers sheet moves with a very broad distribution of drift velocities, where there is no constant current and corresponding plateau in ToF transient, but

only a long drop tail, as the blue line shown in figure 1.13b (ii). This transport is called dispersive transport.

In 1.13b (ii), if the transport of the charge carriers is non-dispersive, the fastest arrival time (t_0) can be deduced from the linear plot of photocurrent versus time. And the average transit time is generally accepted when half of the charge carriers reached the counter electrode at the half of drop tail ($t_{1/2}$). The broad distribution (W) that quantifies the spread of charges can be calculated from

$$W = \frac{t_{1/2} - t_0}{t_{1/2}} \qquad 1.11$$

The corresponding mobility μ can be obtained using Eq.1.10

In the case of dispersive transport, the large broadening of drift velocity of charge carriers in the OSCs is normally due to trapping events. Charge carriers can be captured in shallow or deep trapping states, which tend to have a lifetime ranging from nanoseconds to microseconds. The thermally released trapped carriers will contribute to the photocurrent and result in large spreading of drift velocity of charge carriers [38]. Thus no constant current plateau is observed and no useful information can be observed in the linear plot. In order to analyse such transients, the ToF signal is plotted in a log (current) versus log (time) representation, as demonstrated in figure 1.13(iii). The double logarithmic plot will produce an inflection point with the help of two tangents. This inflection point indicates the fastest arrival time (t_{tran}) of charge

carriers. According to Scher and Montroll's transit-time dispersion model [39], the hopping time distribution function $I(t)$ is proportional to $t^{-(1-\alpha)}$ where the dispersion parameter α is between 0 to 1 before the t_{tran} and between -1 to 0 after t_{tran}. It is worth noting that for dispersive transport the transition time t_{tran} only indicates the fastest arriving time of charge carriers, and no information about average arriving time can be obtained from this kind of transport. The corresponding "fastest" mobility can be calculated from the Eq.1.10 as well.

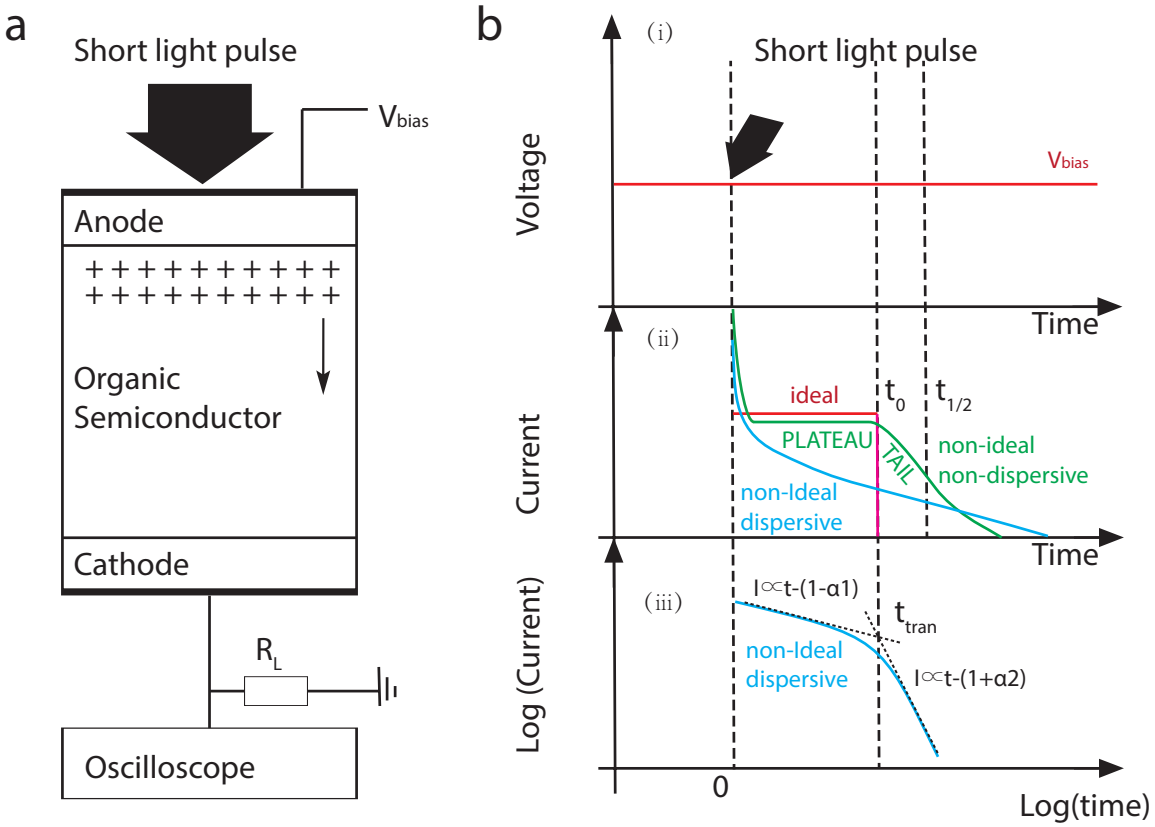

Figure 1.13: Schematic of ToF experimental arrangement and Schematic of the bias and the theoretical and experimental current transients

(a) Schematic of ToF experimental arrangement showing the current generated light irradiation and transport through the device under the applied electric field (providing a current-transient) as a voltage drop across a load resistor, R_L, at the oscilloscope input. ***(b)*** *Schematic of the bias and the theoretical and experimental current transients.*

1.4.2 Dark Injection

The dark injection transient current technique (DI) is one of the other popular techniques used to measure charge carrier mobility in OSCs. It is termed dark injection, as it does not rely on photogenerated charges, unlike the ToF technique. By applying a voltage pulse in forward bias to the sample, and in the presence of one highly injecting (ohmic) electrode, the current flow through the device is recorded as a function of time. This current transient is measured as a voltage across a load resistor on the input of an oscilloscope. The shape of the current transient contains a large amount of information about the charge carrier behaviour, including a characteristic peak, which is related to the transit time of the carriers across the sample thickness. Using the sample dimensions and the applied bias, the carrier mobility can be calculated from this peak time.

Unlike ToF, As shown in figure 1.14, DI relies on ohmic injection contact to sustain a maximum current, the so-called space charge limited current within the sample. In the case of trap free ideal samples, as shown in figure 1.14b, when applying a voltage pulse, charge carriers are injected into the device. Before reaching the steady state current I_{SCLC}, there is an increasing and decreasing of the current density. The first increase of the current is due to the increase of the driving electric field ($E=V/d$), as the gap between the frontier charges and counter electrode (d) decreases (figure 1.14a). However this increasing is limited by the coulombic repulsion from the charges already injected into the sample, which finally forces the injected current

down. Hence the dark current increases at the beginning then drops down until it finally reaches the steady state I_{SCLC}, which result in a turning point. The time (t_{DI}) at this point is called the dark injection peak time, which relates to the time when the front edge of charge carriers reaches the counter-electrode and is a vital element for the mobility calculation.

As the non-uniformity nature of the electric field in space charge limited transport, one can no longer substitute the DI peak time t_{DI} in Eq 1.10 to determine the true mobility. However further analysis shows that, t_{DI} is directly related to the space charge free transit time, t_{tran}, ($t_{DI} = 2(1\text{-}e^{-2/1})\ t_{tran} \approx 0.79\ t_{tran}$)[40, 41], Thus, the mobility can be obtained from Eq. 1.12,

$$\mu = \frac{d^2}{Vt_{tran}} = \frac{0.79d^2}{Vt_{DI}} \qquad 1.12$$

Indeed, the t_{DI} is used to calculate an experimental mobility, where the common scaling behaviour of this is a reduction in t_{DI} as the electric field (or bias) is increased. In a real DI system, it is impossible to get such a 'cusp like' DI transient. Due to the presence of traps and dispersive nature of the carrier motion, a typical experimental DI transient is shown in figure 1.14 b(iii) presenting a broadened transient peak. Real current transients will also display a RC displacement current resulting from the voltage pulse being applied to a sample with measurable capacitance in a circuit containing significant series resistances. Charge trapping, especially, can have a very

pronounced effect on the shape of the current transient. Trapping is characterised by a reduction of the current over time, as carriers stop contributing to the current as a result of being trapped, and strong trapping will cause the DI transit peak to disappear. Whether the t_{DI} peak can be resolved or not depends on the relative magnitudes of the trapping rate and extraction rate; as the electric field is increased the transit time is reduced, leading to increased extraction rate and the appearance of the peak above the trapping decay.

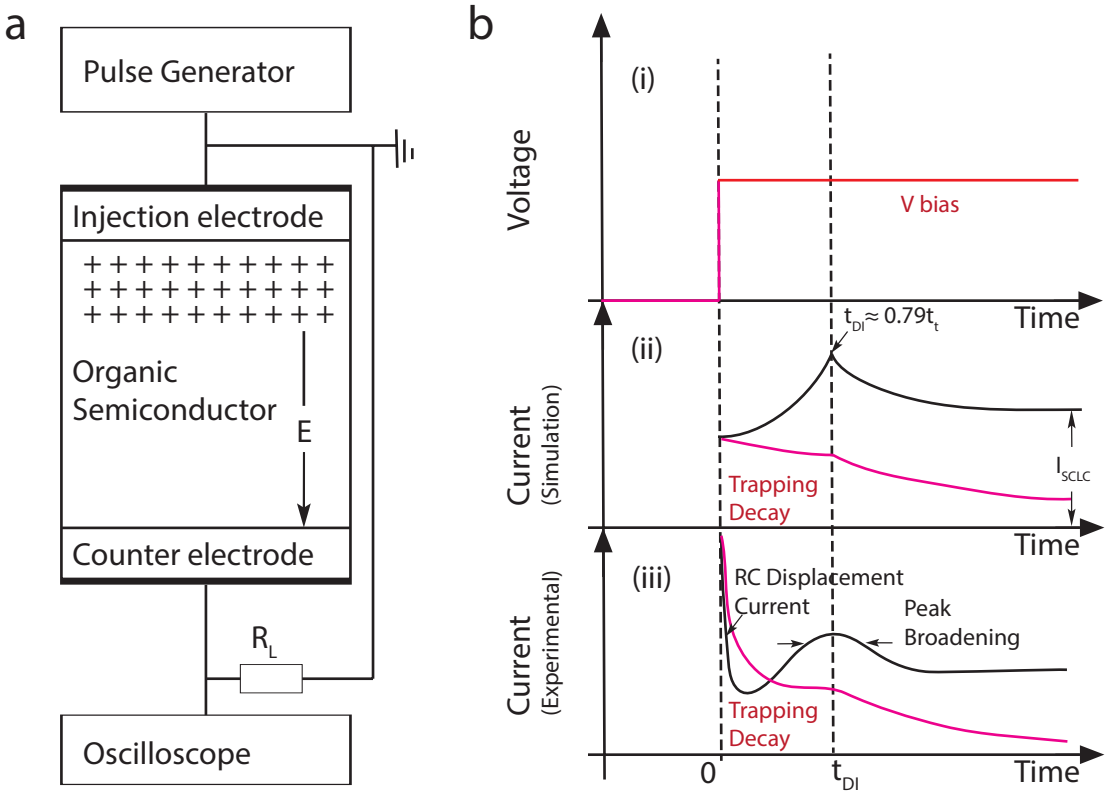

Figure 1.14: Schematic of DI experimental arrangement and schematic of the bias and the theoretical and experimental current transients

(a) Schematic of DI experimental arrangement showing The current through the NiFe-Alq$_3$ (500nm)-Al or ITO-Alq$_3$ (500nm)-Al device is measured as a function of time (providing a current-transient) as a voltage drop across a load resistor, R_L, at the oscilloscope input. ***(b)*** *Schematic of the bias and the theoretical and experimental current transients. (i) Input signal, (2) The simulated currents (adapted from [Phys. Rev.* **126**, 1980 (1962)*]) do not include the RC displacement current but do include charge trapping and the steady state current. (iii)Experimental current transients display clear displacement currents as well as distinctive peak broadening.*

1.4.3 Other methods

Except from ToF and DI, another important transient technique used in OSCs, which is called transient electroluminescence or time-resolved electroluminescence (TEL) technique. The transition time obtained by TEL is measuring delay time of luminescence after the applying of an instantaneous electric field, which is like a reversed ToF. The advantage of this method is the capability of measuring charge carriers mobility in multilayer devices. However some obvious limitations appear when using this method. It is hard to differentiate the mobility obtained by TEL is from which type of charge carriers, as electroluminescence requires injection of both electrons and holes. Even if the type of charge carrier is clearly known in the situation of multilayer OLEDs, it is also complicate to determine a charge carrier mobility, because of possible charge-carrier accumulation at the internal interfaces.

The steady state method, SCL-IV characteristics is actually using the Mott-Gurney equation Eq. 1.1, which is only valid when only one type of charge carriers dominates the injection and transport, and the mobility is assumed to be independent of the electric field. In field effect transistor method, just as its name implies, is measuring current between source and drain versus bias between gate and source in an OSC field effect transistor. And the mobility can be obtained by this measurement.

1.5 Introduction to organic spintronics

1.5.1 Spintronics

The understanding and using electricity and electronics to power machines, to store or transport information promoted human history into the technological and information revolution. However, by using their spin, we can open new exciting applications [42]. One famous application is the sensor in the reading head of every modern disk. Its development enabled the fast miniaturization and increase in storage density of hard disks in the last decades, which has benefited from the discovery of GMR effect by Fert and Grunberg, who shared the Nobel Prize in Physics in 2007 [43, 44].

Spintronic is the study of the manipulation of spin and spin-polarized transport in the solid state and has been a frontier research field for scientists [45]. The pioneering work can be traced back to 1936, when Mott explained an unusual behaviour of resistance in ferromagnetic metals (FM), by introducing the two-current model, that the conductivity of FM is the sum of two independent charge carriers, spin majority (up) current and spin minority (down) current [46, 47]. Our understanding of spin-polarized transport in spintronics devices is based on this model.

In 1973, tunnel magnetoresistance (TMR) was first discovered by Tedrow and Meservey, who used a FM/tunnel barrier/superconductor junction to experimentally determine the spin polarization of the conduction band in FM material [48]. In 1975

Julliere measured the TMR ratio for Co/Ge/Fe sandwich structure (a spin valve structure introduced in 1.2.3) and the Julliere model was developed [49]. In his model, TMR originates from the difference in the density of states (DOS) at E_F between spin up $N_{\uparrow}(E_F)$ and spin down $N_{\downarrow}(E_F)$. As shown in figure 1.15, because of the spin conserved tunnelling, electrons can be only tunnelled between spin subbands of two FM contacts with the same spin orientation. When two FM layers have antiparallel magnetization (AP) (figure 1.15 (a)), the number of tunnelling electrons with both spin orientation are small comparing with parallel magnetization configuration (P) (figure 1.15 (b)), which has a bigger tunnelling current with major spin orientation. Therefore, the resistance of the devices in P configuration (R_P) is lower than in the AP configuration (R_{AP}). The TMR ratio representing the resistance difference between P and AP configuration is derived in Eq. 1.13, where G_P (G_{AP}) is the conductance in P (AP) configuration, and $P_{1(2)}$ the polarization of the left (right) FM contact [50].

$$TMR = \frac{R_{AP}-R_P}{R_P} = \frac{G_P-G_{AP}}{G_{AP}} = \frac{2P_1P_2}{1-P_1P_2} \qquad 1.13$$

And

$$P_i = \frac{N_{i\uparrow}(E_F)-N_{i\downarrow}(E_F)}{N_{i\uparrow}(E_F)+N_{i\downarrow}(E_F)}, \quad i = 1,2. \qquad 1.14$$

Thus the polarization of the left (F1) and right (F2) electrodes shown in figure 1.15 can be expressed as the TMR. The Julliere model gives a good basic insight, however, when analysing data from TMR experiment, this formula has its limitations [27, 51]. Firstly, the polarization orientation of electrons at Fermi level should not been

interpreted from the formula above. For example, the tunnelling current observed from TMR experiment for Ni is majority electrons (the electrons with major spin orientation), but it is its minority DOS at Fermi energy. Furthermore, Julliere's TMR model represents the polarization of electrodes but ignores the property of the insulator in between. However the observation of the changing of TMR sign when only change the device's insulter indicates the importance of spacer material and interface between spacer and electrodes[52]. This model cannot explain the observed temperature and bias dependent TMR as well and a model incorporating all these effects is still lacking.

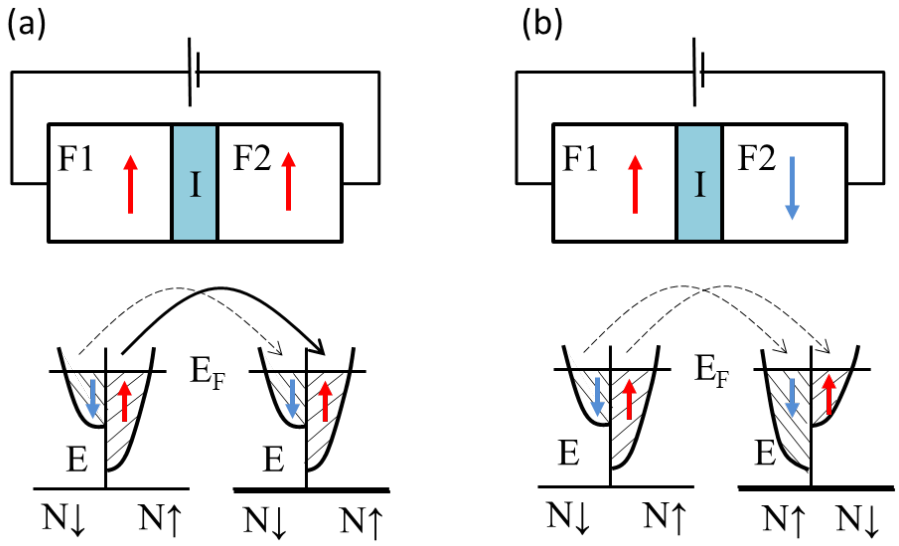

Figure 1.15: Schematic of electron tunnelling in FM/insulator/FM tunnel junctions

a) Parallel and b) antiparallel orientation of magnetizations with the corresponding spin resolved density of states (DOS) in ferromagnetic metals. The dashed (solid) arrow represents the low (high) spin current.

Although devices with TMR effect can have large MR values and can usefully act as magnetic sensors or 0-1 switchers, the non-volatile memory applications benefit from the later discovery of giant magnetoresistance (GMR) [53]. Depending on how the current flows, GMR structures are often classified to two geometries; current-in-plane (CIP) and current perpendicular to plan (CPP) and the magnetoresistance in both geometries can be explained by using two-current moles as shown in figure 1.16. The first GMR device had the CIP geometry and most of the GMR applications use this geometry, while in the case of CPP version the devices first realized by Pratt *et al*. (1991) [54] has the similar structure comparing with TMR devices as shown figure 1.15 and figure 1.16b, and is easier to analyse. Analogous to TMR, Eq. 1.13 can be used to represent the magnetoresistance in the GMR. Finally the large room temperature GMR is realized which enabled a quick transition from basic physics to commercial applications in the field of magnetic recording. [55]

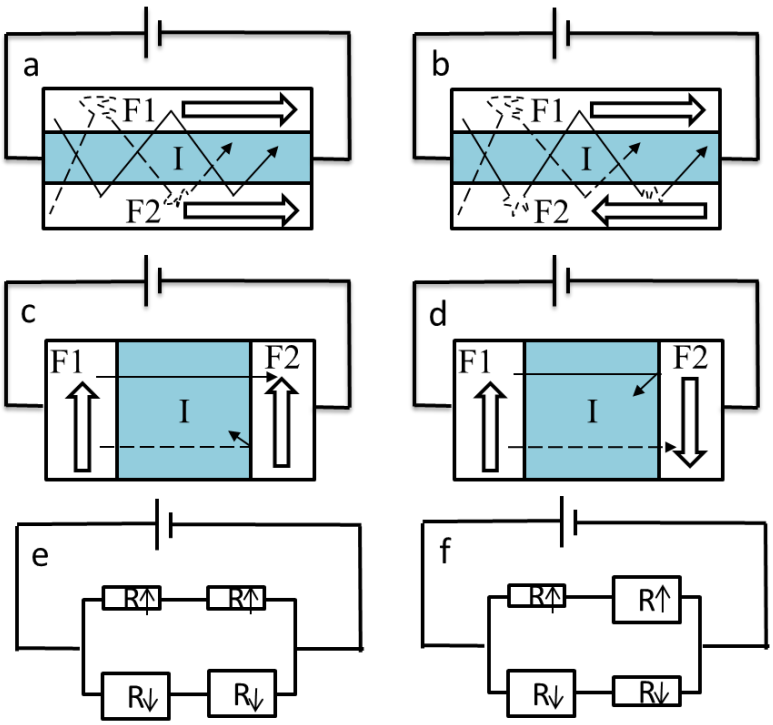

Figure 1.16: Schematic illustration of GMR geometry

a) and b) Show the current in plane (CIP) geometry. c) and d) Show the current perpendicular to the plane (CPP). Spin polarized current injection and transport in P and AP configurations are displayed in two geometries as well. The solid arrows represent the spin majority current and the dash arrows represent the spin majority current. Resistance of currents with either spin orientation in both P and AP configuration are shown in panel e) and panel f) resulting in an overall higher resistance in AP configuration than in P configuration.

In this thesis, the CPP GMR effect is mainly discussed. This effect is based on injection, transport and extraction of a spin-polarized current. A fundamental obstacle for electrical spin injection from ohmic ferromagnetic metal contacts into a semiconductor is identified as the conductance mismatch problem [56-58]. The equivalent resistance of a spin valve is the sum of the resistances of two metal

electrodes (spin dependent) and one semiconductor spacer (spin independent). So if the resistance of the spin independent semiconductor spacer dominate the resistance of the device, the spin vale will be only weakly spin dependent.

Regardless of mismatch problem, during the transport, the spin polarization is gradually lost by spin flip events. The loss is typically characterized by two quantities: the spin relaxation length l_s, and the spin relaxation time τ_s, l_s and τ_s are simply related by, $l_s = v\tau_s$ where, v is the average charge carrier velocity that can be obtained from average charge carrier mobility μ. As shown in figure 1.17, typical spin relaxation time measured in inorganic semiconductors is in the scale of nanoseconds [59, 60], while it is recently being found that in OSCs spin relaxation time is in excess of 10 microseconds [12, 29, 61]. Thus, investigations in spintronic devices based on OSCs have recently been catching increasing attention and will be discussed in next section.

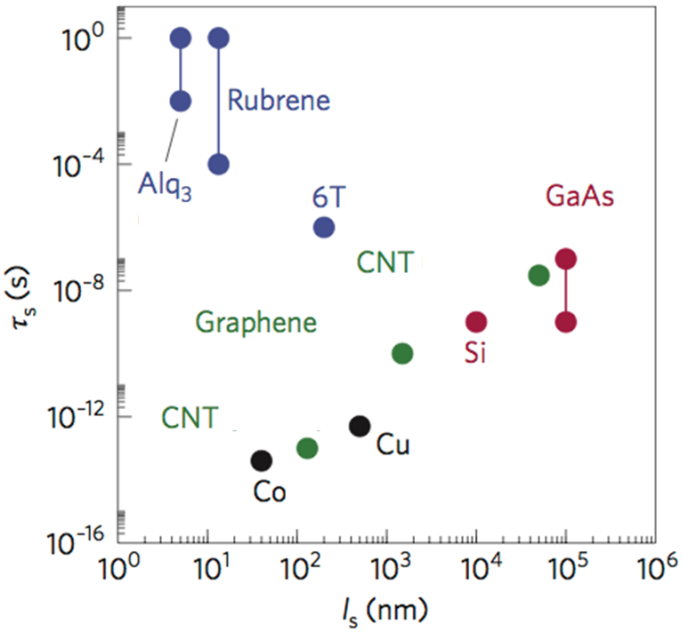

Figure 1.17: (Adapted from ref[53]) Spin-diffusion length l_S versus spin-diffusion time τ_S, for various materials

1.5.2 Organic spintronics

Long spin relaxation time along with other advantages, as introduced in section 1, cheap, easy processing, and almost infinite chemical tunability make organic materials very appealing to substitute inorganic materials used in spin valves.

The first demonstration of magnetoresistance (MR) in an 'OSV' was from a lateral device by Dediu *et al.* [62]. In this device, two ferromagnetic $La_{0.67}Sr_{0.33}MnO_3$ (LSMO) electrodes were separated by a 70-500nm sexithiophene (T_6) channel. Although the MR was explained as the result of the spin polarized carrier injection, it failed to show the direct correlation between the MR and the magnetic switching of

the electrodes' magnetization, which is what defines the spin valve operation. The first real OSV was fabricated by Xiong *el al.* in 2004, based on Alq_3 as the spacer layer sandwiched by ferromagnetic LSMO and Co electrode (1.18d) [63]. A magnetoresistance (MR) of 40% was measured at 11K that turned to zero when temperature was raised above 200K under the bias below 1V (Figure 1.18a).

Contrary to the standard spin valve introduced before, the LSMO/Alq_3/Co devices showed lower resistance at AP configuration, which is known as inverse MR. The MR was temperature dependent and bias dependent which vanished at room temperature or at bias over 1V (figure 1.18 b and e). A spin diffusion length of 45nm was estimated by fitting the MR versus Alq_3 thickness using a modified Julliere's model (Eq. 1.15) [49], which is conceptually and practically wrong. Except for the two general weakness of Julliere's model discussed before in traditional spin valves, Julliere's model is only valid for tunnelling transport so it may be inappropriate to use for a spin-injection problem in OSVs. And also Eq. 1.15 ignored spin scattering at electrodes organic interface and assume the spin polarization of the injected electrons is attenuated exponentially as e^{-d/l_s}. Furthermore, in this experiment, the author claimed an up to 100nm 'ill-defined' layer, which is due to the inclusions from top Co electrode. This is also an acute problem in OSV fabrication that limited OSV performance.

$$MR(d) = \frac{2P_1P_2e^{-d/l_s}}{1-P_1P_2e^{-d/l_s}} \qquad 1.15$$

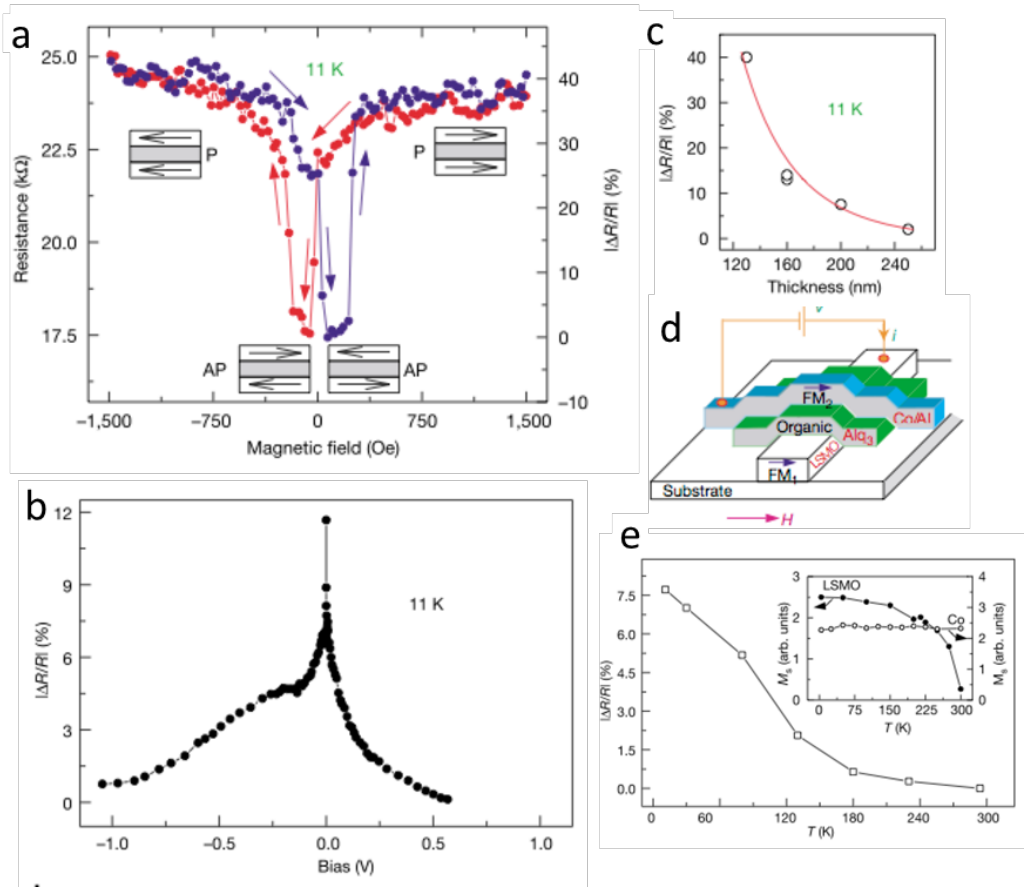

Figure 1.18: (Adapted from ref [63]) The magneto transport response of an OSV

a) Shows the GMR loop of a LSMO/Alq_3/Co spin valve. b) Shows the GMR dependence with the function of bias voltage V. c) Shows the GMR value of the device depends the thickness of the Alq_3 layer. d) Shows the structure of the LSMO/Alq_3/Co spin valve. e) Shows the temperature dependence of GMR. The inset shows the magnetizations of the Co and LSMO electrodes versus T, measured using MOKE.

Since then, combined with the development of chemical syntheses and optimization of device fabrication, electrical detection of MR has been obtained in a vast number of OSV devices with OSC interlayers based on either small molecules (e.g. pentacene,

rubrene, N,N'-bis-(1-naphtalenyl)-N,N'-bis(phenyl) benzidiane (α-NPD), 4,4'-bis99-(ethyl-3-carbazovinylene)-1,1'-biphenyl (CVB), copper(II) phthalocyanine (CuPc), C_{60}) or π-conjugated polymers (e.g. poly(3-hexylthiophene-2,5-diyl) regioregular (RR-P3HT), poly-(dioctyloxy) phenyl vinylene (DOO-PPV),).[25, 62, 64-78] The properties of OSVs have been improved by using these new materials. However, a number of fundamental issues without a definite solution were left by the early experiments.

The most acute problem for OSV is the poor reproducibility in the early experiments. The main cause of this problem was the diffusion of atoms belonging to the top metal electrode to the soft organic spacer, as the 'hot' metal atoms are usually involved, during the fabrication process. The existence of metal inclusion was not only impairing spin injection but also shorting the device. Recently, the MR value of inorganic spin valves has been greatly increased by improving FM/spacer interfaces.[55, 79] A similar approach has been tried for OSVs. Dediu *et al.* inserted an inorganic insulating layer (Al_2O_3) between the top Co electrode and Alq_3 to prevent the inter-diffusion.[80] However with inserting of this Al_2O_3 layer the improved device reproducibility and stability is at the expense of losing some spin polarization injection, thus this device only performed ~10% MR at low temperature. As the insulating layer does not appear to improve much of the MR value, Sun *et al.* introduced a layer of magnetic nanodots between top Co electrode and Alq_3 spacer (1.19). Because magnetic nanodots have a greater size and lower evaperation

temperature, they are expected to have a much lower diffusion rate into organic spacer. This so called buffer layer assisted growth (BLAG) method significantly improved the MR value of OSV to ~300% (figure 1.19) [81].

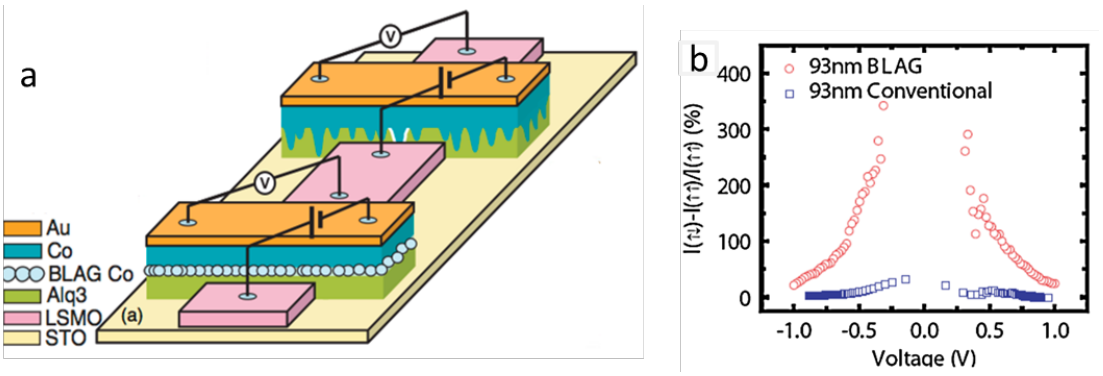

Figure 1.19: (adapted from ref[81]) (a) Schematic diagrams of a BLAG OSV and a conventional OSV. (b) MR obtained as a function of bias voltage for the BLAG OSV and the conventional OSV

Apart from incorporating the protection layer, other approaches including changing top FM electrode, and improving device fabrication process have been used. Yoo *et al.* managed to fabricate an all OSV by using an organic FM layer as the top electrode [82]. This organic FM layer was chemically deposited at a very low temperature (40K) that significantly suppressed the inter-diffusion of top organic FM layer into organic spacer. However the obtained ~2% MR effect indicated a very low spin polarization degree of the deposited organic FM electrode. Wang *et al.* used the indirect deposition method to grow top FM electrode.[83] In this method, before Co evaporation the chamber was purged with Ar gas, the Co atoms were evaporated by electron beam source. After scattering with Ar atoms several times, the Co atoms or clusters reached

the organic spacer surface with reduced kinetic energy. In this way Co penetration into the organic layer has been supressed. By using this method a low (~0.06%) MR effect was obtained for the LSMO/Alq_3/Co device at the room temperature.

The other fundamental problem is the understanding of spin injection and transport mechanism in the OSC. One critical issue that is under debate is whether the observed MR is due to purely spin tunneling between FM electrodes or the spin current injection and transport in the bulk of OCSs [67-69]. The investigation of the temperature dependence of the MR by Wang *et al.* found that MR of spin valve devices decreased with temperature following exactly the surface magnetization of LSMO and independent of OSC spacer [66]. This phenomenon agreed with Dediu's results in 2008, and it seems that the MR have nothing to do with OSC spacer but is due to electrode polarization (1.20 a and b)[80]. Nevertheless, in the review paper published in 2009, Dediu *et al.* presented a different temperature dependence for the LSMO/Alq_3/Co structure OSV with 130nm 160nm and 100nm Alq_3, which indicate that spin bulk transportation can also contribute to the value of MR (figure 1.20 c) [53].

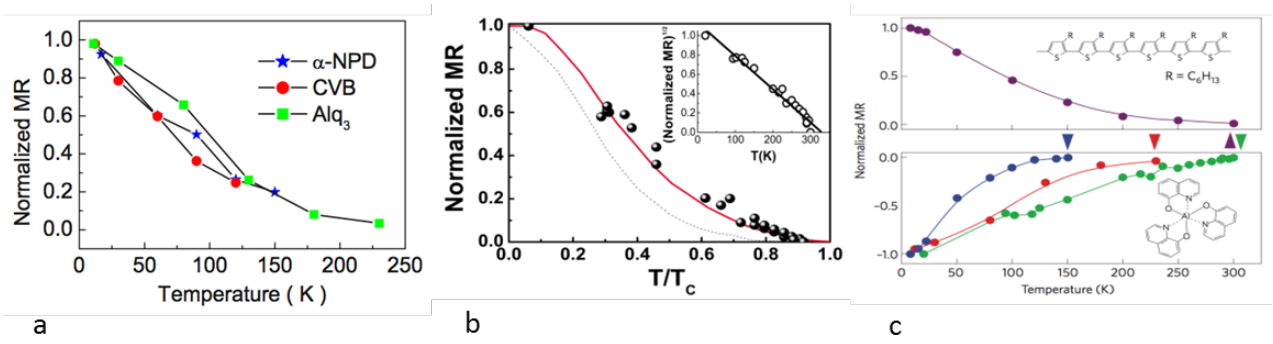

Figure 1.20: (adapted from ref[53] [66] [80]) Temperature dependent MR.

(a) The MR value of three different LSMO/OSC/Co spin-valve devices versus temperature T normalized at T=14 K. (b) Comparison between MR, (dots), the LSMO surface magnetization (solid line), and the polarized charge-carrier density (dotted). Both magnitudes are plotted in reduced temperature scale normalized to Tc. The inset shows the linearized data. (c) MR of LSMO/OSC/Co OSVs the blue, red and green data represents Alq_3 with 130, 160 and 100nm thickness respectively.

It was not until recently that people observed the existence of Hanle effect in the OSVs, in which the MR in spin valves changes upon the application of additional perpendicular magnetic field [84, 85]. The Hanle effect is a clear experiment that proves the existence of spin injection and transport in the bulk of OSVs, which indicates the importance of spin diffusion in the bulk of OSCs. Furthermore, there is another evidence that also shows the spin polarized current is present over a large area within the OSC devices, the low-energy muon spin rotation (LE-μSR) [86, 87]. As shown in figure 1.21, the LE-μSR data obtained from high T_c electrode NiFe/Alq_3/FeCo spin valves show that the temperature dependence of the spin diffusion length corresponds exactly to that of the MR, and as the magnetism of NiFe

or FeCo is barely changed in this temperature range, this result suggests that the spin diffusion in the OSC spacer is equally important for the spin valve effect.

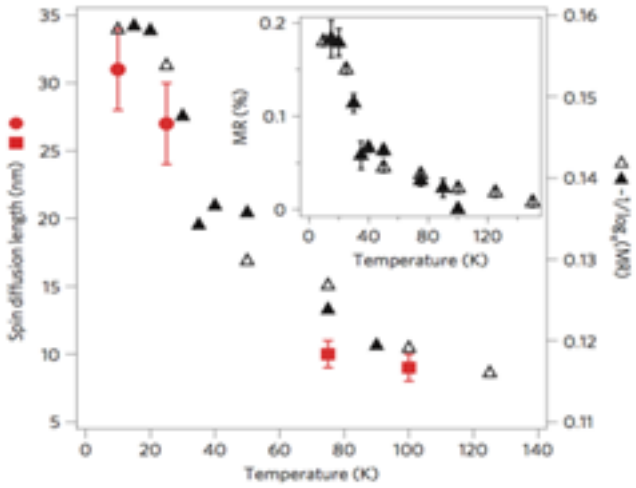

Figure 1.21: (adapted from ref[86]) Correlation between spin diffusion length and magnetoresistance for the NiFe/Alq_3/FeCo devices in the LE-μSR experiment .

As shown in figure 1.22 e and f, recent experiments for OSVs either with decreased spin injection barrier in the FM/OSC interface[88, 89], or reduced hyperfine interaction, one of the mechanisms of the spin relaxation, in the bulk of OSC showing no difference of temperature dependence of MR, which make this argument even more complex[90]. One possible explanation is that both interfacial spin injection and bulk spin transport can contribute to spin valve effect, while which one dominates depends on the choice of FM and OSC material, and the interface qualities between FM and OSC layers.

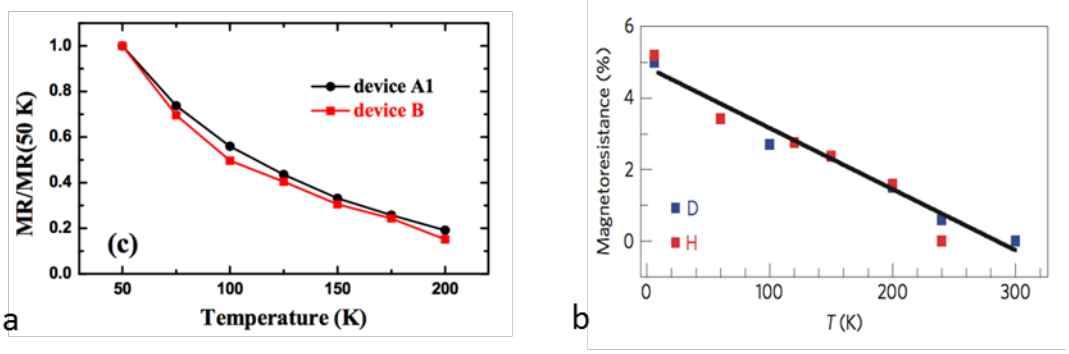

Figure 1.22: (adapted from ref[88] [89]) Temperature dependent MR.

(a)Temperature dependent MR with two OSVs (device A1 and B have different injection barrier in the FM/OSC interface). (b) Temperature dependent MR with H- and deuterated, D-hydrogen polymer OSVs.

1.5.3 Introduction to hybridized interface sates (HINTS)

Apart from the issues discussed before, one of the puzzling experimental results obtained from the OSVs was the sign of the MR. In the LSMO-Alq_3-Co device for example, the inverse spin valve effect has been regularly observed since the first experiment [63, 66, 67, 91]. The Julliere model has been commonly used to analyse this phenomenon. If spin majority (up) charge carriers are injected from LSMO, the spin minority (down) charge carriers are preferred to be extracted from the Alq_3/Co interface. This naturally leads to the conclusion that LSMO and Co have opposite spin polarization of electrons at the Fermi energy level. However this explanation contradicts the fact that Co and LSMO are both widely accepted as majority (spin up) injectors [92]. Later on, a positive MR on the same structure OSVs were obtained by Barraud *et al.* that confirmed this suspicion, and a concept of hybridized interface states were introduced to explain this phenomenon.

Barraud *et al.* fabricated an Alq_3 based nanometre-scale OSV tunnelling device. As shown in figure 1.23, the nanoindent in the Alq_3 layer was realized by conductive-Atomic Force Microscopy (AFM) that allowed them to control the organic tunnel barrier thickness. Subsequently the nano-hole was filled with Co leading to an LSMO/Alq_3/Co nano-size magnetic tunnel junction, which exhibit a MR up to 300%. The authors explained this high obtained MR value by a spin hybridization transport model, which demonstrated the effective polarized spin injection or even the observed sign reversal of injected spins is due to the formation of HINTS in the first molecular layer at electrode interface.

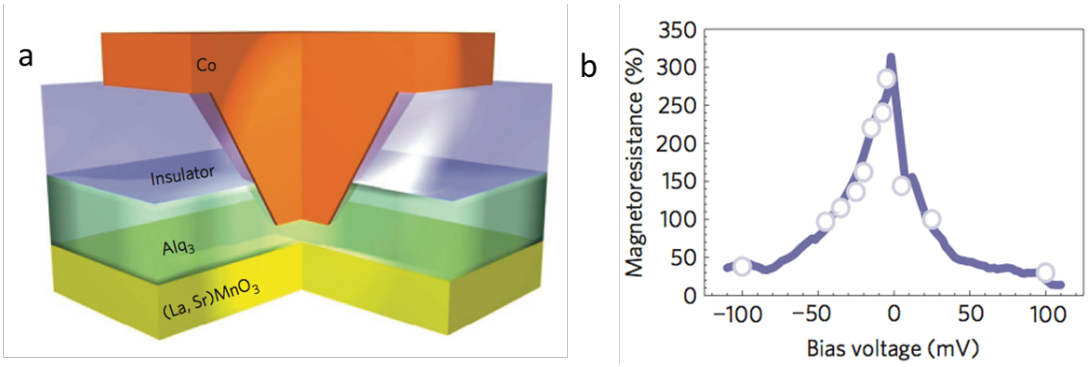

Figure 1.23: (adapted for ref. [93]) (a) Schematic of the organic MTJ OSV. (b) MR obtained as a function of bias voltage for the MTJ OSV.

This model has been explained by Sanvito [76, 93]. Figure 1.24a shows the superposition of the individual DOS of two spin orientations for the spin subbands of ferromagnetic electrode and the HOMO of the organic molecule. When the two materials are brought to contact, the DOS gets modified into two ways, the energy

levels broaden (figure 1.24b) and their position shifts in energy (figure 1.24c) Due to the hybridization of FM/OSC interface and the presence of HIINTS. The spin-up and spin-down energy levels of the molecule are broadened by different amounts, because of the offset of the two spin subbands in ferromagnetic electrode. As a result, if the broadened molecular orbital at the EF presents opposite spin-polarization than that of the electrode (figure 1.24b), it will present a negative MR; otherwise if the broadened molecular orbital at the EF presents the same spin-polarization due to the energy level shift, it will present a positive MR (figure 1.24c).

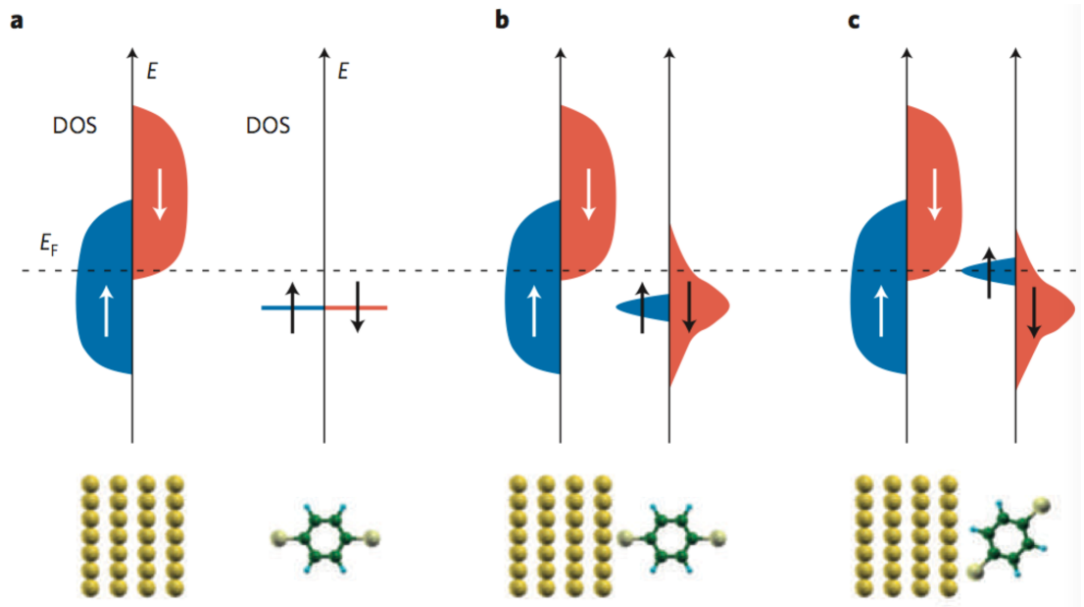

Figure 1.24: (adapted from ref [76])Schematic of the spin-filtering mechanism at an organic/inorganic hybrid interface

The HINTS discussed in this hypothesis has later been observed by spin resolved near-threshold photoemission spectroscopy (NT-SP) and spin-resolved 2PPE measurements by Steil *et al.* and Droghetti *et al* [93, 94]. They also investigated the origin of HINTS by theoretical density functional theory (DFT) calculation. The

lowest energy geometry for Alq_3 on Co is shown in figure 1.25. Two quinoline ligands of Alq_3 laid down on the Co surface result in strongly chemisorbed bond through the hybridization between the d-Co state and the p_z orbitals of the ligands. The computed result of DOS is displayed in figure 1.26, which agreed well with the experiment result.

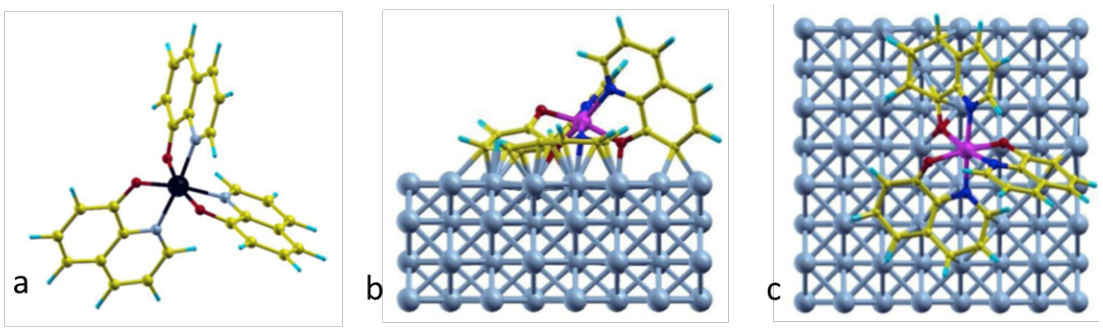

Figure 1.25: adapted from ref. [94]) (a) Structure of the Alq3 molecule. (b) Top view and (c) lateral view of the Alq3/Co interface after the DFT geometry optimization

Colour code: C (yellow), O (red), N (gray), H (blue), and Al (purple).

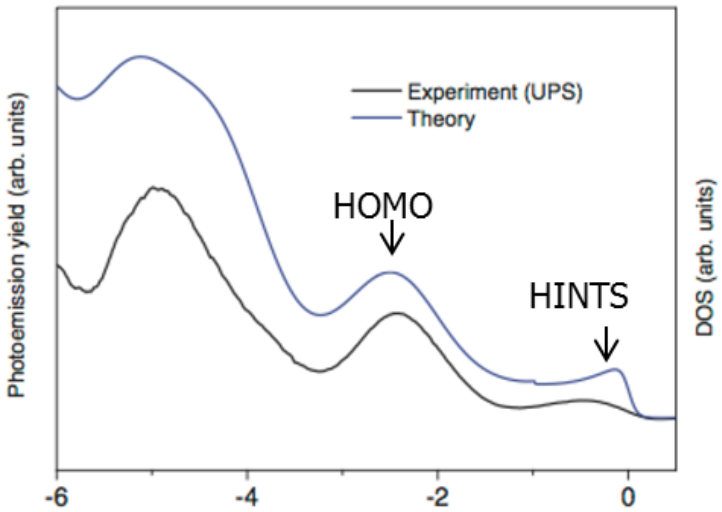

Figure 1.26: (adapted from ref. [94])UPS spectrum and total DOS for one monolayer of Alq_3

1.5.4 Introduction to spin-OLED

As introduced in section 1.2.2, the light-emitting nature of OLED was due to the exciton recombination. The excitons can exists in four states, which are grouped into two categories, singlets and triplets (singlet state excitons and triplet state excitons). As shown in figure 1.27, in conventional OLEDs, due to the random orientation of spin injection, the ratio between singlets and triplets is 1:3. Owing to the fact that the radioactive recombination time (life time) of triplets is much longer than that of singlets, only singlets contribute to light emission, therefore the maximum internal quantum efficiency cannot exceed 25%.

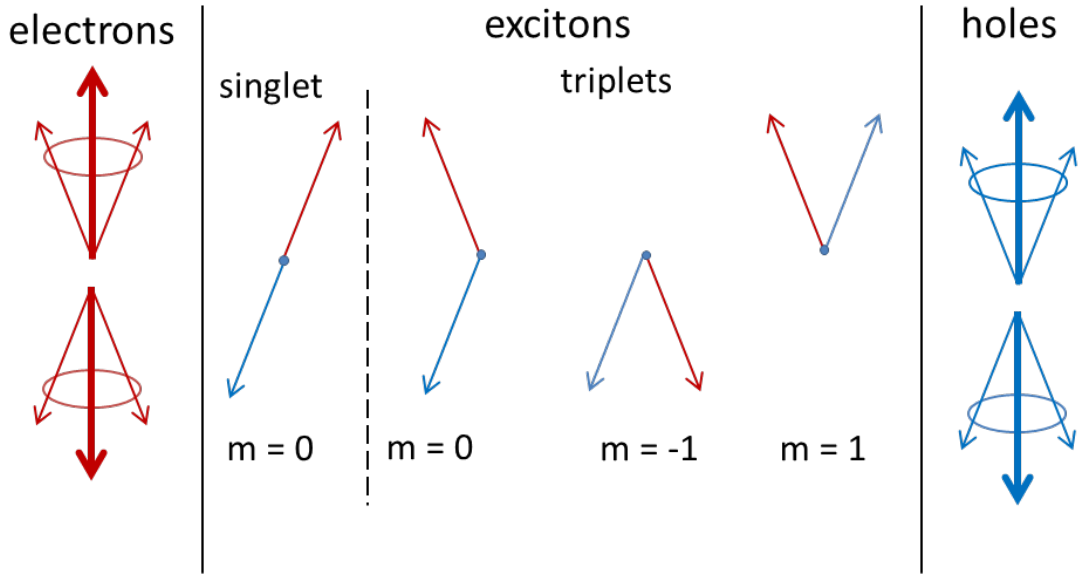

Figure 1.27: Spin statistics of exitons formed in a conventional OLED by injected electrons and holes with random spin orientation.

The singlet has a zero spin angular momentum (S=0), but triplets have non-zero spin angular momentum (S=1), in which both the electron and hole have spin up or spin down orientation or the electron and hole have opposite spin orientation but with a non-zero resultant spin and a zero Z component (m=0)

The idea of spin polarized OLED or spin-OLED is to the combine OSVs and OLEDs, by replacing the electrodes of OLED with FM electrodes. In this case, by injecting spin polarized charge carriers from FM, the ratio of singlets, and hence the light emission can be manipulated. As illustrated in figure 1.28, ideally, if two electrodes are spin polarized and aligned anti-parallel, all the excitons formed will be triplets, while if the injected electrons and hole are in parallel spin orientation, half of the excitons will have singlet state, thus the light output will be significantly improved.

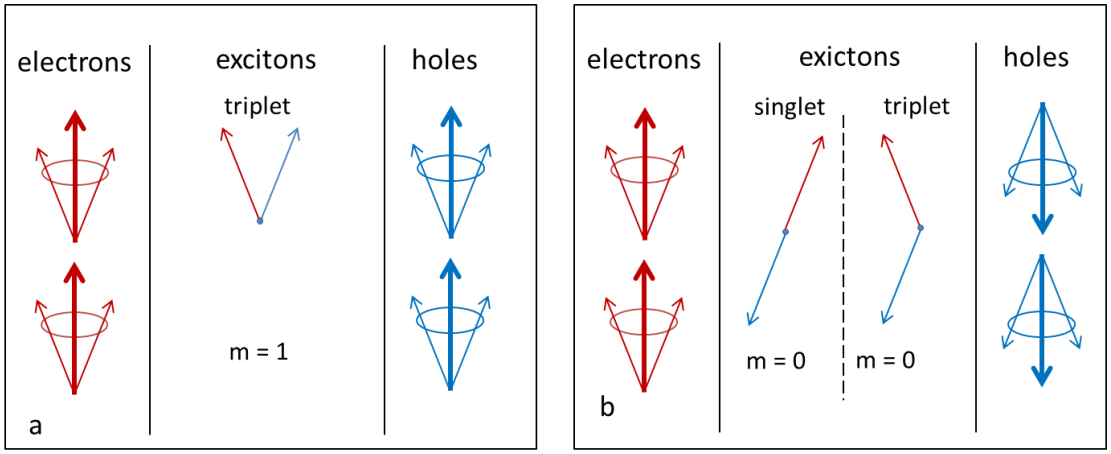

Figure 1.28: Spin statistics of exitons formed in a spin-OLED with spin polarized injection in (a) parallel alignment, and (b) antiparallel alinment.

This idea has not been successfully achieved in early experiments, when people used Alq_3, which is popular in both OSVs and OLEDs, as the OSC interlayer between FM electrodes [95-97]. The main difficulty was that the MR response of OSV devices was usually limited to significant low voltage (< 1V), whereas for OLEDs the efficient light emission requires much higher bias voltage (> 3V)[98].

With the development of chemical syntheses and optimization of device fabrication, in 2012, Nguyen *et al.* reported in Science the realization of a spin-OLED with magneto-electroluminescence (MEL) on the order of ~1% at 3.5V at low temperature [99]. To improve the electron injection, they deposited a thin LiF buffer layer in front of the FM cathode. To reduce the hyperfine interaction and increase the spin transport in the bulk of OSC, they used a deuterated polymer interlayer. In this experiment, the MEL value is perhaps not substantial, but the ability of injecting simultaneously both electrons and holes with polarized spin orientation is new in the field of spintronics. Recently, an Alq_3 based spin-OLED with a single FM electrode was fabricated by Ding *et al [100]*. They improved hole injection and room temperature spin injection, by combining the deposition of a thin p-type organic buffer layer and the use of oxygen plasma treatment on the surface of FM cathode. An observation of light output changing when applied an in-plane magnetic field proved the injection of spin polarized charge carriers.

1.6 Motivation

In the previous discussion one can see, over the past decade the researches in the field of organic spintronics were mainly based on the former experience of the inorganic spintronics. However fundamental differences between organic and inorganic semiconductor limited the progress of organic research and the improvement of OSV performance. On the contrary, in the field of organic light emitting devices (OLED),

with tens of years of study and commercialization, the performance of OLEDs has witnessed a remarkable increase. Therefore to get a deep understanding of organic spintronic devices OSVs we have to refer to OLEDs.

OLED and OSVs share many similarities in that they both have the electrode-OSC(s)-electrode sandwich device structure and the carrier injection, transport and extraction are similar[4, 63, 101]. In the case of OSVs the electrodes are ferromagnetic which can result in the injection of spin polarized charges into the organic layer and subsequent spin selective extraction at the other electrode. OSVs and OLEDs both depend on the injection of holes from the anode into HOMO and/or the injection of electrons from the cathode into the LUMO of the OSCs.

Since OSVs rely on the spin polarised injection and extraction of at least one type of carrier (holes or electrons) for their operation, the injection of charges from FM electrodes is of paramount importance in studying their operation [27]. Much of the initial work on OSVs was based on the use of Alq_3 as the organic charge transport layer, and since Alq_3 is widely used as an electron transport material in OLEDs, it has been assumed that electrons are the dominant charge carrier in OSVs [102]. For example, in order to explain the negative MR in OSVs Dediu *et al.* built a model, which was based on injection and extraction of electrons with minority spin orientation [80]; In a later Nature Material review paper they labelled Alq_3 as a ‘n type’ OSC where electrons were preferred to be injected and transport [53]; To

explain the temperature dependent IV data in a Fe-Alq_3-Co OSV, Liu *et al.* claimed that electrons were injected from Fe into Alq_3 at positive bias and from Co into Alq_3 at negative bias [103]. Zhang *et al.* also reported that the Alq_3 is one of the most promising candidates using as the middle spacer for spin transport because of its efficiency electron transport mobility [104]. There are also the evidence of UPS and density function theory (DFT) calculations that support the electron injection [105-107].

Clearly, what particular charge carrier is injected depends on both the electrode material as well as the OSC [108]. In particular, the alignment between the Fermi level of the electrode material and the HOMO and LUMO of the organic layer is important. For OSVs, the magnetic contacts are normally based on LSMO or transition metal electrodes or their alloys, such as Fe or NiFe [87, 109]. Regardless of the vacuum level shifts, magnetic electrodes used in OSVs, in particular the transition metals and LSMO generally have high work functions (4.8~5.2eV) [110, 111]. Therefore their Fermi level are closer to the HOMO rather than the LUMO of OSCs, so the FM/OSC interface would be expected to have lower hole injection barriers than electron injection barriers. This was supported by internal photoemission measurements of Schottky barriers [112], X-ray and UPS measurements in the interface between FM and OSC layers [113]. A further in-depth electroluminescence study on the OLEDs with various cathodes also supported the idea that holes dominate FM/OSC charge carrier injection [114]. As shown in figure 1.29, the Alq_3

OLEDs with high work function cathodes, Al, Ag, Zn or Cu (with work functions of 4.3 4.32, 4.47 and 4.7eV respectively) demonstrated significantly reduced light output compared with the device with low work function cathodes. This is because electrons were not efficiently injected from the high work function cathodes, due to high electron injection barriers in the OSC/electrode interfaces. In this case, for OSVs the FM electrodes, which have even higher work functions, should act as poorer electron injectors but better hole injectors.

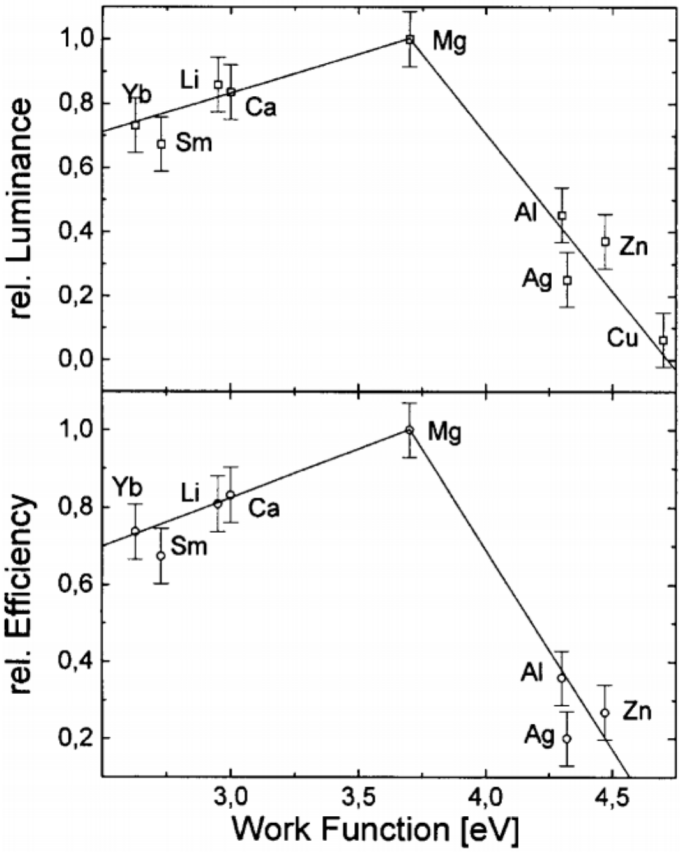

Figure 1.29: (adapted from ref [114]) Relative luminance and efficiency for OLEDs as a function of cathode work function. All data are normalized to the corresponding data for Mg cathode OLED.

There is another issue that typical operating conditions, are very different between OLEDs and OSVs; whereas OSVs can operate at small bias (V_{bias} ~ 100mV) [53, 63, 87, 99], OLEDs require a much larger voltage for light emission (V_{bias} ~ 3V) [4, 87]. This is the case even though the organic layer Alq_3 thickness is similar (~100nm) in both types of device and demonstrates some fundamental differences between the two device types. As shown in figure 1.30, for OLEDs the high operating voltage is characteristic of the built in potential (V_{bi}) in the device which is due, in part, to the difference in the Fermi levels of the two contact materials required to give both efficient hole injection from the anode and electron injection from the cathode. And the low drive voltage for OSVs is partly due to small work function difference between two FM electrodes, while there is still the existence of charge carrier injection barriers (Φ_e or Φ_h) in the electrode/OSC interfaces, which is of the order of ~1eV for Alq_3 based OSVs. The extremely low drive voltage (~100mV) for OSVs implies that the actual charge carrier injection barrier is smaller than the theoretical expectation, and this issue has not been well explained [95, 99, 115].

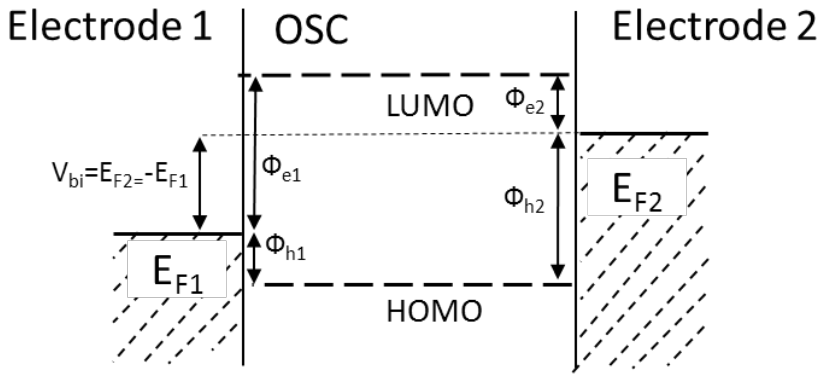

Figure 1.30: Electronic structure of an OSC device Vbi is the builid-in potential, Φ e and Φ h is electron injection barrier and hole injection barrier in the electrode/OSC interface.

In this thesis, the OLEDs with FM cathodes are investigated, and the type of injected carriers in the Alq_3 based OSVs is identified by comparing the mobility of injected carriers with initial motilities of both electrons and holes in Alq_3. The initial mobility of photo generated electrons and holes in Alq_3 are measured by time of flight (ToF) technique. The mobility of injected carries is systematically measured by dark injection (DI) technique. In addition, the interfacial diploes or trap states which is the so called HINTS between FM/OSCs, introduced by FM are investigated by the DI technique, and a model to explain the low operational voltage of OSVs is proposed.

References

[1] Y. Shirota, H. Kageyama, Charge carrier transporting molecular materials and their applications in devices, Chem. Rev. , 107 (2007) 953-1010.

[2] W. Naber, S. Faez, W. Van der Wiel, Organic spintronics, J. Phys. D: Appl. Phys. , 40 (2007) R205.

[3] T.R. Hebner, J.C. Sturm, Local tuning of organic light-emitting diode color by dye droplet application, Appl. Phys. Lett. , 73 (1998) 1775-1777.

[4] C.W. Tang, S.A. VanSlyke, Organic electroluminescent diodes, Appl. Phys. Lett. , 51 (1987) 913-915.

[5] J.H. Burroughes, D.D.C. Bradley, A.R. Brown, R.N. Marks, K. Mackay, R.H. Friend, P.L. Burns, A.B. Holmes, Light-emitting diodes based on conjugated polymers, Nature, 347 (1990) 539-541.

[6] J.S. Kim, M. Granström, R.H. Friend, N. Johansson, W.R. Salaneck, R. Daik, W.J. Feast, F. Cacialli, Indium–tin oxide treatments for single- and double-layer polymeric light-emitting diodes: The relation between the anode physical, chemical, and morphological properties and the device performance, J. Appl. Phys. , 84 (1998) 6859-6870.

[7] K. Sugiyama, H. Ishii, Y. Ouchi, K. Seki, Dependence of indium–tin–oxide work function on surface cleaning method as studied by ultraviolet and x-ray photoemission spectroscopies, J. Appl. Phys. , 87 (2000) 295-298.

[8] D.J. Milliron, I.G. Hill, C. Shen, A. Kahn, J. Schwartz, Surface oxidation activates indium tin oxide for hole injection, J. Appl. Phys. , 87 (2000) 572-576.

[9] Y.S. Park, E. Kim, B. Hong, J. Lee, Characteristics of ITO films with oxygen plasma treatment for thin film solar cell applications, Mater. Res. Bull. , 48 (2013) 5115-5120.

[10] T.M. Brown, R.H. Friend, I.S. Millard, D.J. Lacey, J.H. Burroughes, F. Cacialli, Efficient electron injection in blue-emitting polymer light-emitting diodes with LiF/Ca/Al cathodes, Appl. Phys. Lett. , 79 (2001) 174-176.

[11] T.M. Brown, I.S. Millard, D.J. Lacey, J.H. Burroughes, R.H. Friend, F. Cacialli, The influence of LiF thickness on the built-in potential of blue polymer light-emitting diodes with LiF/Al cathodes, Synth. Met. , 124 (2001) 15-17.

[12] R.H. Friend, R.W. Gymer, A.B. Holmes, J.H. Burroughes, R.N. Marks, C. Taliani, D.D.C. Bradley, D.A.D. Santos, J.L. Bredas, M. Logdlund, W.R. Salaneck, Electroluminescence in conjugated polymers, Nature, 397 (1999) 121-128.

[13] M. Pope, C.E. Swenberg, Electronic processes in organic crystals and polymers, Oxford University Press1999.

[14] H. Ishii, K. Sugiyama, E. Ito, K. Seki, Energy level alignment and interfacial electronic structures at organic/metal and organic/organic interfaces, Adv. Mater. , 11 (1999) 605-625.

[15] E.H. Rhoderick, R.H. Williams, Metal Semiconductor Contacts, Oxford University Press, Incorporated1988.

[16] B.J. de Gans, P.C. Duineveld, U.S. Schubert, Inkjet Printing of Polymers: State of the Art and Future Developments, Adv. Mater. , 16 (2004) 203-213.

[17] D.P. Woodruff, T.A. Delchar, Modern Techniques of Surface Science, Cambridge University Press1994.

[18] C. Kittel, Introduction to Solid State Physics, Wiley2004.

[19] S. Meloni, A. Palma, J. Schwartz, A. Kahn, R. Car, Chemistry between Magnesium and Multiple Molecules in Tris(8-hydroxyquinoline) Aluminum Films, J. Am. Chem. Soc. , 125 (2003) 7808-7809.

[20] C. Shen, I.G. Hill, A. Kahn, J. Schwartz, Organometallic Chemistry at the Magnesium− Tris(8-hydroxyquinolino)aluminum Interface, J. Am. Chem. Soc. , 122 (2000) 5391-5392.

[21] C. Shen, A. Kahn, J. Schwartz, Chemical and electrical properties of interfaces between magnesium and aluminum and tris-(8-hydroxy quinoline) aluminum, J. Appl. Phys. , 89 (2001) 449-459.

[22] C. Shen, A. Kahn, The role of interface states in controlling the electronic structure of Alq3/reactive metal contacts, Org. Electron. , 2 (2001) 89-95.

[23] J.H. Wei, S.J. Xie, L.M. Mei, J. Berakdar, Y. Yan, Conductance switching,

hysteresis, and magnetoresistance in organic semiconductors, Org. Electron. , 8 (2007) 487-497.

[24] M. Cinchetti, S. Neuschwander, A. Fischer, A. Ruffing, S. Mathias, J.-P. Wüstenberg, M. Aeschlimann, Tailoring the Spin Functionality of a Hybrid Metal-Organic Interface by Means of Alkali-Metal Doping, Phys. Rev. Lett. , 104 (2010) 217602.

[25] M. Cinchetti, K. Heimer, J.-P. Wustenberg, O. Andreyev, M. Bauer, S. Lach, C. Ziegler, Y. Gao, M. Aeschlimann, Determination of spin injection and transport in a ferromagnet/organic semiconductor heterojunction by two-photon photoemission, Nat. Mater. , 8 (2009) 115-119.

[26] J. Anderson, E. McDonald, P. Lee, M. Anderson, E. Ritchie, H. Hall, T. Hopkins, E. Mash, J. Wang, A. Padias, Electrochemistry and electrogenerated chemiluminescence processes of the components of aluminum quinolate/triarylamine, and related organic light-emitting diodes, J. Am. Chem. Soc. , 120 (1998) 9646-9655.

[27] A.J. Drew, G. Szulczewski, L. Nuccio, W.P. Gillin, The role of interfaces in organic spin valves revealed through spectroscopic and transport measurements, physica status solidi (b), 249 (2012) 9-17.

[28] P.W.M. Blom, M.J.M. de Jong, J.J.M. Vleggaar, Electron and hole transport in poly(p‐phenylene vinylene) devices, Appl. Phys. Lett. , 68 (1996) 3308-3310.

[29] G. Szulczewski, S. Sanvito, M. Coey, A spin of their own, Nat. Mater. , 8 (2009) 693-695.

[30] J. Frenkel, On Pre-Breakdown Phenomena in Insulators and Electronic Semi-Conductors, Phys. Rev., 54 (1938) 647-648.

[31] H. Bässler, Charge transport in disordered organic photoconductors a Monte Carlo simulation study, physica status solidi (b), 175 (1993) 15-56.

[32] Y.N. Gartstein, E.M. Conwell, High-field hopping mobility in molecular systems with spatially correlated energetic disorder, Chem. Phys. Lett. , 245 (1995) 351-358.

[33] D.H. Dunlap, P.E. Parris, V.M. Kenkre, Charge-Dipole Model for the Universal Field Dependence of Mobilities in Molecularly Doped Polymers, Phys. Rev. Lett. , 77 (1996) 542-545.

[34] Z.G. Yu, D.L. Smith, A. Saxena, R.L. Martin, A.R. Bishop, Molecular Geometry Fluctuation Model for the Mobility of Conjugated Polymers, Phys. Rev. Lett. , 84 (2000) 721-724.

[35] Z.G. Yu, D.L. Smith, A. Saxena, R.L. Martin, A.R. Bishop, Molecular geometry fluctuations and field-dependent mobility in conjugated polymers, Phys. Rev. B, 63 (2001) 085202.

[36] M. Ikai, S. Tokito, Y. Sakamoto, T. Suzuki, Y. Taga, Highly efficient phosphorescence from organic light-emitting devices with an exciton-block layer, Appl. Phys. Lett. , 79 (2001) 156-158.

[37] R.G. Kepler, Charge carrier production and mobility in anthracene crystals, Phys. Rev., 119 (1960) 1226.

[38] O.H. LeBlanc, Hole and Electron Drift Mobilities in Anthracene, The Journal of Chemical Physics, 33 (1960) 626-626.

[39] H. Scher, E.W. Montroll, Anomalous transit-time dispersion in amorphous solids, Phys. Rev. B, 12 (1975) 2455-2477.

[40] D. Poplavskyy, T. Kreouzis, A. Campbell, J. Nelson, D. Bradley, Injection and charge transport in polyfluorene polymers, Mater. Res. Soc. Symp. Proc. , Cambridge Univ Press2002, pp. 67-78.

[41] A. Many, G. Rakavy, Theory of transient space-charge-limited currents in solids in the presence of trapping, Phys. Rev., 126 (1962) 1980.

[42] C. Chappert, A. Fert, F.N. Van Dau, The emergence of spin electronics in data storage, Nat. Mater. , 6 (2007) 813-823.

[43] M.N. Baibich, J.M. Broto, A. Fert, F.N. Van Dau, F. Petroff, P. Etienne, G. Creuzet, A. Friederich, J. Chazelas, Giant Magnetoresistance of (001)Fe/(001)Cr Magnetic Superlattices, Phys. Rev. Lett. , 61 (1988) 2472-2475.

[44] G. Binasch, P. Grünberg, F. Saurenbach, W. Zinn, Enhanced magnetoresistance in layered magnetic structures with antiferromagnetic interlayer exchange, Phys. Rev. B, 39 (1989) 4828-4830.

[45] S.A. Wolf, D.D. Awschalom, R.A. Buhrman, J.M. Daughton, S. von Molnár, M.L. Roukes, A.Y. Chtchelkanova, D.M. Treger, Spintronics: A Spin-Based

Electronics Vision for the Future, Science, 294 (2001) 1488-1495.

[46] N. Mott, The electrical conductivity of transition metals, Proceedings of the Royal Society of London. Series A, Mathematical and Physical Sciences, 153 (1936) 699-717.

[47] N. Mott, The resistance and thermoelectric properties of the transition metals, Proceedings of the Royal Society of London. Series A-Mathematical and Physical Sciences, 156 (1936) 368-382.

[48] P.M. Tedrow, R. Meservey, Spin Polarization of Electrons Tunneling from Films of Fe, Co, Ni, and Gd, Physical Review B, 7 (1973) 318.

[49] M. Julliere, TUNNELING BETWEEN FERROMAGNETIC-FILMS, Phys. Lett. A 54 (1975) 225-226.

[50] G.A. Prinz, Device physics - Magnetoelectronics, Science, 282 (1998) 1660-1663.

[51] J.S. Moodera, L.R. Kinder, T.M. Wong, R. Meservey, Large Magnetoresistance at Room Temperature in Ferromagnetic Thin Film Tunnel Junctions, Phys. Rev. Lett. , 74 (1995) 3273-3276.

[52] J.M. MacLaren, X.G. Zhang, W.H. Butler, Validity of the Julliere model of spin-dependent tunneling, Phys. Rev. B, 56 (1997) 11827-11832.

[53] V.A. Dediu, L.E. Hueso, I. Bergenti, C. Taliani, Spin routes in organic semiconductors, Nat. Mater. , 8 (2009) 707-716.

[54] W.P. Pratt, S.F. Lee, J.M. Slaughter, R. Loloee, P.A. Schroeder, J. Bass, Perpendicular giant magnetoresistances of Ag/Co multilayers, Phys. Rev. Lett. , 66 (1991) 3060-3063.

[55] S. Parkin, J. Xin, C. Kaiser, A. Panchula, K. Roche, M. Samant, Magnetically engineered spintronic sensors and memory, Proc. IEEE 91 (2003) 661-680.

[56] G. Schmidt, D. Ferrand, L.W. Molenkamp, A.T. Filip, B.J. van Wees, Fundamental obstacle for electrical spin injection from a ferromagnetic metal into a diffusive semiconductor, Phys. Rev. B, 62 (2000) R4790-R4793.

[57] E.I. Rashba, Theory of electrical spin injection: Tunnel contacts as a solution of the conductivity mismatch problem, Phys. Rev. B, 62 (2000) R16267-R16270.

[58] A. Fert, H. Jaffrès, Conditions for efficient spin injection from a ferromagnetic metal into a semiconductor, Phys. Rev. B, 64 (2001) 184420.

[59] I. Žutić, J. Fabian, S. Das Sarma, Spintronics: Fundamentals and applications, Rev. Mod. Phys. , 76 (2004) 323-410.

[60] A.R. Rocha, V.M. Garcia-Suarez, S.W. Bailey, C.J. Lambert, J. Ferrer, S. Sanvito, Towards molecular spintronics, Nat. Mater. , 4 (2005) 335-339.

[61] V. Krinichnyi, S. Chemerisov, Y.S. Lebedev, EPR and charge-transport studies of polyaniline, Phys. Rev. B, 55 (1997) 16233.

[62] V. Dediu, M. Murgia, F.C. Matacotta, C. Taliani, S. Barbanera, Room temperature spin polarized injection in organic semiconductor, Solid State Commun. , 122 (2002) 181-184.

[63] Z.H. Xiong, D. Wu, Z.V. Vardeny, J. Shi, Giant magnetoresistance in organic spin-valves, Nature, 427 (2004) 821-824.

[64] F. Wang, Z.V. Vardeny, Recent advances in organic spin-valve devices, Synth. Met. , 160 (2010) 210-215.

[65] F.J. Wang, Z.H. Xiong, D. Wu, J. Shi, Z.V. Vardeny, Organic spintronics: The case of Fe/Alq3/Co spin-valve devices, Synth. Met. , 155 (2005) 172-175.

[66] F.J. Wang, C.G. Yang, Z.V. Vardeny, X.G. Li, Spin response in organic spin valves based on La2/3Sr1/3MnO3 electrodes, Phys. Rev. B, 75 (2007) 245324.

[67] W. Xu, G.J. Szulczewski, P. LeClair, I. Navarrete, R. Schad, G. Miao, H. Guo, A. Gupta, Tunneling magnetoresistance observed in La0.67Sr0.33MnO3/organic molecule/Co junctions, Appl. Phys. Lett. , 90 (2007) -.

[68] H. Vinzelberg, J. Schumann, D. Elefant, R.B. Gangineni, J. Thomas, B. Buchner, Low temperature tunneling magnetoresistance on (La,Sr)MnO(3)/Co junctions with organic spacer layers, J. Appl. Phys. , 103 (2008).

[69] J.S. Jiang, J.E. Pearson, S.D. Bader, Absence of spin transport in the organic semiconductor Alq3, Phys. Rev. B, 77 (2008) 035303.

[70] J.-W. Yoo, H.W. Jang, V.N. Prigodin, C. Kao, C.B. Eom, A.J. Epstein, Tunneling vs. giant magnetoresistance in organic spin valve, Synth. Met. , 160 (2010) 216-222.

[71] J.-W. Yoo, H.W. Jang, V.N. Prigodin, C. Kao, C.B. Eom, A.J. Epstein, Giant magnetoresistance in ferromagnet/organic semiconductor/ferromagnet heterojunctions, Phys. Rev. B, 80 (2009) 205207.

[72] J.J.H.M. Schoonus, P.G.E. Lumens, W. Wagemans, J.T. Kohlhepp, P.A. Bobbert, H.J.M. Swagten, B. Koopmans, Magnetoresistance in Hybrid Organic Spin Valves at the Onset of Multiple-Step Tunneling, Phys. Rev. Lett. , 103 (2009) 146601.

[73] R. Lin, F. Wang, J. Rybicki, M. Wohlgenannt, K.A. Hutchinson, Distinguishing between tunneling and injection regimes of ferromagnet/organic semiconductor/ferromagnet junctions, Phys. Rev. B, 81 (2010) 195214.

[74] N.J. Harmon, M.E. Flatté, Spin-Flip Induced Magnetoresistance in Positionally Disordered Organic Solids, Phys. Rev. Lett. , 108 (2012) 186602.

[75] T.L.A. Tran, T.Q. Le, J.G.M. Sanderink, W.G. van der Wiel, M.P. de Jong, The Multistep Tunneling Analogue of Conductivity Mismatch in Organic Spin Valves, Adv. Funct. Mater. , 22 (2012) 1180-1189.

[76] S. Sanvito, Molecular spintronics: The rise of spinterface science, Nat. Phys. , 6 (2010) 562-564.

[77] T. Ikegami, I. Kawayama, M. Tonouchi, S. Nakao, Y. Yamashita, H. Tada, Planar-type spin valves based on low-molecular-weight organic materials with La0.67Sr0.33MnO3 electrodes, Appl. Phys. Lett. , 92 (2008) -.

[78] A. Ozbay, E.R. Nowak, Z.G. Yu, W. Chu, Y. Shi, S. Krishnamurthy, Z. Tang, N. Newman, Large magnetoresistance of thick polymer devices having La0.67Sr0.33MnO3 electrodes, Appl. Phys. Lett. , 95 (2009) -.

[79] S.S. Parkin, C. Kaiser, A. Panchula, P.M. Rice, B. Hughes, M. Samant, S.-H. Yang, Giant tunnelling magnetoresistance at room temperature with MgO (100) tunnel barriers, Nat. Mater. , 3 (2004) 862-867.

[80] V. Dediu, L.E. Hueso, I. Bergenti, A. Riminucci, F. Borgatti, P. Graziosi, C. Newby, F. Casoli, M.P. De Jong, C. Taliani, Y. Zhan, Room-temperature spintronic effects in Alq3-based hybrid devices, Phys. Rev. B, 78 (2008).

[81] D. Sun, L. Yin, C. Sun, H. Guo, Z. Gai, X.G. Zhang, T.Z. Ward, Z. Cheng, J. Shen, Giant Magnetoresistance in Organic Spin Valves, Phys. Rev. Lett. , 104 (2010).

[82] J.-W. Yoo, C.-Y. Chen, H. Jang, C. Bark, V. Prigodin, C. Eom, A. Epstein, Spin injection/detection using an organic-based magnetic semiconductor, Nat. Mater. , 9 (2010) 638-642.

[83] S. Wang, Y.J. Shi, L. Lin, B.B. Chen, F.J. Yue, J. Du, H.F. Ding, F.M. Zhang, D. Wu, Room-temperature spin valve effects in La0.67Sr0.33MnO3/Alq3/Co devices, Synth. Met. , 161 (2011) 1738-1741.

[84] A. Riminucci, M. Prezioso, C. Pernechele, P. Graziosi, I. Bergenti, R. Cecchini, M. Calbucci, M. Solzi, V. Alek Dediu, Hanle effect missing in a prototypical organic spintronic device, Appl. Phys. Lett. , 102 (2013) -.

[85] S. Watanabe, K. Ando, K. Kang, S. Mooser, Y. Vaynzof, H. Kurebayashi, E. Saitoh, H. Sirringhaus, Polaron spin current transport in organic semiconductors, Nat. Phys. , 10 (2014) 308-313.

[86] A.J. Drew, J. Hoppler, L. Schulz, F. Pratt, P. Desai, P. Shakya, T. Kreouzis, W. Gillin, A. Suter, N. Morley, Direct measurement of the electronic spin diffusion length in a fully functional organic spin valve by low-energy muon spin rotation, Nat. Mater. , 8 (2008) 109-114.

[87] L. Schulz, L. Nuccio, M. Willis, P. Desai, P. Shakya, T. Kreouzis, V.K. Malik, C. Bernhard, F.L. Pratt, N.A. Morley, A. Suter, G.J. Nieuwenhuys, T. Prokscha, E. Morenzoni, W.P. Gillin, A.J. Drew, Engineering spin propagation across a hybrid organic/inorganic interface using a polar layer, Nat. Mater. , 10 (2011) 39-44.

[88] F.J. Yue, Y.J. Shi, B.B. Chen, H.F. Ding, F.M. Zhang, D. Wu, Manipulating spin injection into organic materials through interface engineering, Appl. Phys. Lett. , 101 (2012) 022416.

[89] B.B. Chen, Y. Zhou, S. Wang, Y.J. Shi, H.F. Ding, D. Wu, Giant magnetoresistance enhancement at room-temperature in organic spin valves based on La0.67Sr0.33MnO3 electrodes, Appl. Phys. Lett. , 103 (2013) 072402.

[90] T.D. Nguyen, G. Hukic-Markosian, F. Wang, L. Wojcik, X.-G. Li, E. Ehrenfreund, Z.V. Vardeny, Isotope effect in spin response of [pi]-conjugated polymer films and devices, Nat. Mater. , 9 (2010) 345-352.

[91] S. Majumdar, H.S. Majumdar, R. Laiho, R. Österbacka, Comparing small

molecules and polymer for future organic spin-valves, J. Alloys Compd. , 423 (2006) 169-171.

[92] T.S. Santos, J.S. Lee, P. Migdal, I.C. Lekshmi, B. Satpati, J.S. Moodera, Room-Temperature Tunnel Magnetoresistance and Spin-Polarized Tunneling through an Organic Semiconductor Barrier, Phys. Rev. Lett. , 98 (2007) 016601.

[93] C. Barraud, P. Seneor, R. Mattana, S. Fusil, K. Bouzehouane, C. Deranlot, P. Graziosi, L. Hueso, I. Bergenti, V. Dediu, Unravelling the role of the interface for spin injection into organic semiconductors, Nat. Phys. , 6 (2010) 615-620.

[94] A. Droghetti, S. Steil, N. Großmann, N. Haag, H. Zhang, M. Willis, W.P. Gillin, A.J. Drew, M. Aeschlimann, S. Sanvito, M. Cinchetti, Electronic and magnetic properties of the interface between metal-quinoline molecules and cobalt, Phys. Rev. B, 89 (2014) 094412.

[95] A.H. Davis, K. Bussmann, Organic luminescent devices and magnetoelectronics, J. Appl. Phys. , 93 (2003) 7358-7360.

[96] G. Salis, S. Alvarado, M. Tschudy, T. Brunschwiler, R. Allenspach, Hysteretic electroluminescence in organic light-emitting diodes for spin injection, Phys. Rev. B, 70 (2004).

[97] E. Arisi, I. Bergenti, V. Dediu, M.A. Loi, M. Muccini, M. Murgia, G. Ruani, C. Taliani, R. Zamboni, Organic light emitting diodes with spin polarized electrodes, J. Appl. Phys. , 93 (2003) 7682-7683.

[98] E. Ehrenfreund, Z. Valy Vardeny, Organic spin-valves: from unipolar to bipolar devices, PCCP 15 (2013) 7967-7975.

[99] T.D. Nguyen, E. Ehrenfreund, Z.V. Vardeny, Spin-polarized light-emitting diode based on an organic bipolar spin valve, Science, 337 (2012) 204-209.

[100] B. Ding, Q. Song, K. Alameh, Room-temperature spin-polarized organic light-emitting diodes with a single ferromagnetic electrode, Appl. Phys. Lett. , 104 (2014) -.

[101] P.L. Burn, S.C. Lo, I.D.W. Samuel, The Development of Light‐Emitting Dendrimers for Displays, Adv. Mater. , 19 (2007) 1675-1688.

[102] C.W. Tang, S.A. VanSlyke, Organic electroluminescent diodes, Appl. Phys.

Lett. , 51 (1987) 913.

[103] Y. Liu, S.M. Watson, T. Lee, J.M. Gorham, H.E. Katz, J.A. Borchers, H.D. Fairbrother, D.H. Reich, Correlation between microstructure and magnetotransport in organic semiconductor spin-valve structures, Phys. Rev. B, 79 (2009) 075312.

[104] X. Zhang, S. Mizukami, T. Kubota, M. Oogane, H. Naganuma, Y. Ando, T. Miyazaki, Spin Transport in Co/Al2O3/Alq3/Co Organic Spin Valve, IEEE Trans. Magn. , 47 (2011) 2649-2651.

[105] Y. Zhan, I. Bergenti, L. Hueso, V. Dediu, M. de Jong, Z. Li, Alignment of energy levels at the Alq3 / La0.7Sr0.3MnO3 interface for organic spintronic devices, Phys. Rev. B, 76 (2007).

[106] Y.Q. Zhan, M.P. de Jong, F.H. Li, V. Dediu, M. Fahlman, W.R. Salaneck, Energy level alignment and chemical interaction at Alq_{3}/Co interfaces for organic spintronic devices, Phys. Rev. B, 78 (2008) 045208.

[107] K. Tarafder, B. Sanyal, P.M. Oppeneer, Charge-induced spin polarization in nonmagnetic organic molecule Alq(3), Phys. Rev. B, 82 (2010).

[108] K. Seki, E. Ito, H. Ishii, Energy level alignment at organic/metal interfaces studied by UV photoemission, Synth. Met. , 91 (1997) 137-142.

[109] M. Bowen, M. Bibes, A. Barthelemy, J.-P. Contour, A. Anane, Y. Lemaitre, A. Fert, Nearly total spin polarization in La[sub 2/3]Sr[sub 1/3]MnO[sub 3] from tunneling experiments, Appl. Phys. Lett. , 82 (2003) 233-235.

[110] H.B. Michaelson, The work function of the elements and its periodicity, J. Appl. Phys. , 48 (1977) 4729-4733.

[111] S. Yunoki, A. Moreo, E. Dagotto, S. Okamoto, S.S. Kancharla, A. Fujimori, Electron doping of cuprates via interfaces with manganites, Phys. Rev. B, 76 (2007) 064532.

[112] I.H. Campbell, T.W. Hagler, D.L. Smith, J.P. Ferraris, Direct Measurement of Conjugated Polymer Electronic Excitation Energies Using Metal/Polymer/Metal Structures, Phys. Rev. Lett. , 76 (1996) 1900-1903.

[113] M. Grobosch, K. Dörr, R. Gangineni, M. Knupfer, Energy level alignment at interfaces between organic semiconductors and clean ferromagnetic La0.7Sr0.3MnO3

thin film contacts for spin injection, Appl. Phys. A 95 (2009) 95-99.

[114] M. Stössel, J. Staudigel, F. Steuber, J. Simmerer, A. Winnacker, Impact of the cathode metal work function on the performance of vacuum-deposited organic light emitting-devices, Appl. Phys. A 68 (1999) 387-390.

[115] I. Bergenti, V. Dediu, E. Arisi, T. Mertelj, M. Murgia, A. Riminucci, G. Ruani, M. Solzi, C. Taliani, Spin polarised electrodes for organic light emitting diodes, Org. Electron. , 5 (2004) 309-314.

Chapter 2 Experimental and Measurement Methodology

2.1 Alq_3 purification

Alq_3 used in this thesis was purchased from Sigma-Aldrich. Even though it is labelled 99.9995% pure, the purchased Alq_3 brownish powder contains impurities such as water, oxygen, salts and hydroxides which can act as trapping centres affecting mobility of carriers and cause degradation of the organic semiconductor devices [1]. Therefore Alq_3 purification is an essential step prior to device fabrication and further testing.

As shown in figure 2.1, the purification apparatus consists of three parts, a vacuum pump station (A Trivac rotary pump and Turbotronik NT 10 turbo pump), two Pyrex glass tubes (one inner tube and one outer tube) and a Carbolite Furnace in a horizontal orientation. The inner tube mounted with ~1 gram material loaded into the closing end of the outer tube. The other open end of the tube was connected with the vacuum pump station and pumped down under a vacuum of $\sim 10^{-7}$ mbar. The raw material was heated in steps to ensure the rate of heating is slow enough such that the sample does not degrade until it reaches its sublimation point. The first out gassed impurity was water that evaporates at ~80 °C under the vacuum. The other impurity was excess hydroxyquinoline that is not consumed in the reaction with sublimation point of ~120 °C. Once the temperature reached ~80 °C or ~120 °C, the system was left at this temperature for about 3 hours for out-gassing until the pressure stabilized at $\sim 10^{-7}$ mbar. Alq_3 started to evaporate at the temperature of ~200 °C and deposited on the

tube. As can be seen in figure 2.1, the temperature gradient in the tube ensures any of the impurities deposit on the tube was further from the furnace than the pure material. The last main impurity was the by-product of the reaction, which degrades at the high sublimation temperature and remain in the glass boat.

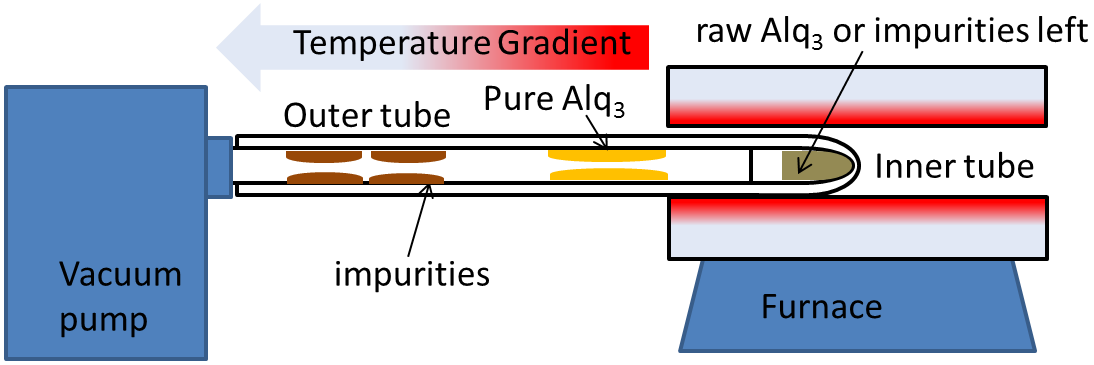

Figure 2.1: Schematic of the train sublimation process

2.2 Device fabrication

The structure of the devices used in this thesis is shown in figure 2.2, two electrodes sandwiched with one or two organic semiconductor spacers. The effective diode area is 2mm by 2mm. The metal contacts and organic semiconductors were grown by thermal evaporation on to either cleaned glass substrates or pre-patterned Indium-Tin-Oxide (ITO) substrates. With high working function and high conductivity, transparent ITO is commonly used in OLEDs as the anode. The ITO

coated glass substrates with a sheet resistance of ~13Ω/square, were purchased from Merck.

All sample preparation steps were processed in a clean room with a particle density of less than 10000p/m^3. The strictly controlled process of fabrication of organic thin film devices is essential in this experiment and will be demonstrated in the next section.

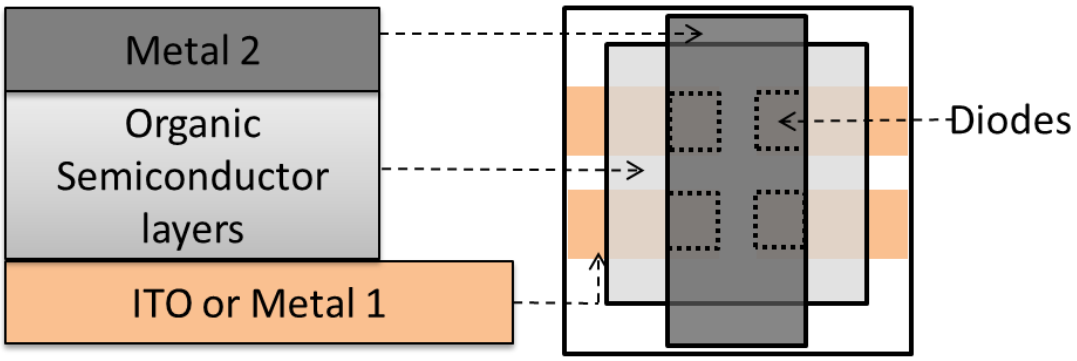

Figure 2.2: Schematic of sample structure and substrate pattern

ITO substrates were patterned with etching process. Metal or organic semiconductor layers were patterned with masks by thermal evaporation. 4 identical diodes can be fabricated in one growth.

2.2.1. Substrate cleaning

The glass substrates or ITO substrates were cut to 20mm×20mm and cleaned trough the following standard cleaning process before using.

- Scrubbed with detergent and distilled water.
- 20 minutes sonication in detergent/distilled water solution.
- 5-minute sonication in distilled water for 3 times.
- 5-minute sonication in Acetone twice.
- 5-minute sonication in Chloroform twice.
- Drying with nitrogen.

The standard clean process was used at every time before ITO substrate patterning and thin film growth.

2.2.2. ITO substrate patterning

After cleaning, the pure grass substrate is directly placed into the thin film deposition system. ITO substrates need to go through a series of photo-chemical patterning process to remove unwanted ITO and leave the electrode pattern. This process is demonstrated in figure 2.3.

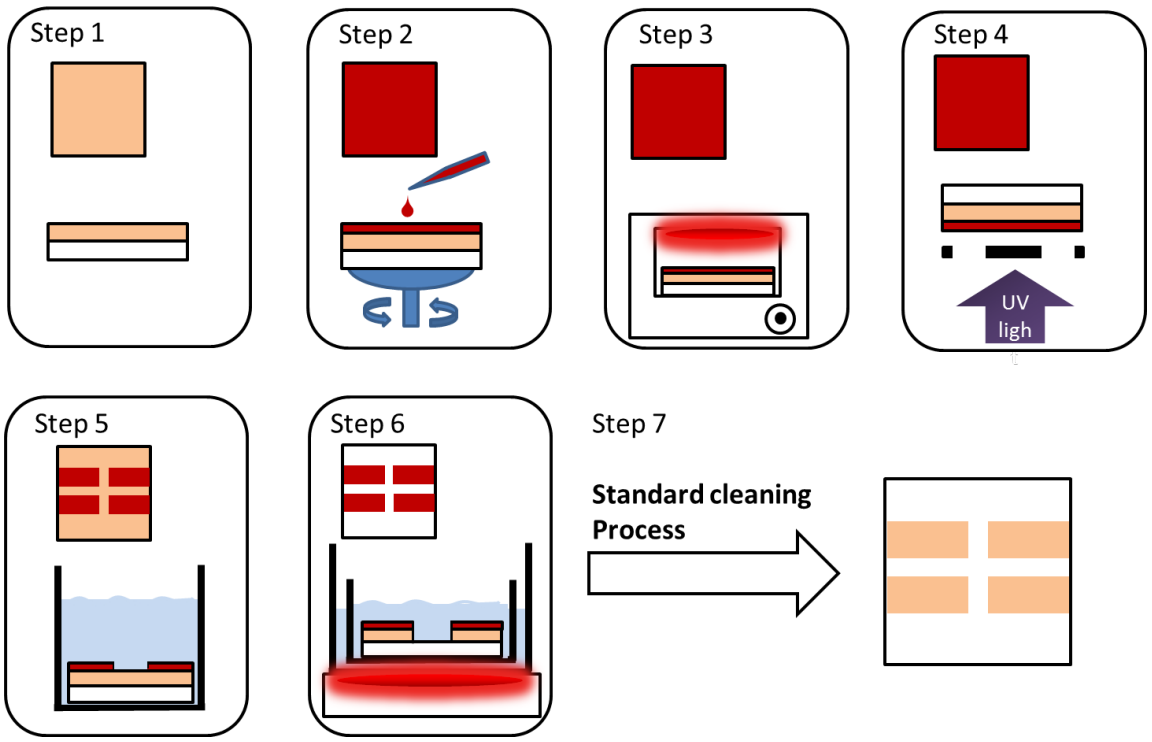

Figure 2.3: Diagram of patterning process

Step 1. Preparing a cleaned 20cm × 20cm ITO Substrate.

Step 2. Spin-casting photoresist on top of ITO substrates.

Step 3. Thermally cure the sample in an oven for 15 minutes at about 90 ℃.

Step 4. Wait for five minutes, let the sample cool down, and then cover it with the mask, exposing it to UV light for 1 minute.

Step 5. Wash the uncovered photoresist by the developer (25% NaOH and 75% distilled water) solution for two minutes, and then rinse it in the distilled water.

Step 6. Soak the substrate in the etching solution (48% HCl, 50% distilled water and 2% H_2NO_3) at 48-50℃ for one and a half minute, then rapidly transfer to the distilled water to wash away the acids.

Step 7. Clean the substrates with the standard cleaning process as descripted in previous section.

It is worth noting that, before depositing the film, the Oxygen plasma treatment was used for the patterned ITO substrates. The plasma treatment tends to remove any remaining organic residuals from the patterned ITO and increase the work function of the ITO [2]. A Deiner Electronic Femto plasma system was used. The oxygen plasma was generated at a power of 30W. The treatment time set for the ITO substrates was 4 minutes. Once the plasma treatment was complete the ITO substrate was loaded into the load lock of an evaporation system.

2.2.3. Organic and metallic deposition

As shown in figure 2.4 the evaporation system consists of two vacuum chambers one is small (a 30cm × 13cm × 9cm cuboid) and the other is big (a 66cm height and 32cm diameter cylinder); the small one acting as a load lock, used for loading the substrates to the big one, which is the main chamber. The sample loading was performed using a transfer arm. Both of the chambers can be evacuated to a pressure of around 10^{-7} mbar by scroll and turbo-molecular pumps. Five thermal sources are sited in the bottom of the main chamber, one for the metal in the centre and the other four for OSC around it (Figure 2.4). The alumina crucibles are used for organic sublimation. Titanium-diboride crucibles are used for Al sublimation and tungsten boats coated with alumina film are used for transition metals and their alloys such as Fe and NiFe. Note that LiF is deposited from an alumina crucible in one of the sources designed for organic deposition. Above the thermal sources is a four-layer cassette that contains

three masks needed for the organic and metallic layers. The bottom layer is the evaporation layer where sample on the sample holder can be loaded into and face the thermal source. The cassette can be moved in height and rotated around the axis and right mask can be loaded in the evaporation layer. This arrangement of crucibles and masks allows for all layers to be grown without breaking vacuum. As there is only one metal source, if a second metal layer is needed, the sample should be stored in the load lock when changing the metal source. Metallic and organic crucibles are resistively heated during the evaporation process and the substrate is spun to ensure a uniformed thin film growth. Deposition rate is monitored through a calibrated quartz crystal that is capable of measuring thickness to an accuracy of 0.5%.

A standard OLED used for the purpose of this research was fabricated by the following process. Firstly the 50nm TPD and 50nm Alq_3 was evaporated at the rate of 0.2nm/s using the square mask. Then the rectangular mask was replaced to deposit top metal contact Al. For the100nm Al growth, the first 10 nm was evaporated at the rate of 0.1nm/s to supress the metal inter-diffusion into the organic layer, and then a higher evaporation rate between 0.6nm/s to 1nm/s was used for the rest of the metal layer. This inter-diffusion process has not been well understood yet. One possible explanation is the hot atoms need time to ‘cool down’ by moving around when arriving at the surface of organic layer. If the evaporation rate is too high the arriving hot atoms will have no time to move around to form a uniformed film but penetrate to the bulk of the organic layer.

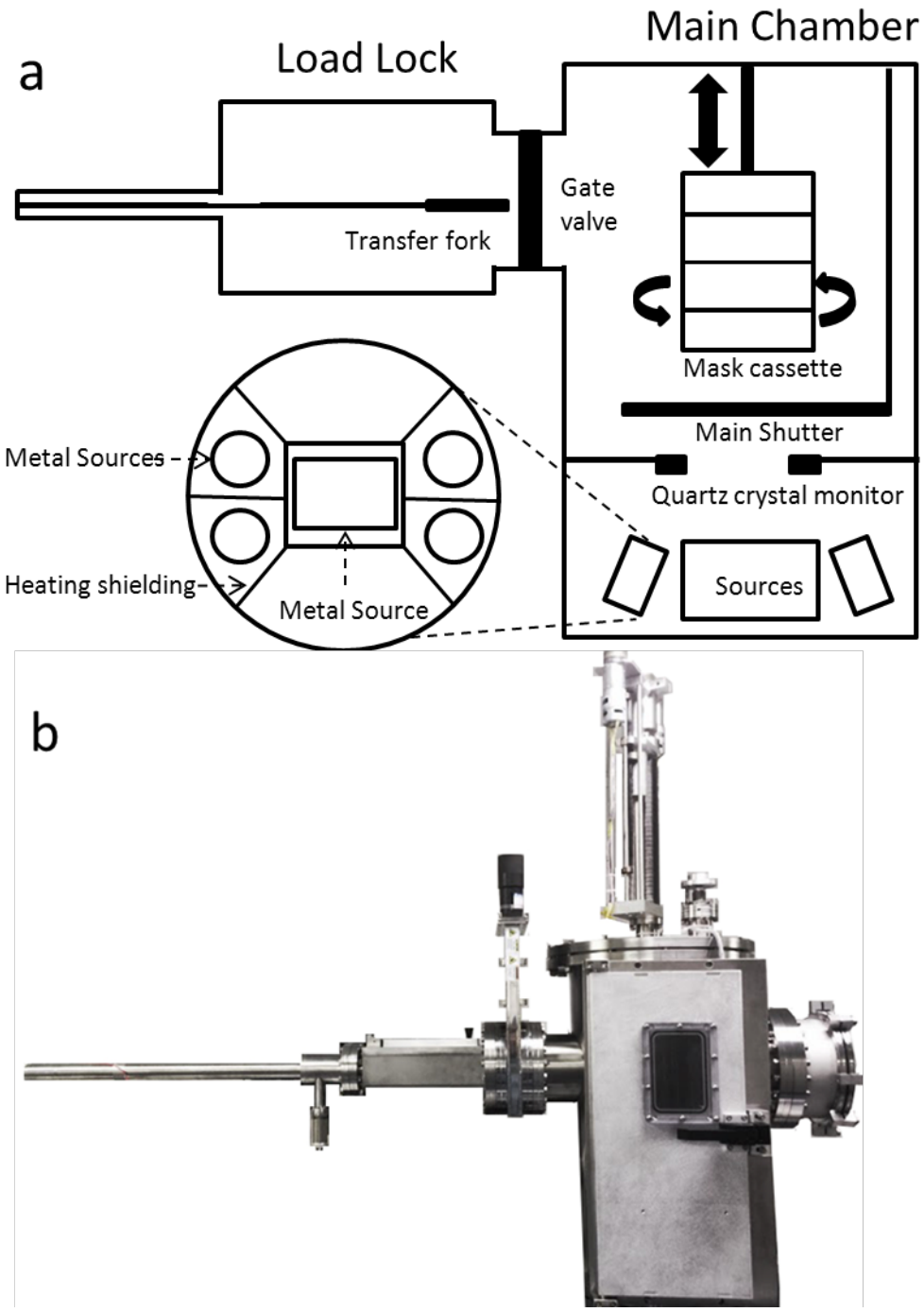

Figure 2.4: (a) The schematic and (b) the real picture of the evaporation system

In the fabrication process of OSV or OSV like devices, the transition metals NiFe, Fe or Co were required to deposit on the grass substrate or on top of the organic films. For the bottom layer deposition, a uniformed film requires a constant evaporation rate (0.4 to 0.6 nm/s). However, for the top contact deposition, the evaporation rate, the evaporation time and the evaporation distance were strictly controlled, otherwise the hot metal atoms can easily penetrate the soft organic film and short the device. As the melting point of the transition metals are as high as thousands degrees, instead of steadily increasing the power from zero, a 50% power (out of 2.0KVA transformer) that is nearly twice of Al required was suddenly applied on the tungsten boat. About 10s after the power applied, when opening the shutter, a 0.1nm/s to 0.2nm/s evaporation rate was obtained. As the power was suddenly applied, the evaporation rate was keeping increasing. Steadily adjusting the power knob and making sure the first 10nm deposition was at the rate below 1nm/s. And then increased the applied power and held the rate at about 5nm/s for 2 to 3 seconds. The total deposition time should be strictly minimized within one minute; therefore the thickness of the top transition metal was no more than 30nm and an extra Al layer were needed to act as a metal contact. Minimizing the evaporation time was the key parameter for the transition metal deposition, as to protect the vacuum break caused by over heating the main chamber.

2.3 I-V-L characterisation

The repetitive I-V-L character of the OSCs is the key factor when comparing quality of different devices. The schematic of I-V-L characterisation measurement is shown in figure 2.5. The device was housed in an evacuated sample holder to prevent any unnecessary oxidization and contaminations. A Keithley 236 source-measure unit was connected to the LEMO connector on t_0 one side of the sample holder via a triax lead. It can provide a series of constant voltages while recording the current through the device. The adapter from the triax lead to the LEMO connector was kept as short possible to minimize noise. This connection allows for measurement from 10^{-12} to 10^{-1} Amps. The device is clamped on the other side of the sample holder, which was placed in the integrating sphere. The integrating sphere is designed to produce uniform light from the device by reflection and diffusion in the sphere's internal surface. The silicon photo-detector insert in the integrating sphere can transform the photo signal to electronic signal and be measured by connected Newport 1830C optical power meter. The power meter is set to the peak wavelength of the emission spectrum of the sample. The instruments are connected to a PC that records the I-V-L characteristics measurement simultaneously.

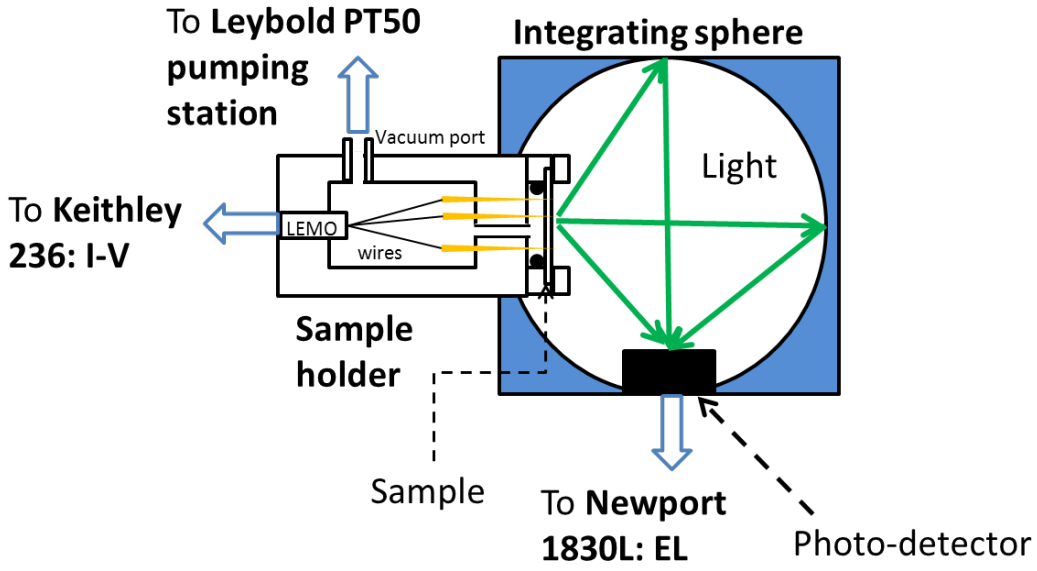

Figure 2.5: Schematic of the sample holder and I-V-L characteristics assessment system

2.4 Built-in Potential measurement

For a single layer device, the build-in potential (V_{bi}) originates from the work function difference of two electrodes in the OLED ($eV_{bi} = W_{anode} - W_{cathode}$). It can be determined using saturated photovoltaic measurement techniques [3]. The experiment setup is shown in figure 2.6a, when the OLED is irradiated with light (a 405nm laser was used), photocarriers are introduced. When there is no applied external bias, the carriers drift under the build-in electric field. As the positive bias is applied the effective voltage across the diode is $V = V_{applied} - V_{bi}$. When $V_{applied} < V_{bi}$ a negative current is obtained. As the applied bias increases, the obtained current goes to zero and turns to positive once $V_{applied} > V_{bi}$. The zero current voltage then is equal to V_{bi} of the device. A typical IV characteristic obtained in the build-in potential measurement is demonstrated in figure 2.6b. The source measure unit used in this

thesis was the Keithley 236 source-measure unit. Neutral density (ND) filters were used, in order to make sure the device was saturated with the given intensity of light. Eg. If the device is saturated, there should be no observation of a different V_{bi} with the inserting of ND filters.

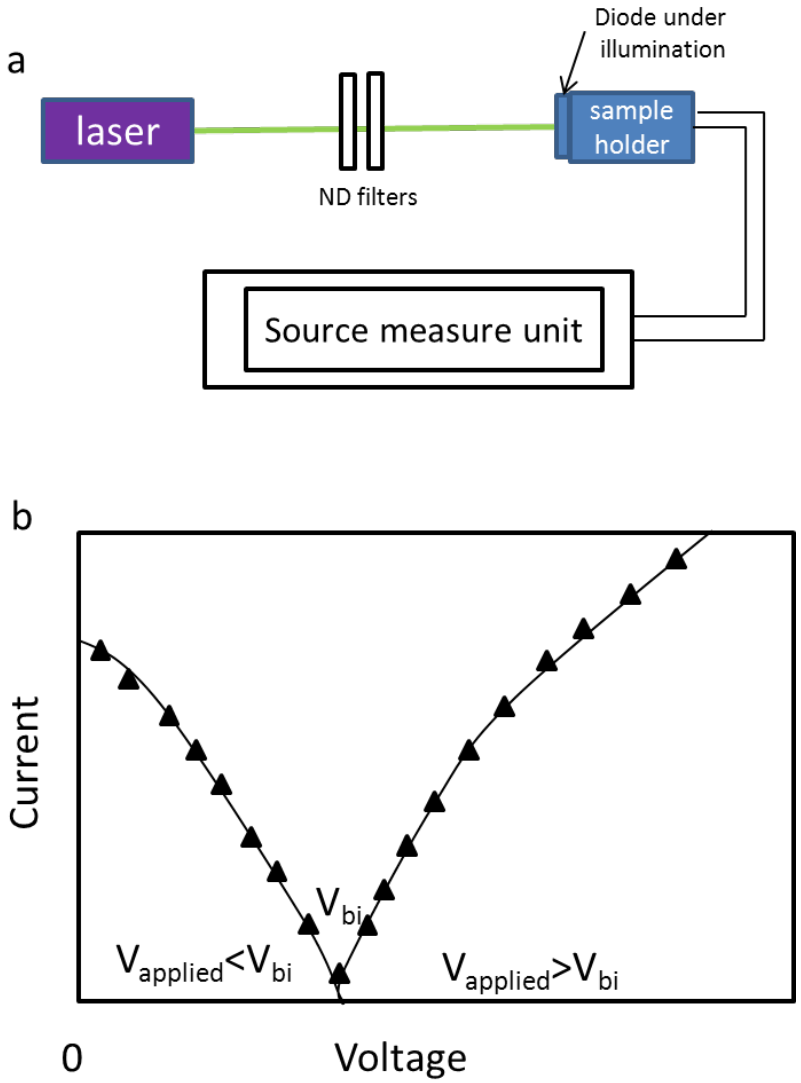

Figure 2.6: (a) A schematic setup for the build-in potential measurement of OLED. (b) A typical IV characteristic obtained in the build-in potential measurement

2.5 Photoluminescent (PL) spectra measurement

As shown in figure 2.7， in the PL measurements, the organic thin film devices were excited by the 405nm laser, and a mechanical chopper was used to provide the reference signal for the lock-in amplifier. A PerkinElmer 7265 DSP lock-in amplifier and a Thorn EMI 9202B S-20 photomultiplier tube were connected with a 550-Traix spectrometer, which collected the light emitted from the organic using a focusing lens. Suitable filters were used in between the mechanical chopper and the detector, in order to control the laser power.

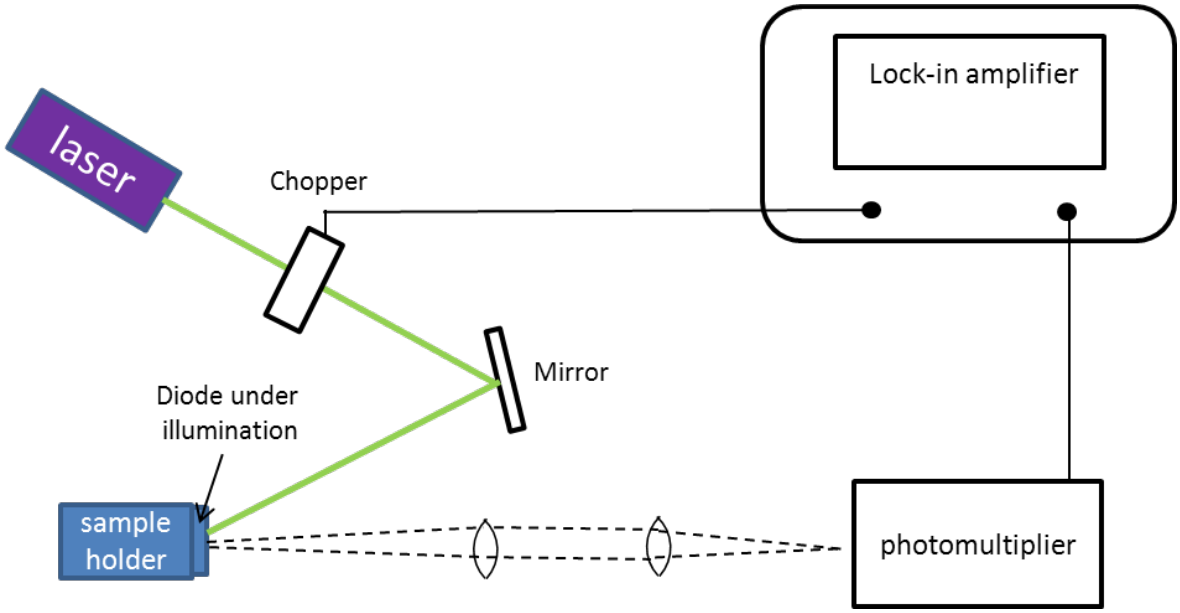

Figure 2.7: A schematic setup for the PL measurement of OLED

2.6 Time of Flight

In the ToF measurements, the sample was placed in a Linkam hot stage (TMS 94) under a constant flux of nitrogen (0.5 L/m). For the temperature dependent measurement, the temperature (ranging from 233K to 333K) can be balanced with the heated hot stage and a liquid nitrogen cryogen.

As shown in figure 2.8, batteries were used to provide constant electric fields across the sample, a frequency-tripled Big Sky ND:YAG laser with 355nm wavelength, pulse width of 0.1s and maximum output pulse energy of 20mJ was used to generate charge carriers for both electron and hole mobility measurements. As shown in figure 2.9, in order to minimize the dark current injected from the electrodes, the samples were reverse-biased with Al electrode positive charged. The current through the sample as a function of time was sensed as the voltage drop across a load resistor, and monitored by an Agilent Infiniium digitising oscilloscope, which was triggered by the laser pulse. Each photocurrent was averaged 265 times to provide a smooth signal with minimum noise. Dark currents were measured and averaged as well after the measurements of photocurrents. The final results presenting in this thesis were net photocurrents that the dark currents have been subtracted.

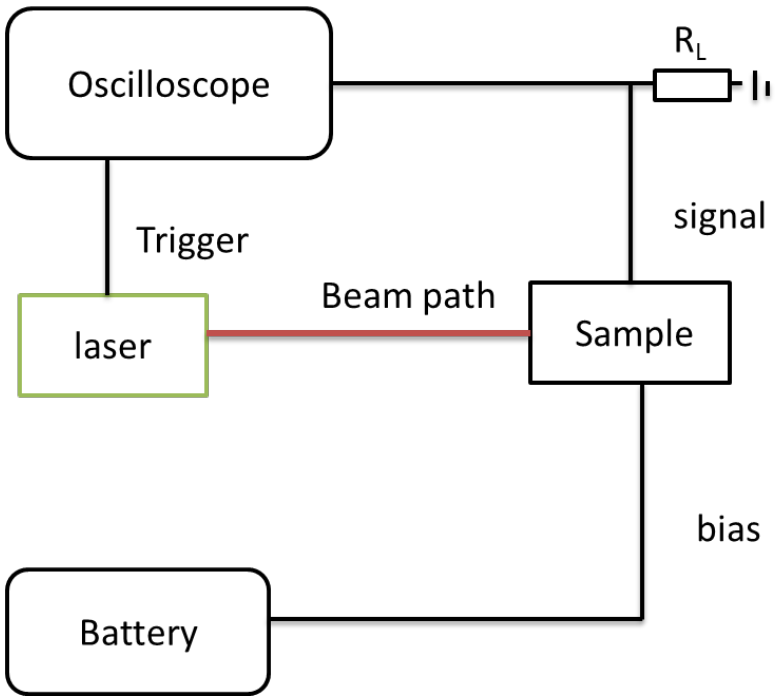

Figure 2.8: A schematic setup for the TOF measurement

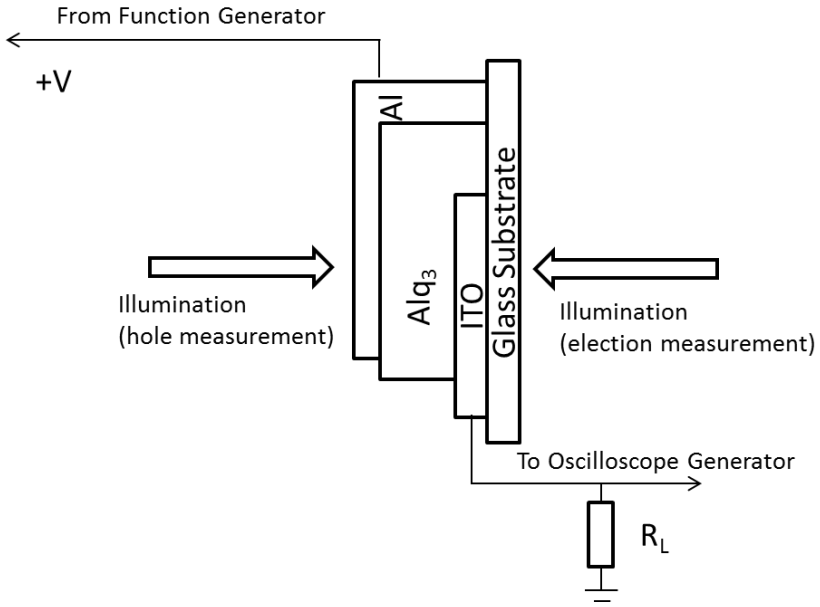

Figure 2.9: Schematic diagram of TOF experiment representing carrier transport with Al and ITO illuminated for hole and electron transport respectively.

2.7 Dark Injection

In the DI measurements, samples were placed in the Linkam hot stage as well to provide varying temperature （100K to 350K）. The experiment setup is shown in figure 2.10. A TTi (TG5011) pulse generator and high voltage amplifier (TREK model 609E-6) were connected to the substrate electrode to supply the step voltage required by the DI experiment. For the Alq_3 devices used in this thesis, 5Hz square wave with the pulse width of 100ms were applied. The charge carriers transport through the device was monitored by an Agilent infiniium oscilloscope, as the voltage drop across a load resistor.

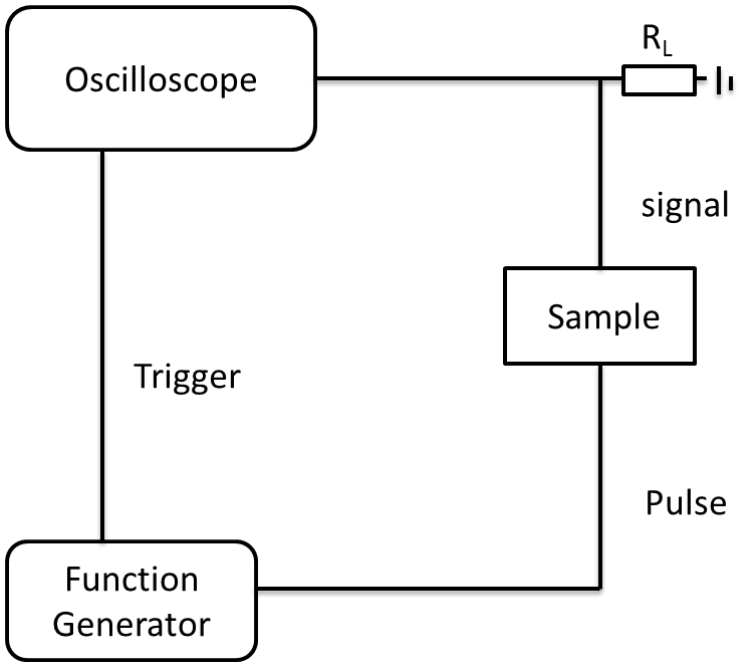

Figure 2.10: A schematic setup for the TOF measurement

2.8 Magnetoresistance measurement

The MR measurement of the spin valves used in this thesis is taken by a Cryogen-Free Measurement System, purchased from the Cryogenic Limited Company. As shown in figure 2.11, the system is comprised of 4 main components: Cryo-cooler system, Cryostat and magnet, Electronics rack, and Measurement system software.

The cooling material used in this system is helium and the temperature can be controlled between 1.6 and 325K. The cryostat is a vacuum insulated chamber whose primary function is to support and thermally shield the superconducting magnet. The magnet is solenoid wound from copper stabilized filamentary superconducting wire, which consists of NbTi and NbTi with Nb_3Sn for low field and high field magnets respectively. The magnet is able to operate in both swept and persistent mode, and can provide the magnetic field as high as 7T. The electronics rack consists of temperature controller, cryogenic superconducting magnet controller, controlling computer, and Keithly source-measure unit etc. The measurement system software is based on the Labview that provides a means of controlling the system electronics.

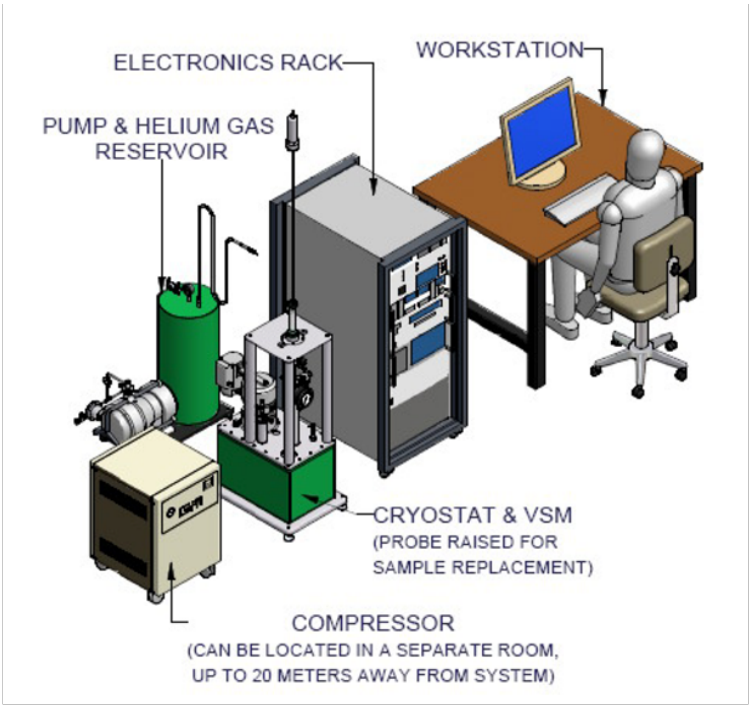

a

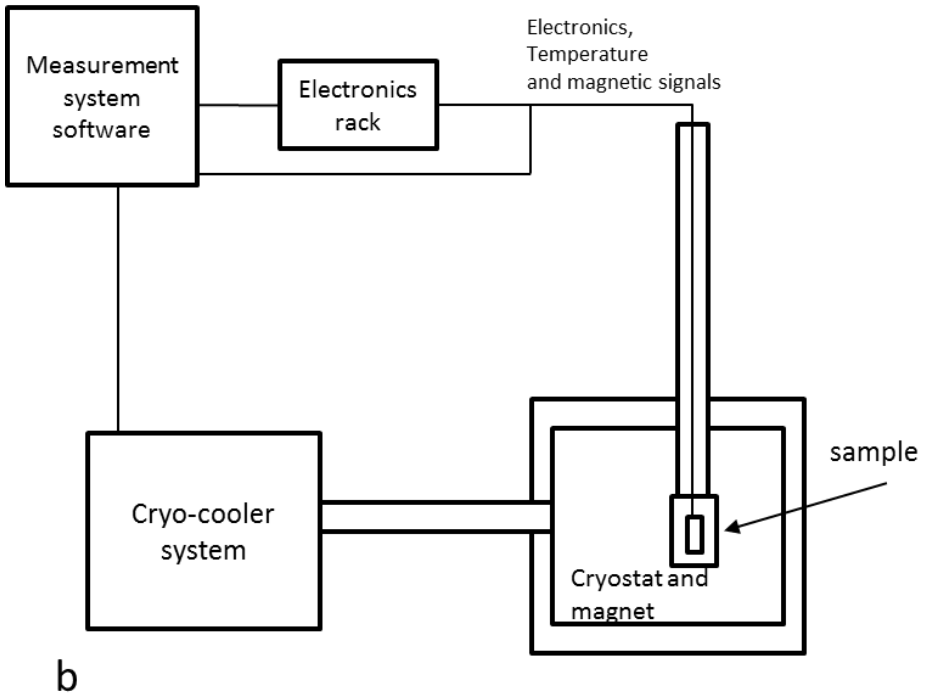

b

Figure 2.11: (a) The full Cryogen Free Measurement System (adapted from the user manual) (b) Schematic of the Measurement System consisting of the cryo-cooler system, cryostat and magnet, electronics rack and measurement system software.

As introduced in chapter 1, a standard spin valve device consists a non-magnetic spacer sandwiched by two ferromagnetic materials (FM1 and FM2). As shown in figure 2.12, FM1 and FM2 have different hysteresis loops. During the measurement, the magnetic field (B field) swept from negative to positive (B_{up}) and then swept back (B_{down}), and the corresponding "parallel" and "anti-parallel" configuration can be obtained. When applying a constant voltage on the sample, a changing of the current density can be obtained when changing the "parallel" and "anti-parallel" configuration.

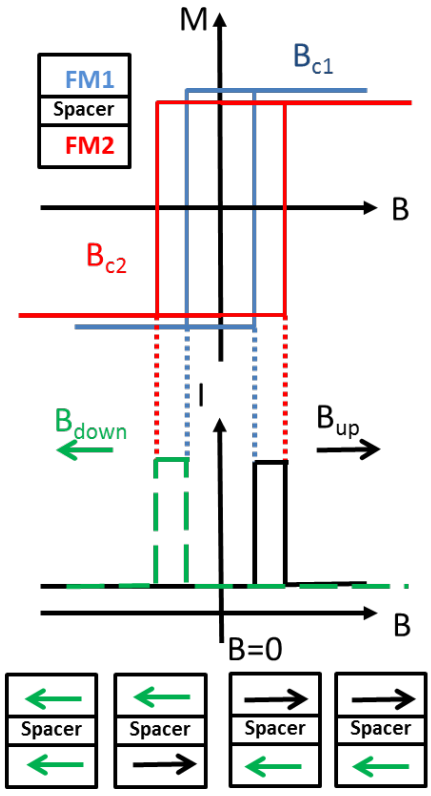

Figure 2.12: Schematic geometry of the spin valve. The parallel magnetization alignment obtained by the hysteric effect of the two ferromagnetic magnetic field. B_{c1} and B_{c2} are the coercive fields of the ferromagnetic field

References

[1] M. Schaer, F. Nüesch, D. Berner, W. Leo, L. Zuppiroli, Water Vapor and Oxygen Degradation Mechanisms in Organic Light Emitting Diodes, Adv. Funct. Mater. , 11 (2001) 116-121.

[2] C.C. Wu, C.I. Wu, J.C. Sturm, A. Kahn, Surface modification of indium tin oxide by plasma treatment: An effective method to improve the efficiency, brightness, and reliability of organic light emitting devices, Appl. Phys. Lett. , 70 (1997) 1348-1350.

[3] D. Ray, M.P. Patankar, N. Periasamy, K.L. Narasimhan, Measurement of built-in voltage of organic semiconductor devices, Synth. Met. , 155 (2005) 349-351.

Chapter 3 Hole injection and transport

3.1 OLED with Ferromagnetic cathodes

In order to get a full understanding of charge carriers injection and transport in OSVs, we have to refer to the OLEDs, which have been widely investigated for decades. Both of the devices have a sandwich structure and the current injection, transport and extraction are similar. Regardless of the requirement for the spin polarized charge current in organic spin valves, one of the main difference between the two devices is that a working OLED requires the injection of both electrons and holes.

In organic spin valves, the magnetic contacts are normally based on either $La_{0.67}Sr_{0.33}MnO_3$ (LMSO) or transition metal electrodes or their alloys, such as NiFe or FeCo [1, 2]. Regardless of any vacuum level shifts, magnetic electrodes used in organic spin valves, in particular the transition metals; generally have a high work function that will aid the hole injection. As the electron mobility in Alq_3 is much higher than hole mobility and Alq_3 is used as a electron transport layer, it is widely assumed that electrons should be the main charge carriers in Alq_3 based OSVs [3-6]. To verify if Alq_3 is capable of long range hole transport, the modified OLEDs with FM cathode (FM-OLED) were fabricated as shown in figure 3.1. The standard OLED (Al-OLED) as introduced in section 1.2.2, used ITO as the anode, 500nm TPD as the hole transport layer, 500nm Alq_3 as the electron transport layer and Al as the cathode. In the FM-OLED the cathode is replaced by the FM transition metals Co or NiFe.

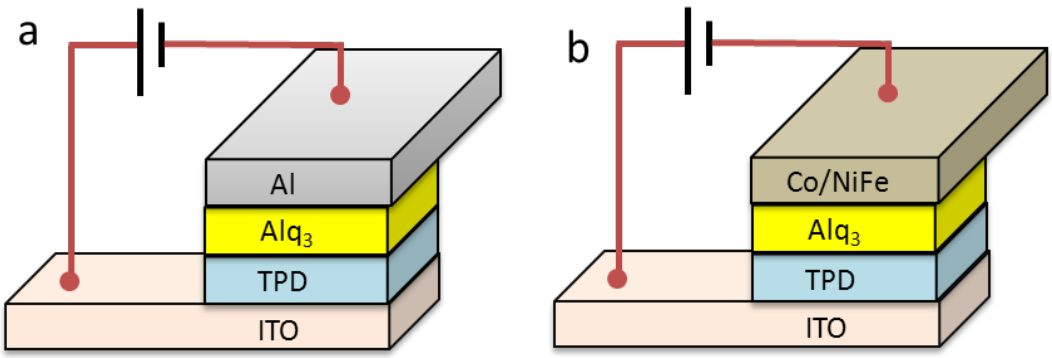

Figure 3.1: Schematic of the structure of the (a) standard OLED and (b) OLED with Ferromagnetic material cathode, Co or NiFe

Figure 3.2a shows the j-V characteristics obtained by the three OLED devices constructed using different cathode metals. In all three cases we see typical diode behaviour consisting of a small leakage current below a sharp "turn-on" point (marking the rapid rise in current with bias) where the device reaches its forward bias conducting state (that is, the current density increases by several orders of magnitude above turn-on compared to below turn-on). This "turn-on" voltage essentially corresponds to the applied voltage required to overcome the difference in the effective work function between the anode and cathode. It is noted that both the FM electrode devices show significantly reduced current densities compared to the Al device above turn–on (e.g. at 5V bias: $j_{NiFe} \sim 10$ Am^{-2} and $j_{Co} \sim 3$ Am^{-2} compared to $j_{Al} \sim 200$ Am^{-2}). Despite quantitative differences, all three devices behave as diodes. Figure 3.2b shows the L-V characteristics of the same three devices. Although the j-V characteristics of all three samples display turn-on at ~1 to 2V bias, only luminescence data from the

Al-OLED closely follows the current density, in contrast to the FM-OLEDs. Here we clearly see a large qualitative difference between the FM cathode devices and the standard Al device. Although the Al-OLED shows clearly measurable luminescence immediately after "turn-on", signifying injection of both electrons and holes and their subsequent radiative recombination, we do not observe luminescence from the FM-OLEDs until operating voltages exceed 8V. Even in this region the luminescence is very weak, at 10V it corresponds to that obtained from the Al device at an operating voltage of 2.2V which is immediately after "turn-on". This demonstrates that whilst the FM contacts used here can inject electrons into Alq_3 the magnitude of this electron injection at an operating voltage of 10V is significantly less than from the Al cathode. A simple comparison of the luminescence efficiency suggests an electron injection rate 6 orders of magnitude less than from Al.

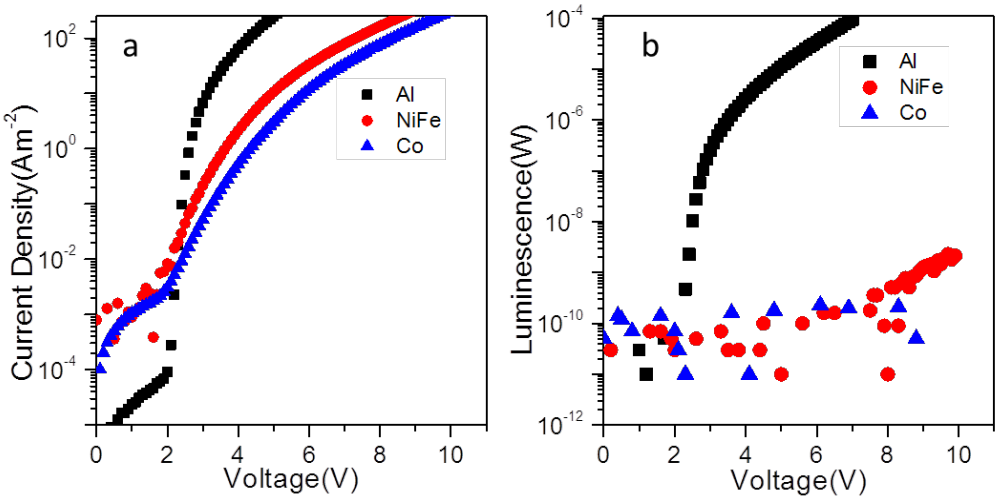

Figure 3.2: (a) The current voltage characteristics of a standard OLED (ITO-TPD(50nm) -Alq3(50nm)-Al) and OLEDs with NiFe and Co cathodes. (b) The Luminescence-Voltage characteristics for the same devices.

This is a very strong indication that NiFe and Co cathodes are poor electron injectors, acting instead to extract holes. However, it is possible that there may be electron injection but that the excitons may be quenched, possibly by in-diffusion of the contact, resulting in no visible electroluminescence. In order to ensure that this was not happening we performed photoluminescence (PL) measurements on the two OLED structures (figure 3.3). Each spectrum shows an asymmetric peak in the range 450-800 nm, with the maximum intensity at 530 nm.

If quenching were responsible for the lack of electroluminescence then it would also quench the photoluminescence. As can be seen in figure 3.3 the shape of the PL from the two structures was identical proving that the lack of electroluminescence was solely due to there being negligible electron injection.

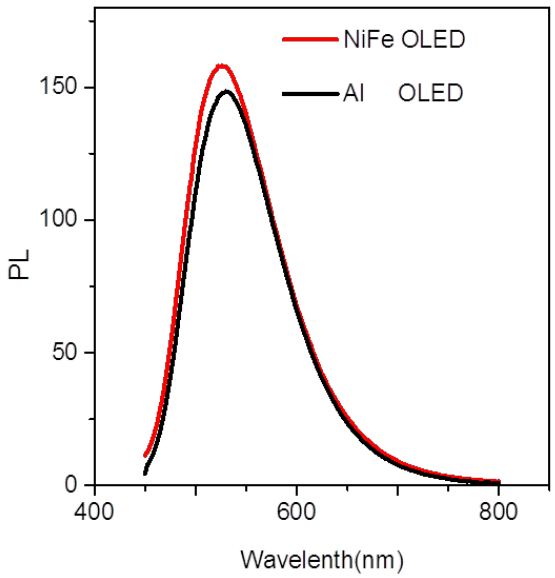

Figure 3.3: Photoluminescence spectra for OLEDs using NiFe or Al as the cathode (ITO-TPD-Alq_3-cathode)

Figure 3.4 shows the magnitude of the current obtained under steady state illumination versus bias for the three devices**.** The built in potential can be measured, under saturated illumination conditions, using the position of the minimum magnitude current obtained (that is, approximating an open circuit voltage measurement in a photovoltaic device as discussed in chapter 2 . The Al cathode device has the largest recorded work function difference (~2.25V) whereas both FM cathode devices show approximately equal and significantly reduced work function differences (~ 1.4V). This results show a ~0.85eV reduction in the built-in potential between the Al and NiFe devices. As the only change between the two structures is in the cathode material this must correspond to a ~0.85eV increase in the effective injection barrier for electrons.

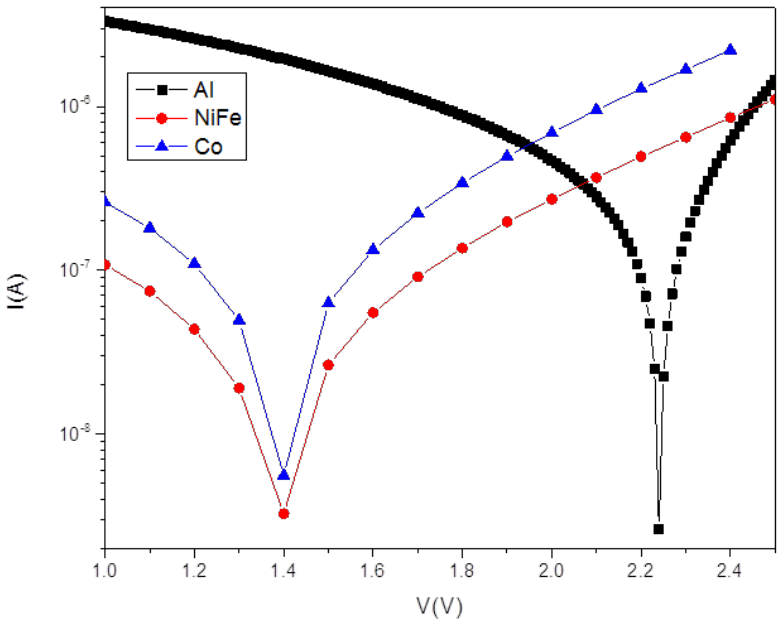

Figure 3.4: The built-in voltage measurements of the Al, NiFe and Co cathode OLEDs under illumination using ITO anode

Figure 3.5a shows a schematic representation of the injection, transport and subsequent recombination occurring in the standard device. The application of a forward bias has the effect of overcoming the injection barrier at both cathode and anode. In figure 3.5b we see a schematic representation pertaining to the NiFe cathode device. Due to the increased work function of the NiFe (Φ_{NiFe} ~5eV), compared to the Al(Φ_{Al} ~4.2eV), a modest forward bias does not achieve efficient electron injection from the cathode. This is in contrast to the hole injection which occurs efficiently from the anode and which supplies the forward current measured in figure 3.2a. We note that at very high forward bias the electric field in the device is sufficiently large that electrons begin to tunnel through the potential barrier into the Alq_3 layer resulting in the small observed luminescence shown in figure 3.2b.

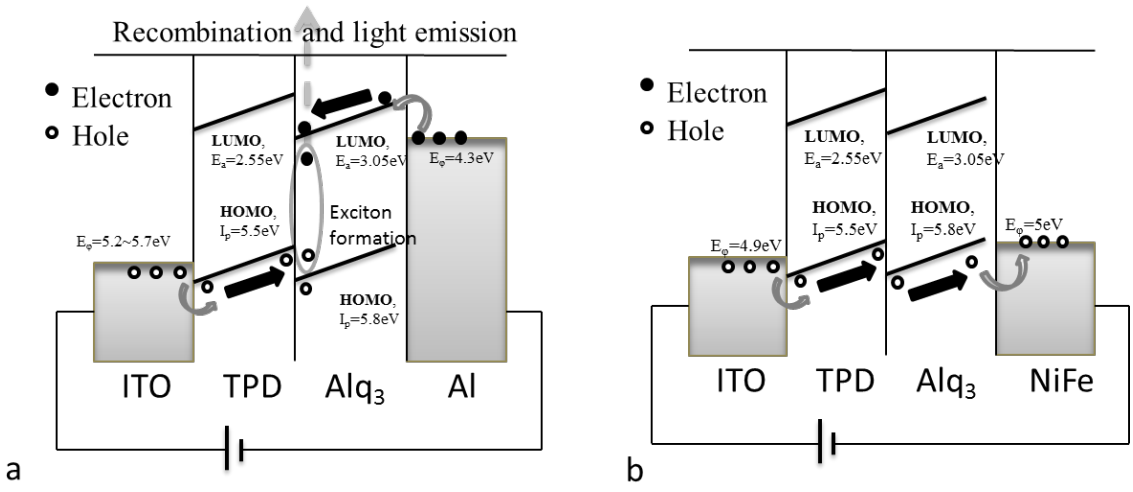

Figure 3.5: Schematics of carrier injection and transport in a (a) standard OLED with Al as cathode and (b) modified OLED with NiFe as cathode

Even thought the above experiments on OLEDs with Ferromagnetic cathodes prove

the capability of hole transport and extraction in and out of Aql_3 to NiFe or Co, there is no direct evidence showing that the injected charge carriers from ferromagnetic material into Alq_3 are holes. The issue of charge carrier type is then addressed though a study of injection and mobility of both electrons and holes in Alq_3.

3.2 Time of Flight in Alq_3

In order to measure the mobility of both electrons and holes transport in Alq_3, The ToF technique is employed on a single organic layer device, comprising ITO electrode- Alq_3 organic spacer– Al electrode. Before the mobility measurements, an I-V characteristic measurement of the device was taken and plotted in figure 3.6. As we can see, this device is behaving a typical "diode like" I-V characteristic, which is a much higher current with applied forward bias than reverse bias. This diode like IV characteristic indicates the difference of charge carrier injection barriers between ITO/Alq_3 and Al/Alq_3 interfaces, i.e. the holes are more easily injected from ITO than from Al into Alq_3, or electrons are more easily injected from Al than from ITO into Alq_3.

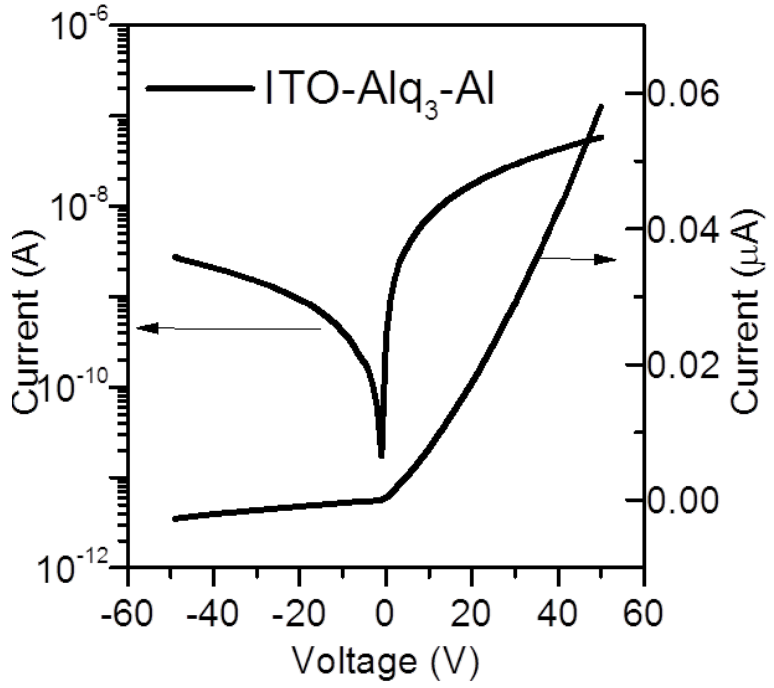

Figure 3.6: IV characteristics for the ITO-Alq_3(1.26μm)-Al device

The IV characteristics are displayed as linear and logarithmic plot, which are showing typical diode like IV.

During the ToF measurement, to minimise the dark current through the sample, the bias is always applied in reverse polarity and differentiating between carrier types is achieved by the choice of illuminated electrode. Typical hole and electron photocurrent transients obtained are shown in figure 3.7, with applied varying bias (electric field) from 18V to 92V. In the case of both type of charge carriers typical dispersive photocurrents were observed, where the fastest arrival time, t_0, is denoted by a sharp inflection point in the trace. The pre and post arrival time gradients of the double logarithmic plots are in agreement with theoretical forms and the arrival time scales as expected with increasing electric field in both cases e.g. the arrival time is

reduced from ~400µs at 18V bias for electrons to ~6µs at 92V bias and similarly for holes the arrival time is reduced from~10ms at 18 V bias to ~1ms at 92V bias. The dispersive character of charge carrier transport in Alq_3 is indicative of disordered transport states.

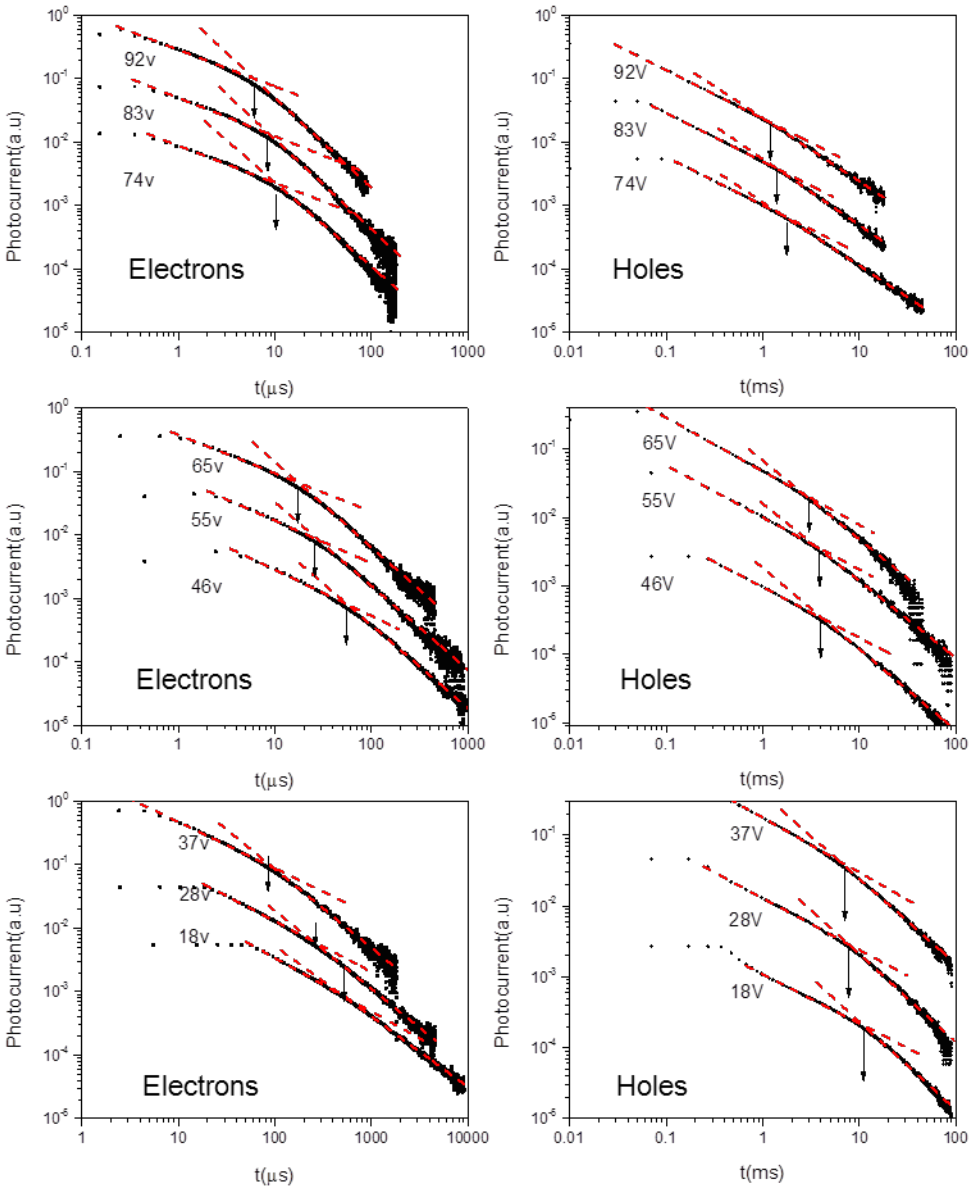

Figure 3.7: ToF photocurrent transients for the ITO-Alq_3(1260nm)-Al Device

Panels (a) (c) and (e) are electron transients and panels (b) (d) and (f) are hole transients under the bias from 18v to 92v.Arrows indicate t_{tran}

Drift velocity can be obtained using the sample thickness divided by the arrival time. The drift velocity versus electric field is plotted in Figure 3.8. The drift velocity of both type charge carriers is not simply lineally dependent on electric field and appear exponentially. This behaviour indicates that the hole and electron mobility is not constant with electric field (see chapter 2) and a Poole-Frenkel plot should be employed.

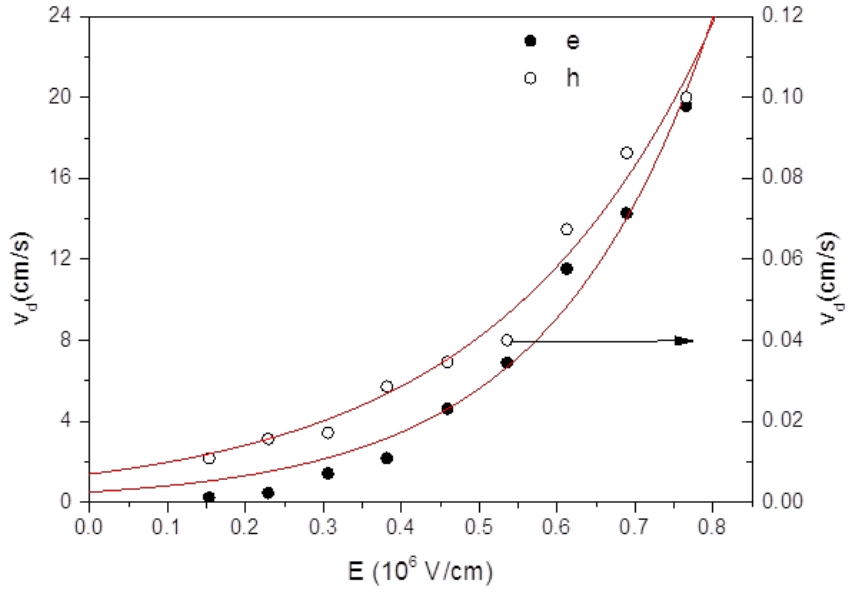

Figure 3.8: Drift velocity versus electric field

The exponential fit of this data indicates a Poole-Frenkel behavior of charge carrier transport.

The hole and electron mobilities, using the same data in figure 3.7 under varying applied bias V are calculated using Eq. (2.1) at a given field. And the results are shown in a Poole-Frenkel plot in figure 3.9. The hole mobilities obtained from these sample are ~10^{-7} cm^2/Vs and weakly electric field dependent. The electron mobilities

are more sensitive to the applied electric field and approximately one order of magnitude higher than electron mobilities at low field and two orders of magnitudes higher at high field. This result is in qualitative agreement with literature[7-9].

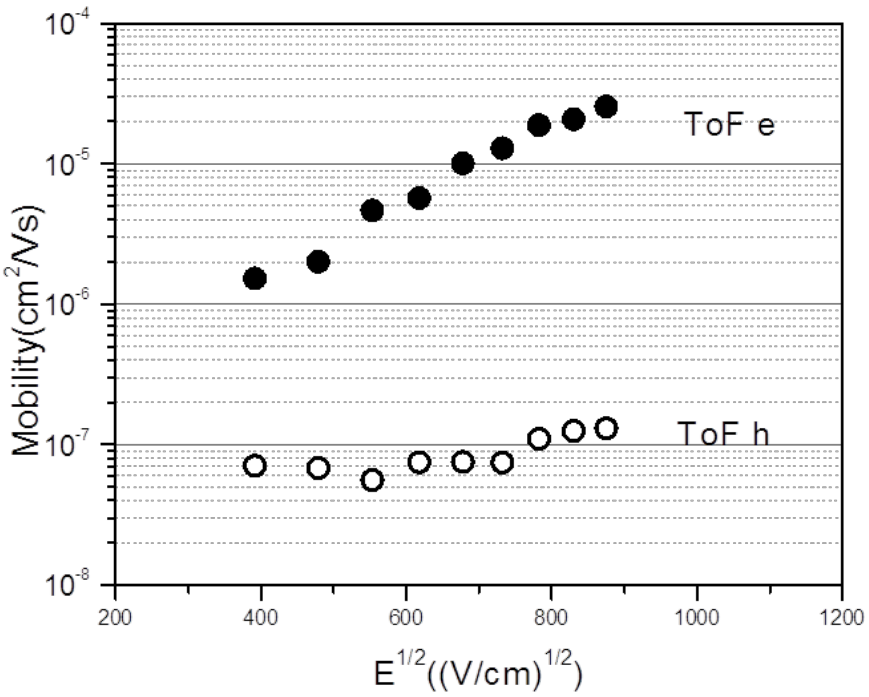

Figure 3.9: Poole-Frenkel plot of electrons and holes in Alq_3 sample

The sample thickness is 1.26μm and is measured under reverse bias.

3.3 Dark Injection in Alq_3

3.3.1 DI for Alq_3 Device with ITO and Al electrode

Whilst ToF measurements allow the direct measurement of the fastest arrival time for both electrons and holes independently, and J-V-L characteristics of modified OLEDs prove holes are more likely to be extracted by the ferromagnetic materials from Alq_3, they do not give us information on the mobility of the charge carriers injected from the electrodes. To investigate this, another mobility measurement technique DI was employed on the same structure as the device in figure 3.7, but using a thinner organic semiconductor layer (Alq_3 500nm). In order to obtain the transient response to a voltage step required for the DI measurement the sample was biased in the forward direction, as defined by the sample's diode like IV characteristics (figure 3.10). That is assuming that the ITO is acting as the anode and Al is acting as the cathode. As there is no choice of illuminated electrode, one cannot differentiate between a hole current and an electron current. The shape of the transient response of the sample and any mobility calculated from it, however, will be determined by the carrier, which is injected most efficiently.

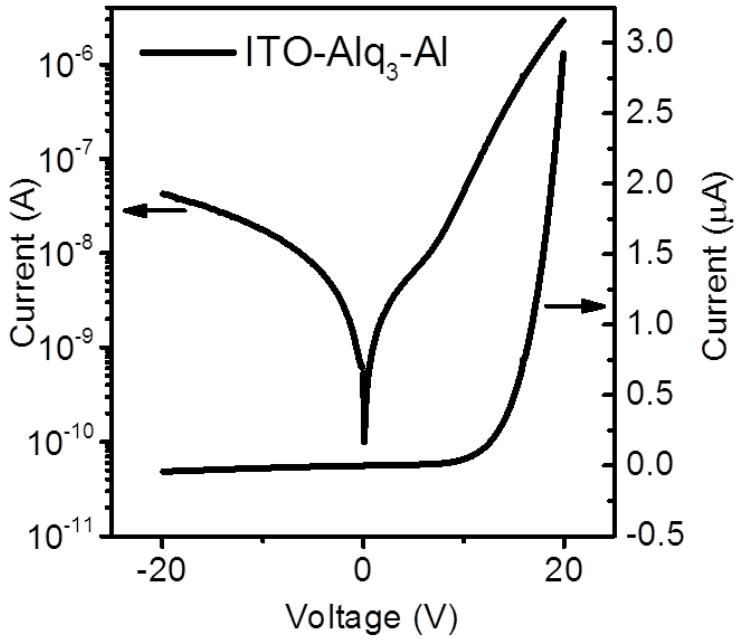

Figure 3.10: IV characteristics for the ITO-Alq_3(500nm)-Al device

The IV characteristics are displayed as linear and logarithmic plot, which are showing typical diode like IV.

In figure 3.11 are shown typical DI transients obtained from the ITO-Alq_3(500nm)-Al device. It is noted that the initial current ”spike” is due to the RC displacement current thorough the circuit (where RC<5μs) which is not resolved clearly in the timescale used. The current transients show a rise to a peak, followed by a reduction to steady state space charge limited current value, as expected from the DI measurement. The time at which the peak occurs, t_{DI}, scales correctly with increasing bias (From 6ms at 30V to 3.5ms at 50V).

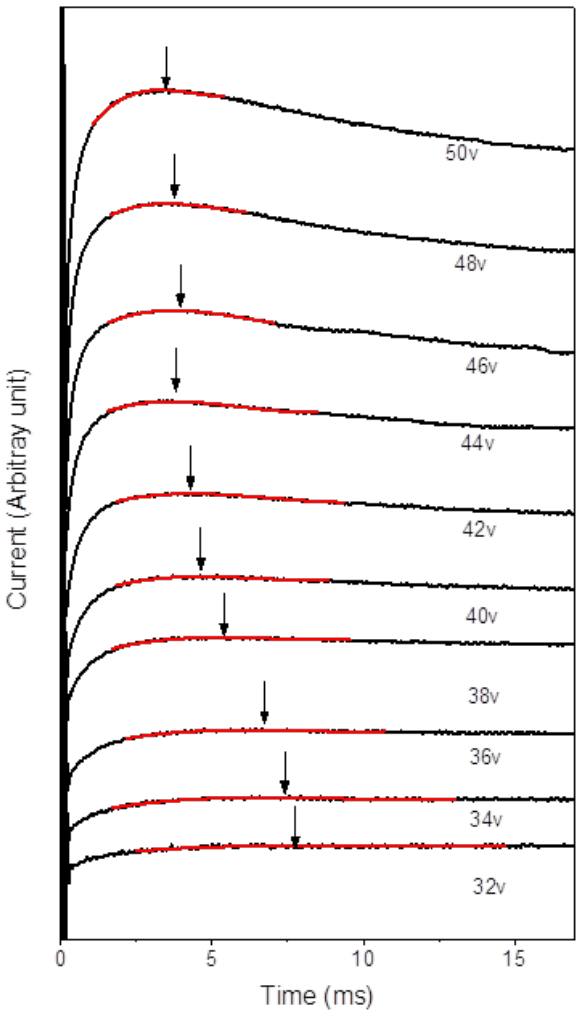

Figure 3.11: DI transit curves of the ITO-Alq_3(500nm)-Al device with applied bias voltage from 32V to 50V. Arrows indicate the t_{DI}

The DI results obtained from the ITO-Alq_3(500nm)-Al device demonstrate that charge carriers can be injected in sufficient numbers and traverse the Alq_3. Charge carrier mobilities were calculated using Eq. (2.3). A Poole-Frenkel plot of these is shown in figure 3.12. The charge carrier mobilities are about ~10^{-8} cm^2/Vs. This values are lower than the mobilities of ether holes or electrons obtained from the ToF, however the weak electric field dependence makes it more likely to correspond to hole

mobilities. More importantly, as introduced in chapter 2, for dispersive transport (as demonstrated in figure 3.7 in Alq_3), ToF can only measure the fastest arrival time of charge carriers, while the mobilities calculated from DI measurements are average values. Thus, even if both techniques are measuring the same type of charge carrier, the mobility obtained from DI should be lower than that obtained from ToF. As demonstrated in figure 3.9 the electron mobilities are varying from ~10^{-6} cm^2/Vs to ~10^{-5} cm^2/Vs, which are 2 to 3 orders of magnitude higher than the mobility obtained in DI. Such a significant difference, plus the strong field dependence makes the mobilities obtained by DI unlikely to be electron mobilities. a conclusion that charge carriers injected from ITO should be holes can be make.

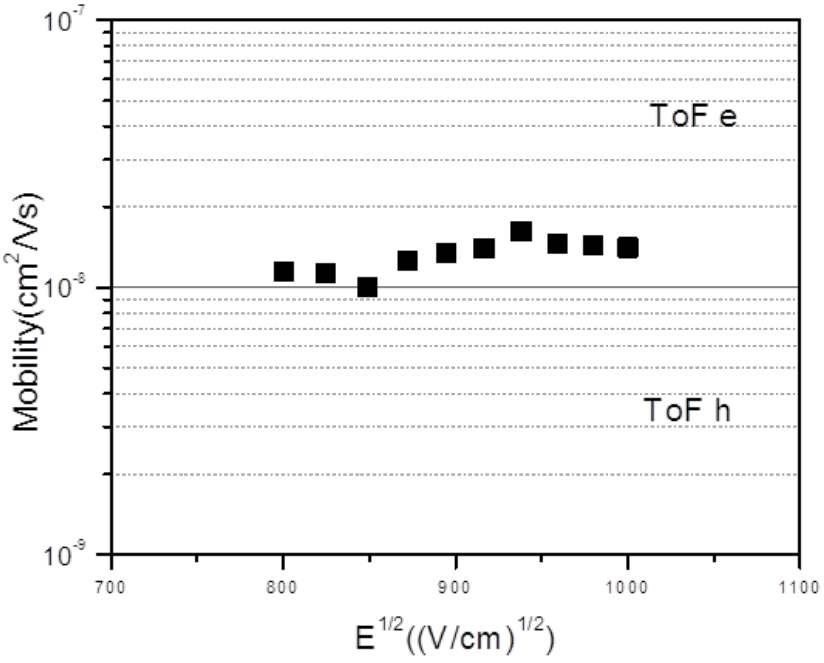

Figure 3.12: Poole-Frenkel plot of charge carriers in Alq_3 sample obtained using DI technique

The sample thickness is 500nm and measured under the varying forward bias.

3.3.2 DI for Alq_3 devices with a Ferromagnetic anode

In order to investigate the type of charge carriers injected from ferromagnetic electrodes, DI measurements were employed on the same structure Alq_3 devices using ferromagnetic material anodes, namely NiFe-Alq_3(500nm)-Al and Fe-Alq_3(550nm) -Al. The IV characteristics were taken for both devices and presented in figure 3.13. Their IV characteristics are comparable with ITO anode device results shown in figures 3.6 and 3.10, and indicate similar charge carrier injection barriers between ITO/Alq_3 and NiFe or Fe/Alq_3 interfaces.

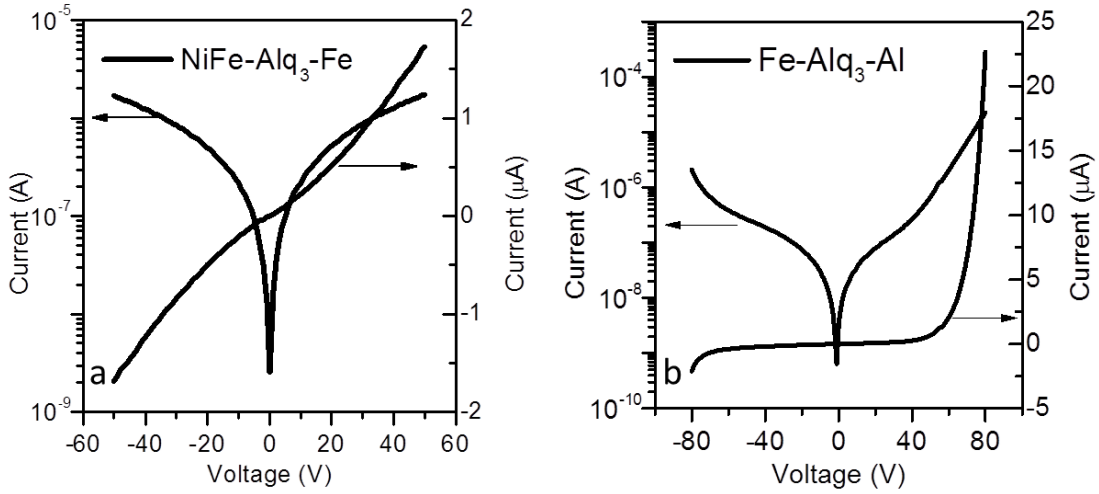

Figure 3.13: IV characteristics for the (a) NiFe-Alq_3(500nm)-Al and (b) Fe-Alq_3(500nm)-Al devices

The IV characteristics are displayed as linear and logarithmic plot for both of the devices, which are showing typical diode like IV.

Figure 3.14 (a) shows DI transient obtained from the NiFe anode device in a forward bias, i.e. hole injection from the NiFe consistent with that observed for the ITO-Alq_3(500nm)-Al device presented in Figure 3.11. At all values of bias shown

there is a long-time decay (much longer than RC<5μs) in the current, which is typical of significant charge trapping occurring within the sample[10]. The peak required to define t_{DI} only becomes evident at very high bias, which is consistent with the extraction time becoming shorter than the trapping time, or extraction rate exceeding trapping rate, as expected for DI transients in the presence of trapping. It is still possible, however, to extract a carrier mobility from such traces, albeit over a very limited range as the devices become highly unstable at high bias. Charge carrier trapping can be approximated by two sets of traps with typical trapping times of 0.24ms and 45ms. Figure 3.14(b) shows similar DI response from the Fe-Alq_3 (550nm)-Al device, which the Fe acting as the anode. Again it can be seen that the mobility is consistent with hole injection from the Fe anode.

It is worth noting that no such transient responses were obtained in reverse bias, with the only response being the RC displacement current. This means that there is no electron injection from the FM contact or hole injection from the aluminium.

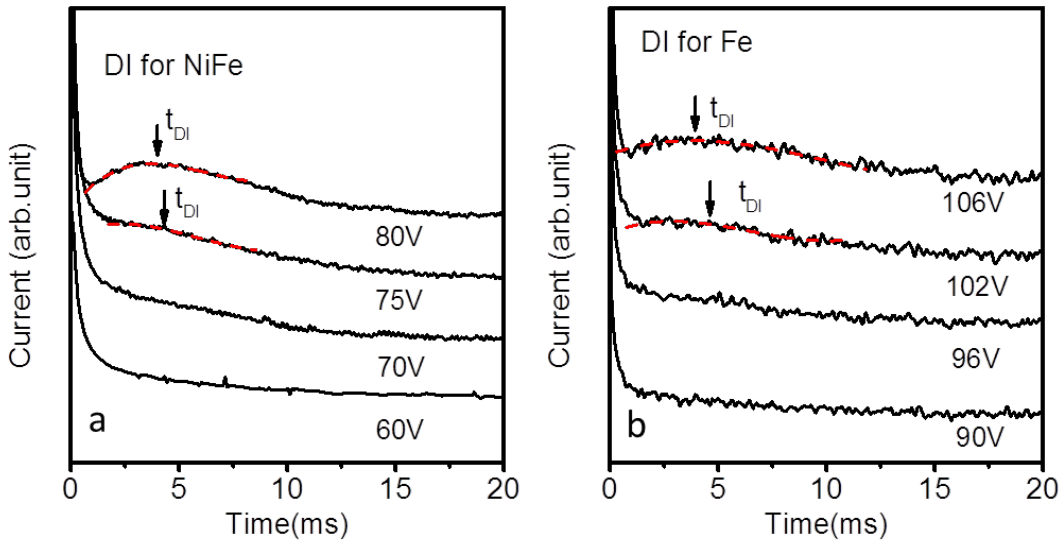

Figure 3.14: DI transit curves obtained from (a) NiFe-Alq_3(500nm)-Al device with applied bias voltage from 60V to 80V and (b) Fe-Alq_3(550nm)-Al device with applied bias voltage from 90v to 106v

3.3.3 DI for spin valve structure device

In order to confirm the hole injection and transport in a real spin valves, two real OSVs were fabricated one (NiFe-Alq_3 800nm-Fe) for dark injection and the other (NiFe-Alq_3 100nm-Fe) for MR measurements. The IV characteristics of the 800nm Alq_3 OSV were measured and shown in linear and logarithmic plots in figure 3.15. The symmetric IV characteristics indicate similar charge injection barriers are present between NiFe/Alq_3 and Alq_3/Fe. This result is consistent with the IV characteristics presenting in figure 3.13 for NiFe-Alq_3-Al and Fe-Alq_3-Al devices, in that it does not show rectification IV because of the absence of lower work function of Al.

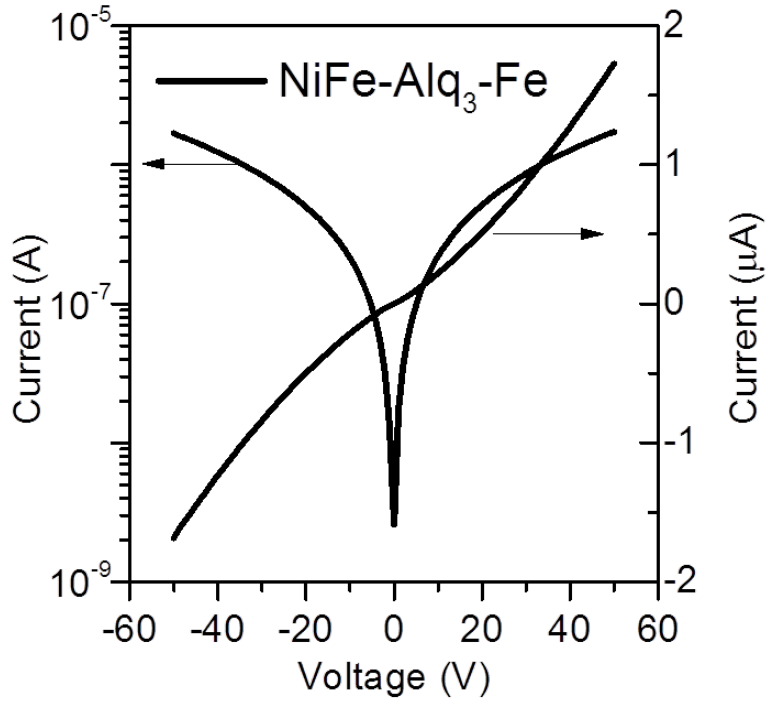

Figure 3.15: IV characteristics for the NiFe-Alq_3(800nm)-Fe device

The IV characteristics are displayed as linear and logarithmic plot, which are both symmetric in forward and reverse bias.

Figure 3.16 shows the DI transient result of this spin valve structure device. Similar to the DI transients displayed in figure 3.14 for Fe-Al and NiFe-Al electrode devices, both trapping and the presence of a t_{DI} extraction peak can be detected with the NiFe acting as the anode. This similarity confirms that carrier injection into Alq_3 does not depend on the cathode used. It is worth noting that the Fe acts as a cathode in the NiFe-Alq_3(800nm)-Fe device, in the configuration shown, yet the injected carrier mobility measured corresponds to the holes in Alq_3.

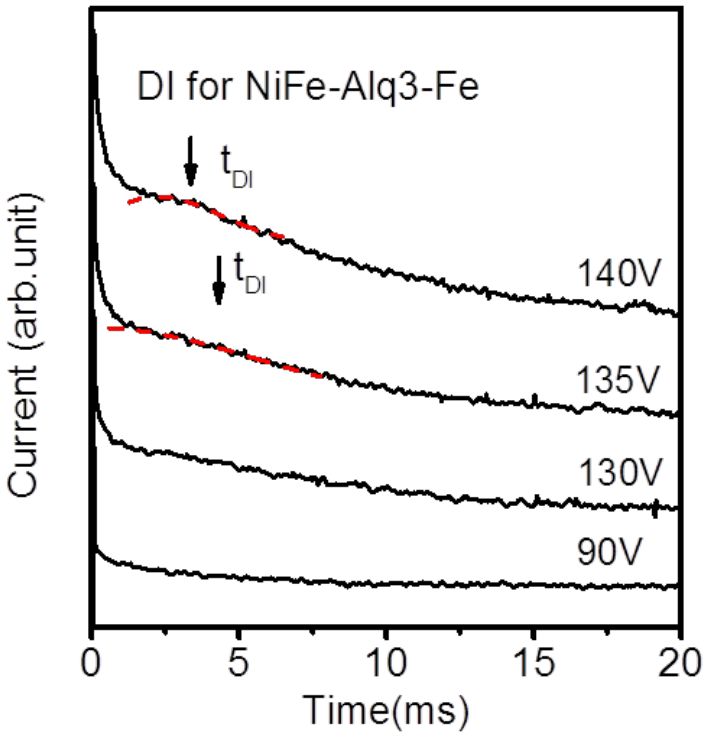

Figure 3.16: DI transit curves of the NiFe-Alq_3(800nm)-Fe device with applied bias voltage from 90V to 140V

In order to prove that this Alq_3 based OSV architecture actually works, the 100nm OSV was used. Its symmetric IV characteristic is shown in figure 3.17(a) with applied bias ranging from -50mV to 50mV at 50K. This indicates similar hole injection properties from both electrodes into Alq_3 with low applied electric field and at such low temperature. This result is consistent with 800nm device shown in figure 3.15. Figure 3.17 (b) shows 2% Magnetoresistance (spin valve effect) at 50K under 100mV bias when scanning the magnetic field between -100mT and 100mT.

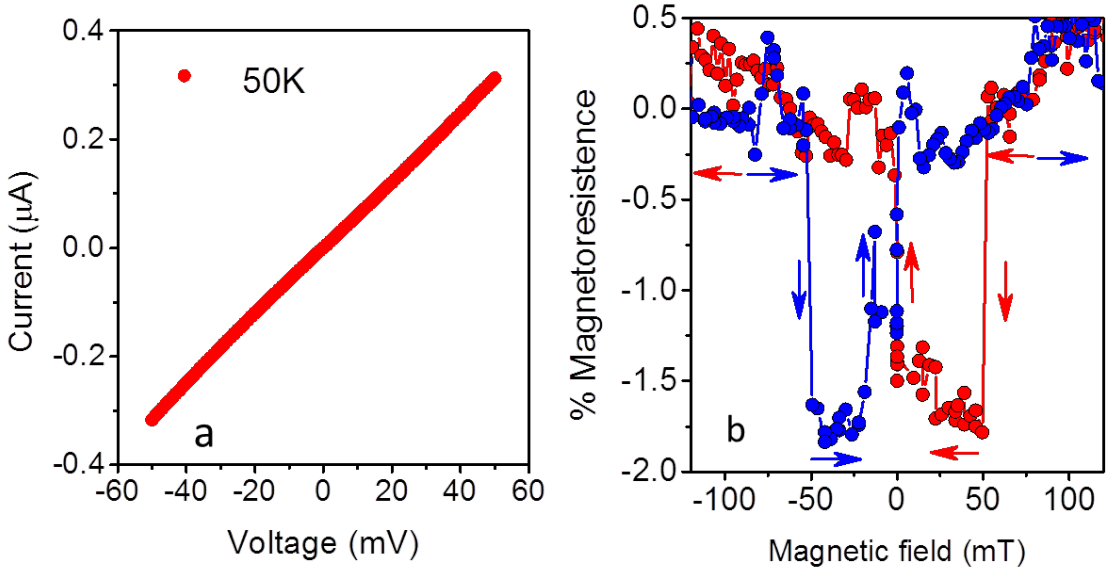

Figure 3.17: (a) Symmetric IV characteristic of a NiFe-Alq_3 (100 nm)-Fe spin valve at 50 K. (b) Magnetoresistance (spin valve effect) obtained under 30 mV bias from the NiFe-Alq_3(100 nm)-Fe spin valve at 50 K

3.4 ToF on DI devices

In order to further confirm the mobilities of both type of charge carriers in Alq_3, ToF measurements were also made on the thin devices used for DI measurements (ITO-Alq_3(500nm)-Al and NiFe-Alq_3(500nm)-Al). Typical dispersive hole and electron photocurrent transients were measured as shown in figure 3.18. Separate arrival times for electrons and holes that scale correctly with increasing electric field in both devices show similar ToF transient properties compared with thick devices present in figure 3.7.

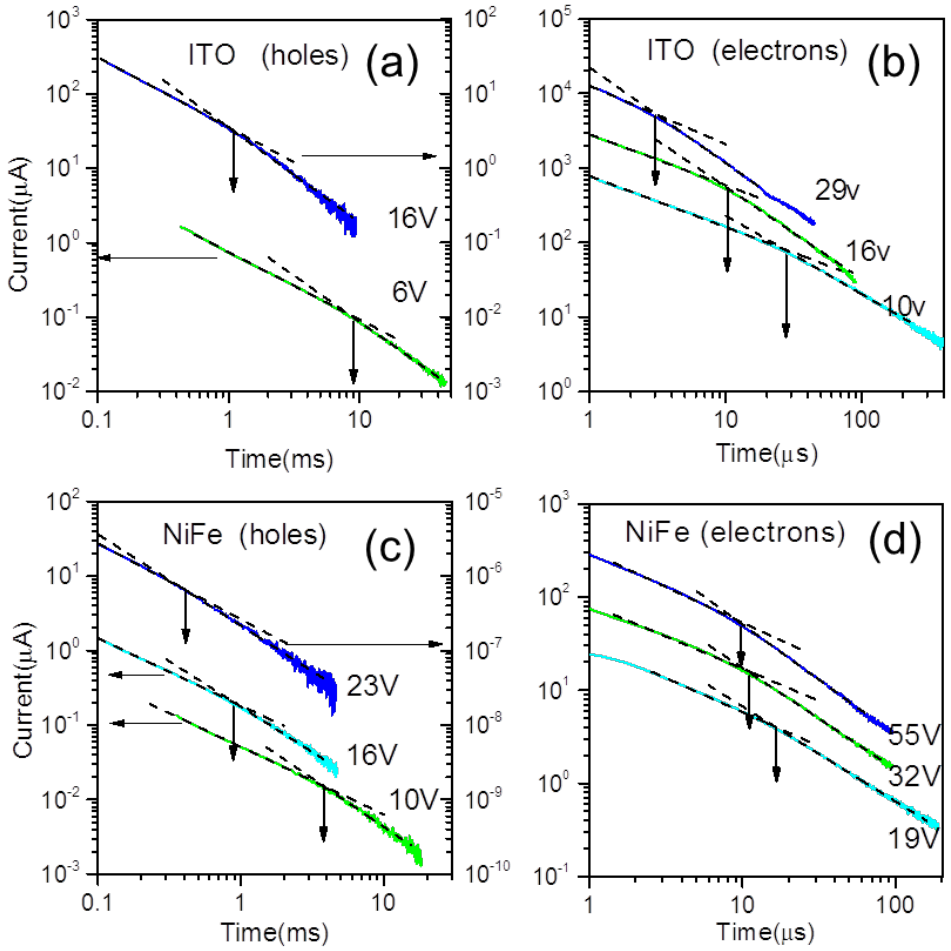

Figure 3.18: Typical ToF photocurrent transients for two Alq_3 Devices

Panels (a) and (b) are hole and electron transients for ITO-Alq_3(500nm)-Al Device. Panels (c) and (d) are hole and electron transients for NiFe-Alq_3(500nm)-Al Device. The transit time is indicated by an arrow for each photocurrent.

There is an important proviso however, due to the large absorption depth (~200nm) in Alq_3 at the 355nm laser wavelength used, these devices are ostensibly unsuitable for ToF. We have therefore calculated nominal mobilities, using an effective device thickness for charge transport of 500-200=300nm, to demonstrate the consistency of these results with the ToF data obtained in 1.2μm devices.

3.5 Discussion and Conclusions

The charge carrier mobilities obtained by ToF and DI for a large number of samples in this study (including, of course, the data from figure 3.7, figure 3.11, figure 3.14 figure 3.16 and figure 3.18) are shown as a Poole-Frenkel plot in figure 3.19. The hole mobilities obtained from these samples are approximately two orders of magnitude lower than the electron mobilities (also plotted in figure 3.19) in this material using ToF or TEL [7-9, 11-14]. As we can see, the mobilities obtained by using DI measurements for either ITO or ferromagnetic material electrode devices are consistent to each other and closer to ToF hole mobilities. The small discrepancy between DI mobility and the ToF hole mobility can be explained by the dispersive nature of the charge transport. Whereas ToF measures an upper limit on the mobility (t_0 correspond to the arrival time of the fastest carrier), DI measures an average mobility (t_{DI} is related to the average drift velocity).

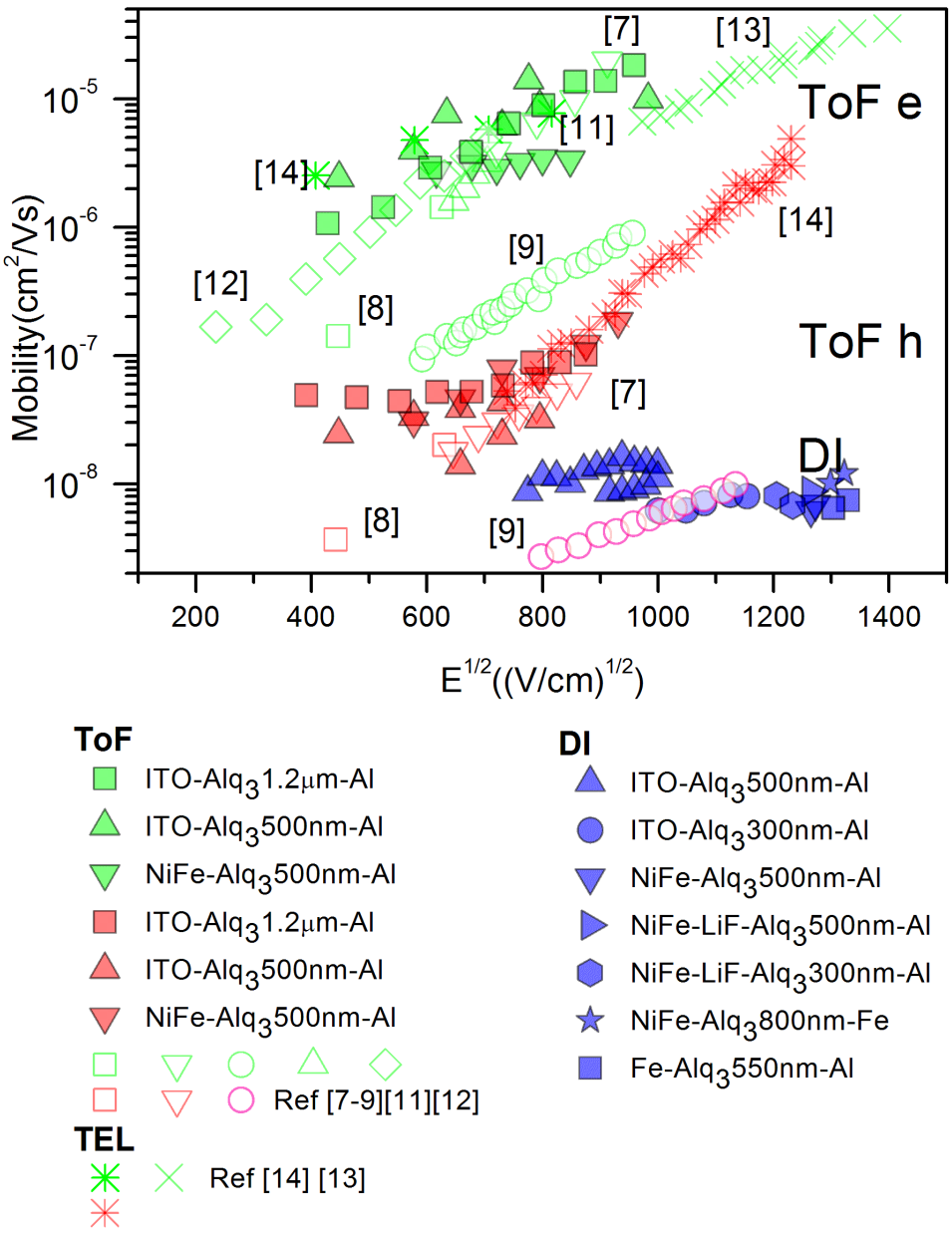

Figure 3.19: Room temperature electron (green symbols) and hole (red symbols) mobility plotted versus the square root of electric field as measured by ToF, DI (blue symbols), and TEL in a variety of Alq_3 samples (including literature data, Refs. 7-9, 11-13). The filled symbols are our data and the open symbols are taken from the literature

We accept that the mobility of holes is much lower than that of electrons, but it's what type of charge carrier is injected that matters. Unlike traditional inorganic semiconductors, OSCs are normally undoped and intrinsically semiconducting, so there should be no so-called n-type and p-type OSCs. The previous assumptions that electrons dominate spin transport in Alq_3 OSVs based on the fact of higher electron mobility are conceptually wrong [3, 4, 6, 15]. As shown in figure 3.20, the particular type of charge carrier is injected depends on both the electrode material and the OSC, thus the alignment between the Fermi level of the electrode material and the HOMO and LUMO of the OSC. For OSVs the metal contacts are usually transition metals or their alloys such as the NiFe and Fe used in this thesis, which generally have a high work function. Regardless of the vacuum level shifts, Fermi level of NiFe or Fe is closer to the HOMO of the Alq_3 and the hole injection barrier is lower than the electron injection barrier (figure 3.20). Therefore holes are more likely to be injected with applied voltage.

In the DI experiment, we observed no electron injection in both FM-Alq_3-Al and ITO-Alq_3-Al devices with either forward or reverse bias by using DI technique. As DI is a space charge limited mobility measurement technique that requires high efficient charge carrier injection, the obtained transient peaks of holes in both devices indicate both ITO and FM electrodes are capable of efficient hole injection that is contradicting to previous assumptions.

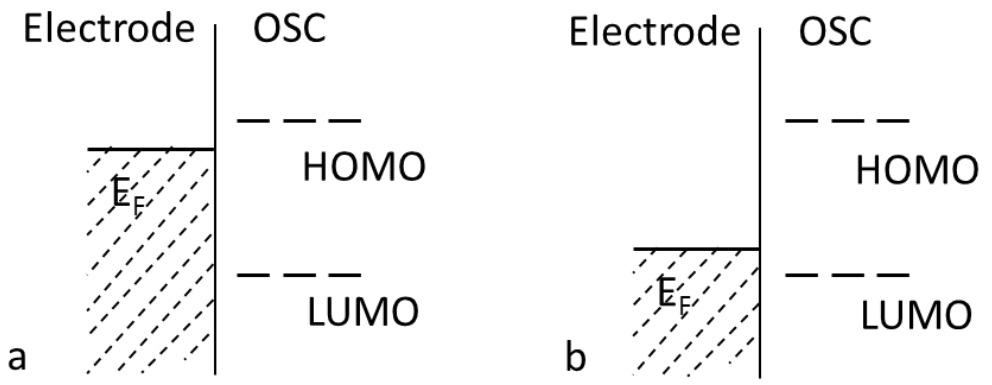

Figure 3.20: Schematic of energy level alignment between electrode E_F and OSC HOMO and LUMO

(a) low work function electrode that prefer to inject electrons into OSC, (b) high work function electrode that prefer to inject holes into OSC

In summary, the J-V-L data presented in figure 3.2 show that NiFe cannot effectively inject electrons into Alq_3 even under high bias. This is due to large work function of NiFe, approximately 0.85eV larger than that of Al, as indicated by the built in potential measurement (figure 3.4). It also shows that NiFe can extract holes from the HOMO of Alq3. Then, by comparing mobilities obtained by DI and ToF for ITO, NiFe and Fe anode devices respectively, we observed that just as ITO, both NiFe and Fe are good hole injectors. Furthermore, Alq_3 is perfectly capable of long range hole transport, albeit with reduced mobility compared to electrons (figure 3.19). This conclusion is further confirmed with similar measurements taken on a real OSV structure device that was fabricated with two ferromagnetic electrodes NiFe and Fe. Given this and the large work functions of both Fe and NiFe, we conclude that the dominant carriers injected from Fe and NiFe into Alq_3 are holes and not electrons.

References

[1] M. Bowen, M. Bibes, A. Barthelemy, J.-P. Contour, A. Anane, Y. Lemaitre, A. Fert, Nearly total spin polarization in La[sub 2/3]Sr[sub 1/3]MnO[sub 3] from tunneling experiments, Appl. Phys. Lett. , 82 (2003) 233-235.

[2] L. Schulz, L. Nuccio, M. Willis, P. Desai, P. Shakya, T. Kreouzis, V.K. Malik, C. Bernhard, F.L. Pratt, N.A. Morley, A. Suter, G.J. Nieuwenhuys, T. Prokscha, E. Morenzoni, W.P. Gillin, A.J. Drew, Engineering spin propagation across a hybrid organic/inorganic interface using a polar layer, Nat. Mater. , 10 (2011) 39-44.

[3] V.A. Dediu, L.E. Hueso, I. Bergenti, C. Taliani, Spin routes in organic semiconductors, Nat. Mater. , 8 (2009) 707-716.

[4] X. Zhang, S. Mizukami, T. Kubota, M. Oogane, H. Naganuma, Y. Ando, T. Miyazaki, Spin Transport in Co/Al2O3/Alq3/Co Organic Spin Valve, IEEE Trans. Magn. , 47 (2011) 2649-2651.

[5] J.-W. Yoo, H.W. Jang, V.N. Prigodin, C. Kao, C.B. Eom, A.J. Epstein, Giant magnetoresistance in ferromagnet/organic semiconductor/ferromagnet heterojunctions, Phys. Rev. B, 80 (2009) 205207.

[6] V. Dediu, L.E. Hueso, I. Bergenti, A. Riminucci, F. Borgatti, P. Graziosi, C. Newby, F. Casoli, M.P. De Jong, C. Taliani, Y. Zhan, Room-temperature spintronic effects in Alq3-based hybrid devices, Phys. Rev. B, 78 (2008).

[7] S. Naka, H. Okada, H. Onnagawa, Y. Yamaguchi, T. Tsutsui, Carrier transport properties of organic materials for EL device operation, Synth. Met. , 111 (2000) 331-333.

[8] R.G. Kepler, P.M. Beeson, S.J. Jacobs, R.A. Anderson, M.B. Sinclair, V.S. Valencia, P.A. Cahill, Electron and hole mobility in tris (8-hydroxyquinolinolato-N1, O8) aluminum, Appl. Phys. Lett. , 66 (1995) 3618-3620.

[9] H.H. Fong, S.K. So, Hole transporting properties of tris(8-hydroxyquinoline) aluminum (Alq[sub 3]), J. Appl. Phys. , 100 (2006) 094502.

[10] A. Many, G. Rakavy, Theory of transient space-charge-limited currents in solids

in the presence of trapping, Phys. Rev., 126 (1962) 1980.

[11] T. Tsutsui, H. Tokuhisa, M. Era, Charge carrier mobilities in molecular materials for electroluminescent diodes, Polymer Photonic Devices, 3281 (1998) 230-239.

[12] R.L. Martin, J.D. Kress, I.H. Campbell, D.L. Smith, Molecular and solid-state properties of tris-(8-hydroxyquinolate)-aluminum, Phys. Rev. B, 61 (2000) 15804-15811.

[13] H. Park, D.-S. Shin, H.-S. Yu, H.-B. Chae, Electron mobility in tris(8-hydroxyquinoline)aluminum (Alq[sub 3]) films by transient electroluminescence from single layer organic light emitting diodes, Appl. Phys. Lett. , 90 (2007) 202103.

[14] A.G. Mückl, S. Berleb, W. Brütting, M. Schwoerer, Transient electroluminescence measurements on organic heterolayer light emitting diodes, Synth. Met. , 111–112 (2000) 91-94.

[15] Y. Liu, S.M. Watson, T. Lee, J.M. Gorham, H.E. Katz, J.A. Borchers, H.D. Fairbrother, D.H. Reich, Correlation between microstructure and magnetotransport in organic semiconductor spin-valve structures, Phys. Rev. B, 79 (2009) 075312.

Chapter 4 Temperature dependent charge transport results for Alq_3

4.1 Hybridized interface states (HINTS)

Chapter 3 presents a comprehensive charge carrier transport analysis of Alq_3 based devices with ITO and ferromagnetic electrodes. We conclude that holes act as the dominant charge carriers with respect to injection and transport processes in Alq_3 based OSVs. However, even though both ITO and ferromagnetic electrodes are capable of hole injection, they demonstrate different DI transient responses (figure 3.11 and figure 3.14).

Taking ITO-Alq_3-Al and NiFe-Alq_3-Al samples that only differ in their anode materials (as shown in figure 4.1), the sample with the ferromagnetic anode shows significant trapping of injected holes. In contrast, in the ITO anode sample, the decay of the initial current is only limited by the RC response of the system (RC<5μs). This RC response is determined by the capacitance of the device (~0.5*pF*) and the sum of the resistances found in the measuring circuit (including load resistor R_L). For the NiFe sample, there is a long-time decay (two orders of magnitude lager than RC time constant) in the current, which is due to hole trapping (figure 4.1 inset).

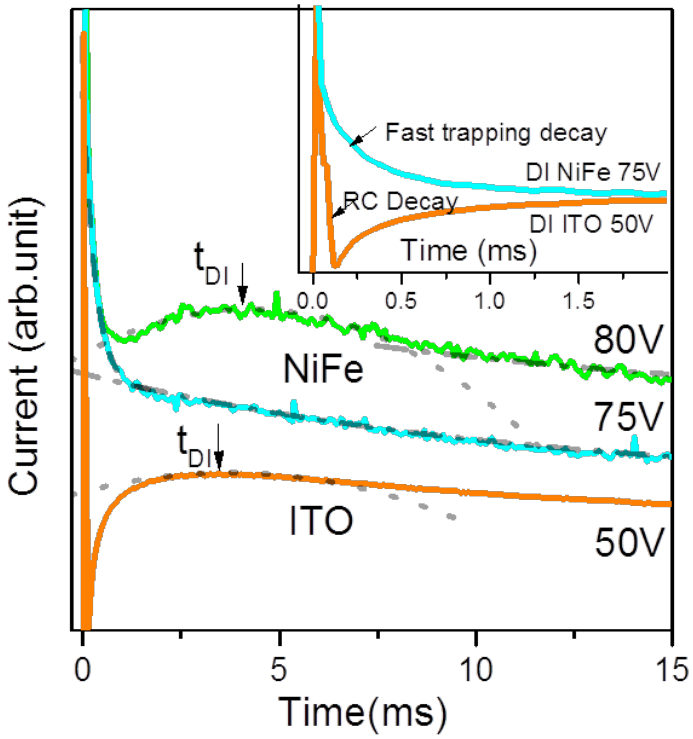

Figure 4.1: DI transient response obtained from a ITO-Alq_3(500nm)-Al device with an applied bias of 50V and a NiFe-Alq_3(500nm)-Al device with an applied bias of 75V and 80V. The inset shows the electronic (RC) and trapping decays during the first millisecond of current transient for both devices

The presence of trapped holes in the NiFe-Alq_3-Al devices was probably brought by the filled hybridised interface states (HINTS) introduced in chapter 1. The absence of these HINTS in the ITO-Alq_3-Al devices suggests that they are only present when ferromagnetic contacts are used. As the NiFe layer was deposited first, onto a glass substrate, and the subsequent device deposition was identical for both of the devices, the HINTS are intrinsic to the ferromagnetic material-organic semiconductor interface, and not formed due to penetration of ferromagnetic contact.

4.2 HINTS quantification

It would be useful to quantify the amount of trapped charge carriers, where trapping is present. The number of trapped charge carriers can be compared to the number of the HINTS that could be present. In order to determine whether occupied HINTS could be responsible for trapping, assuming the HINTS are occupied by trapped charge carriers, and then if the number of HINTS is physical, one can calculate interfacial potential decreases, due to HINTS filling in the absence of a DI measurement.

The electric current I is defined as the rate at which charge Q flows through a given surface as:

$$I = \frac{dQ}{dt} = \frac{edN}{dt} \qquad (4.1)$$

Where e is the charge of a single charge carrier (1.6×10^{-19}C) and N is the number of the charge carriers. Thus the number of charge carriers can be obtained simply by:

$$N = \frac{1}{e}\int_0^t I \cdot dt \qquad (4.2)$$

As shown in figure 4.2, the DI transient response is recording the electric current versus time. In order to quantify the trapped charges in the NiFe-Alq_3-Al device, using equation 4.2, we integrated the current with respect to time from 0 to t_{trap} and

from 0 to t_{tran}. The time t_{trap} was chosen as the time when trapping rate become smaller than the de-trapping rate. t_{tran} (t_{tran} =t_{DI}/0.79) was used to calculate the total number of charge carriers present when the front edge of charge carriers arrived at the opposite electrode.

We obtained the number of trapped charges $N_{trapped}$ = 4.5×10^{12} and total charges N_{total} = 3.2×10^{13}. To verify N_{total} we can also use the steady state space charge limited current value I_{SCLC}.

$$I_{SCLC} = J \cdot A = nev_d \cdot A = ne\frac{d}{t_{tran}} \cdot A \qquad (4.3)$$

Where J_{SCLC} is steady state space charge limited current density， A is the area of the device, v_d is the drift velocity of charge carriers, n is the charge carrier charge carrier density and d is the thickness of the organic semiconductor layer. Considering the number of charge carriers N=ndA,

$$N = \frac{t_{tran} \cdot I_{SCLC}}{e} \qquad (4.4)$$

The number of total charge carriers obtained using the equation 4.4 is N_{total} = 3.1×10^{13} which is in very good agreement with the number using equation 4.2. Considering the number of trapped charges, $N_{trapped}$ = 4.5×10^{12}, and the number of molecules in the first layer of Alq_3 in our device, N_{1st}= ~8.0x10^{12}, the presence of the trapped charge is

entirely consistent with a sheet of potential trap states due to the HINTS in the first molecular layer. In this scenario, this density of trap states is ～50% of the molecules in the 1st monolayer actually trapping injected holes. The number of total charges, obtained by Eq 4.2 and Eq 4.3 $N_{total(tran)}$ and $N_{total(SCLC)}$, the number of trapped charges $N_{trapped}$ and the number of first layer molecules N_{1s}, are summarized in table 4.1.

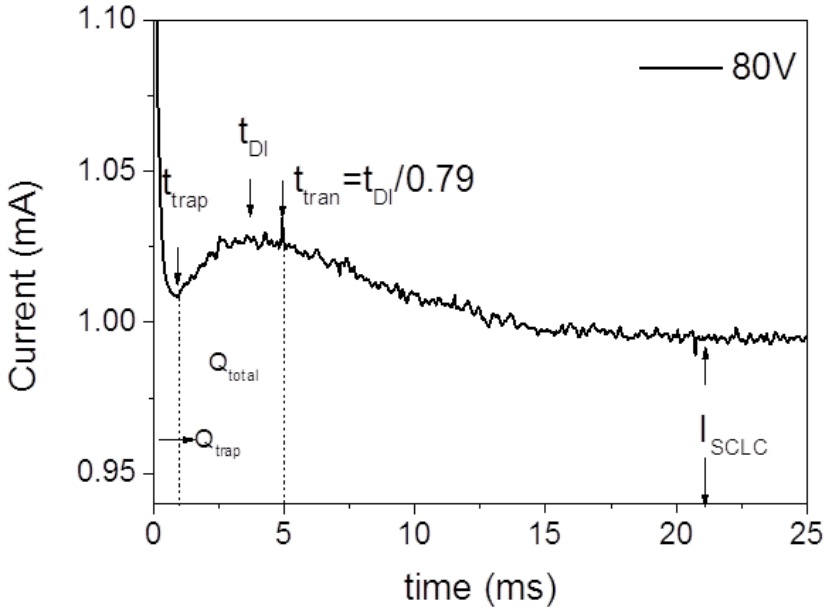

Figure 4.2: DI transient response obtained from a NiFe-Alq_3(500nm)-Al device with the applied bias of 80V

Table 4.1 Summary of $N_{total(tran)}$, $N_{total(SCLC)}$ $N_{trapped}$ and N_{1s} in the sample

$N_{total(tran)}$	$N_{total(SCLC)}$	$N_{trapped}$	N_{1s}
3.2×10^{13}	3.1×10^{13}	4.5×10^{12}	8.0×10^{12}

4.3 Temperature dependent DI

In the presence of trapping and de-trapping it is useful to investigate the temperature dependence of these phenomena, the thermal activation of de-trapping can provide, for example, an effective temperature dependent DI experiment allow for measuring both the thermal activation of steady state current and of the mobility (see figure 4.2)

4.3.1 Thermal activation energies

Considering the drift velocity to be $v_d = \mu E$ where μ is charge carrier mobility E is electric field, equation 4.3 can be rewritten as:

$$J = ne\mu E \qquad (4.5)$$

In contrast to the band transport in inorganic semiconductors, charge carrier transport in organic semiconductors is based on the thermally assisted hopping, where the current density J is thermally activated with two processes; temperature dependent charge carrier density *n* and temperature dependent charge carrier mobility μ. And we can use the simple thermal activation (Arrhenius) behaviour:

$$J = J_0 e^{-\frac{\Delta E_J}{k_B T}} \qquad (4.7a)$$

$$n = n_0 e^{-\frac{\Delta E_n}{k_B T}} \qquad (4.7b)$$

$$\mu = \mu_0 e^{-\frac{\Delta E_\mu}{k_B T}} \qquad (4.7c)$$

Where ΔE_J, ΔE_n and ΔE_μ are current density thermal activation energy, carrier density thermal activation energy and mobility thermal activation energy respectively, k_B is Boltzmann constant, and T is temperature. It is worth noting that, as Alq_3 is undoped and intrinsically semiconducting, the resulting charge carrier density should only depend on that injected from the anode. Therefore, charge carrier density n represents the injected charge carrier density and the activation energy ΔE_n should correspond to the injection barrier. Substituting J, n μ into equation 4.5, we obtain;

$$J = J_0 e^{-\frac{\Delta E_J}{k_B T}} = eEn_0\mu_0 e^{-\frac{\Delta E_{n+\Delta E_\mu}}{k_B T}} \quad (4.8)$$

Thus

$$\Delta E_J = \Delta E_n + \Delta E_\mu \quad (4.9)$$

As current density J and mobility μ can be obtained from DI, the thermal activation of n can be extracted by temperature dependent DI measurement.

4.3.2 NiFe anode device results

Temperature dependent DI measurements were employed on the same NiFe anode device (NiFe-Alq_3 (500nm)-Al) as used in chapter 3, with an applied bias of 78V. The DI transient response is shown in figure 4.3 measured at temperatures from 313K to

353K. In all the four cases, a clear transient peak appeared, followed by a typical trapping decay, which reduces to a steady state current. On heating the transient time t_{DI} reduced from 3ms to 1.8ms, while the steady state current increased from 3.9mA to 6.8mA. Temperatures below 313K cannot provide a DI transient peak but a trapping decay to the steady state current.

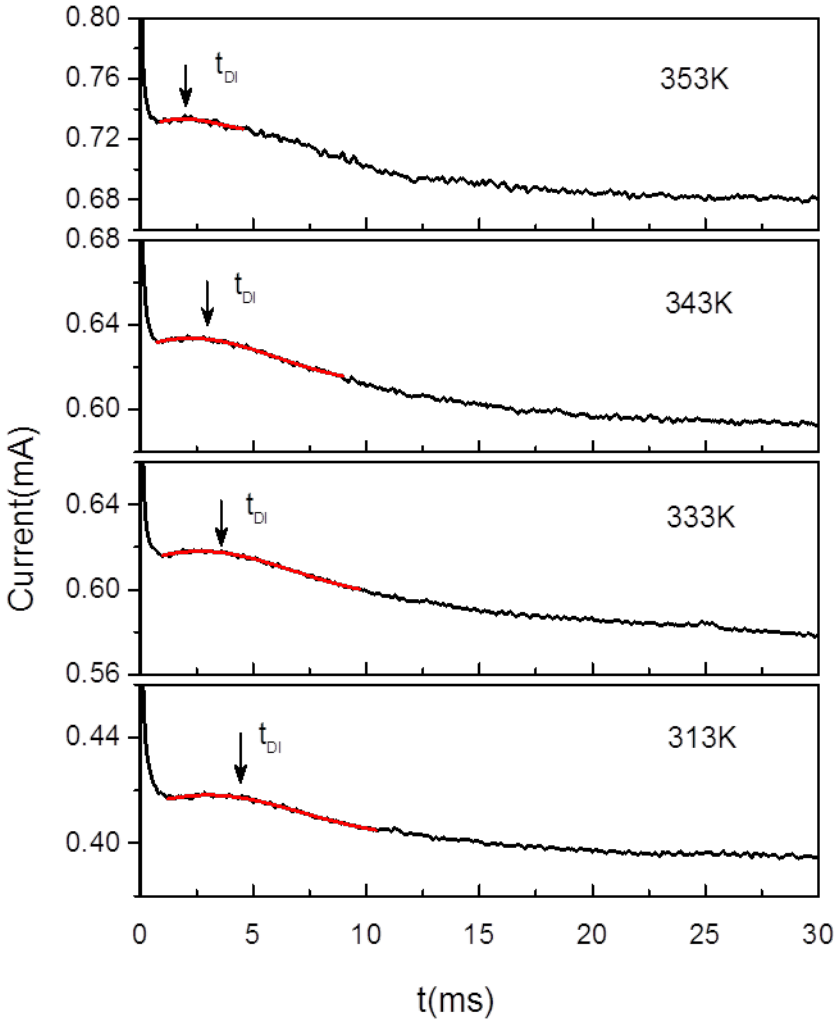

Figure 4.3: DI transient response of the NiFe-Alq_3(500nm)-Al device at the temperatures from 313K to 353K with the applied bias of 78V

Taking the natural logarithm of equations 4.7a and c, we obtain;

$$\ln J = \ln J_0 - \frac{\Delta E_J}{k_B T} \quad (4.10a)$$

$$\ln \mu = \ln \mu - \frac{\Delta E_\mu}{k_B T} \quad (4.10b)$$

As illustrated in figure 4.4, ΔE_J and ΔE_μ can be obtained from plots of J versus 1/T and μ versus 1/T using a log-linear scale from the results shown in figure 4.3.

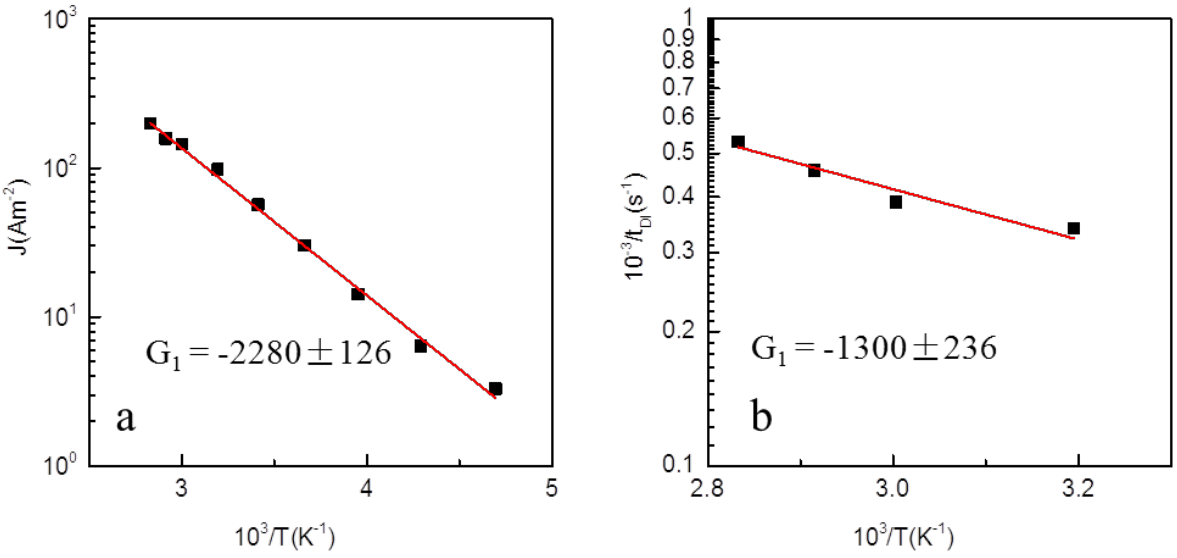

Figure 4.4: Arrhenius plots of (a) current density thermal activation and (b) mobility thermal activation in NiFe-Alq$_3$-Al device (10-3/t$_{DI}$∝μ). G1 and G2 represent the gradient of the plots

From figures 4.4 a and b, we obtain,

$$-\frac{\Delta E_J}{k_B} = -2280 \pm 126$$

and

$$-\frac{\Delta E_\mu}{k_B} = -1300 \pm 236$$

Hence:

$\Delta E_J = 198 \pm 11meV$

$\Delta E_\mu = 113 \pm 20meV$

$\Delta E_n = \Delta E_J - \Delta E_\mu = 85 \pm 23meV$

4.3.3 ITO anode device results

In order to obtain the activation energies in trap free devices, similar temperature dependent DI measurements were taken on the ITO anode device. Figure 4.5 shows the typical DI transient response for this device at the temperatures ranging from 333K to 373K with an applied bias 40V. At all temperatures, no trapping decay was observed, but only the fast RC displacement. The transient peak can be easily observed before reaching the steady state current in all cases, which is consistent with results obtained in chapter 3. The transient time t_{DI} reduced from 3ms to 2ms, while the current increased from 0.27mA to 0.52mA on heating.

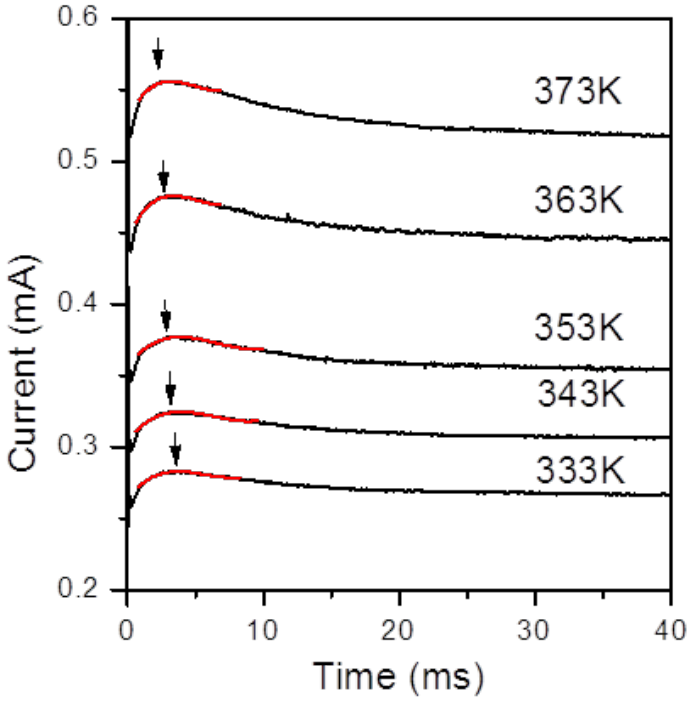

Figure 4.5: DI transient response for ITO-Alq_3(500nm)-Al device at the temperature (a) from 233K to 293K, (b) from 313K to 373K with the applied bias 40V

Arrhenius plots of the current and mobility are shown in figure 4.6, In the temperature range which is common for both NiFe and ITO samples, similar straight lines are obtained.

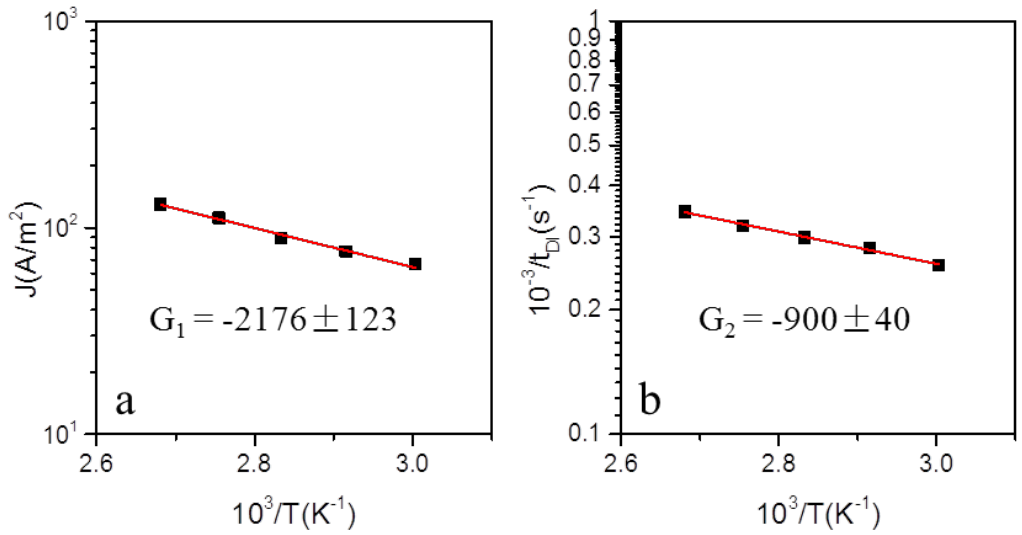

Figure 4.6: Arrhenius plots of of (a) current density and (b) mobility thermal activation in ITO-Alq$_3$-Al device($10^{-3}/t_{DI} \propto \mu$)., via plot of J versus 1/T and $1/t_{DI}$ versus 1/T. G_1 , G_2 G_3 and G_4 represent the gradient of the plots

From fig. 4.6 we have:

$$-\frac{\Delta E_J}{k_B} = -2176 \pm 123$$

$$-\frac{\Delta E_\mu}{k_B} = -900 \pm 40$$

Hence:

$$\Delta E_J = 187 \pm 11 meV$$

$$\Delta E_\mu = 78 \pm 3\ meV$$

$$\Delta E_n = \Delta E_J - \Delta E_\mu = 109 \pm 11 meV$$

Please note that, in subsequent discussion only data obtained over the same temperature range as the NiFe sample will be included.

4.3.4 Discussion

By using temperature dependent DI measurements, the thermal activation energies for current density, mobility and charge carrier density are obtained. The values are summarized in table 4.2. Given both NiFe and ITO devices are dominated by hole transport, as shown in chapter 3, the carrier density activation energy ΔE_n represents a hole thermal injection barrier at NiFe/Alq_3 and ITO/Alq_3 interfaces. In order to visualise the information summarized in table 4.2, we used the simple schematic shown in figure 4.7. Considering the fitting errors, both NiFe and ITO devices have a similar ΔEn, namely a similar hole injection barrier. As we know, the ITO is widely recognized as a good hole injector because of its high work function after plasma treatment (5.2eV to 5.7eV) [1-3], while for transition metals, their work function is ~4.9eV and the injection barrier between NiFe and Alq_3 is estimated to be ~1eV. The measured ~85meV energy barrier is much smaller than the theoretical estimation, which indicates a large energy level shift by the introduction of HINTS in the NiFe/Alq_3 interface.

As the charge carrier mobility is related to charge transport in the bulk of the device, the mobility activation energy should be dominated by bulk transport. As shown in table 4.2, NiFe and ITO devices present similar values of ΔE_μ as well. To investigate

hole transport in the bulk of the Alq_3, a pure transport measurement, temperature dependent ToF is employed and will be discussed in the next section.

Table 4.2 Summary of thermal activation energies for NiFe and ITO devices

Devices	$\Delta E_J(meV)$	$\Delta E_\mu(meV)$	$\Delta E_n(meV)$
NiFe	198±11	113±20	85±23
ITO	187±11	78±3	109±11

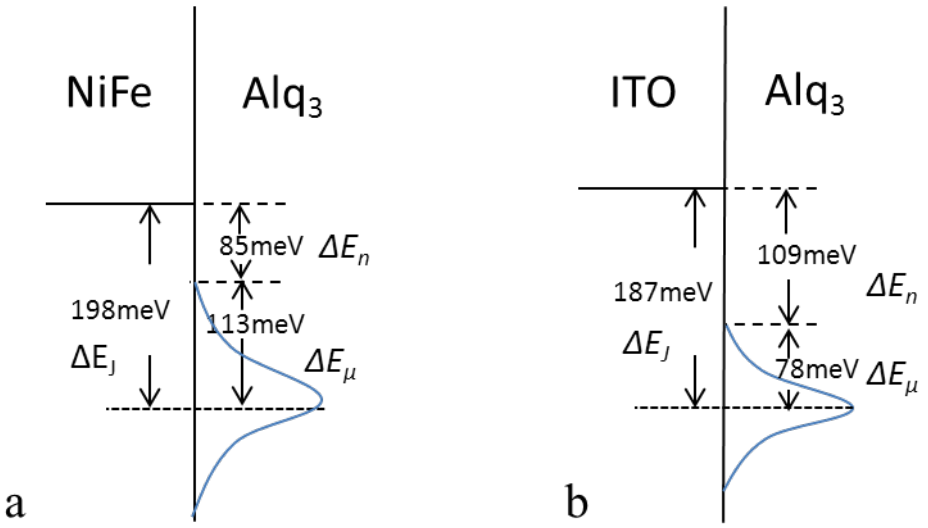

Figure 4.7: Schematic of the hole injection barrier of NiFe/Alq_3 and ITO/Alq_3 interface

4.4 Temperature dependent ToF

4.4.1 Results

In order to investigate thermal activation energy for hole transport in the bulk of Alq_3, temperature dependent ToF was taken on the same ITO device used in chapter 3. As

shown in figure 4.8, hole transport in Alq_3 is extremely dispersive, especially at low electric fields and low temperatures. The photocurrent transients are plotted in log-log scale. As described in chapter 2,the inflection points are obtained that represents the transient arrival time t_{tran} of holes. In figure 4.8, t_{tran} is scaling correctly as expected, with increasing temperature and electric field.

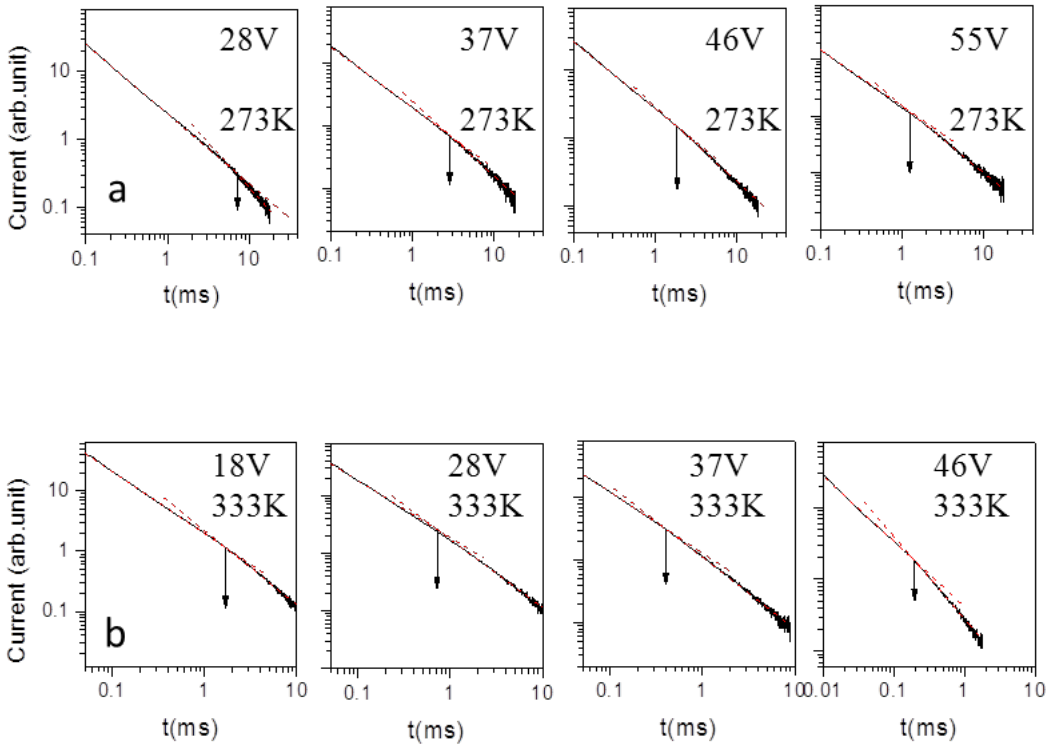

Figure 4.8: Photocurrent transients obtained using the ITO-Alq_3-Al device, with applying varying bias, (a) At the temperature 213K. (b) At the temperature 333K

Using Eq, 2.2 (chapter 2) the hole mobilities were calculated and plotted versus the square root of the electric field ($E^{1/2}$) for a range of temperatures in figure 4.9. For

each temperature clear Poole-Frenkel type behaviour can be observed, that is each data set lies approximately along a straight line.

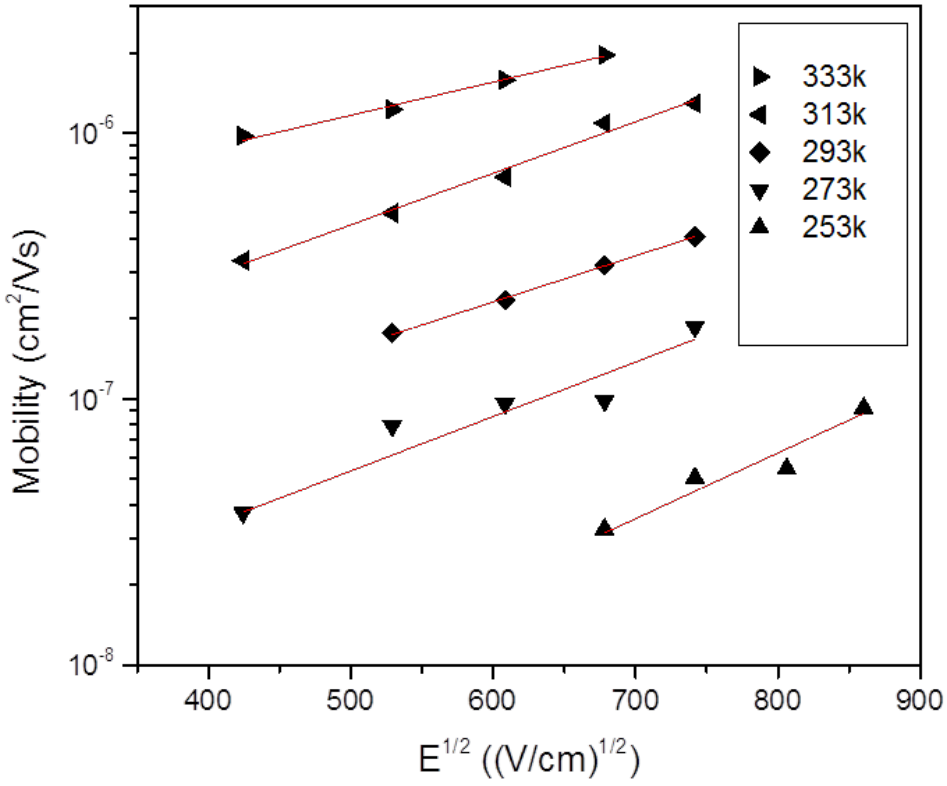

Figure 4.9: Poole-Frenkel plots of the measured hole mobility obtained in ITO-Alq_3-Al device

4.4.2 Analysis of results using GDM model

In order to investigate hole transport nature in Alq_3, in this section, the Gaussian Disorder Model (GDM), as introduced in chapter 1, is employed. As introduced in chapter 1, the energetic disorder (σ) and pre-factor mobility (μ_0) can be obtained from a plot of ln $\mu(E=0)$ as versus T^{-2} as shown in figure 4.10. The slope of the linear fit

corresponds to the energy disorder (σ) and the y-axis intercept to the pre-factor mobility (μ_0).

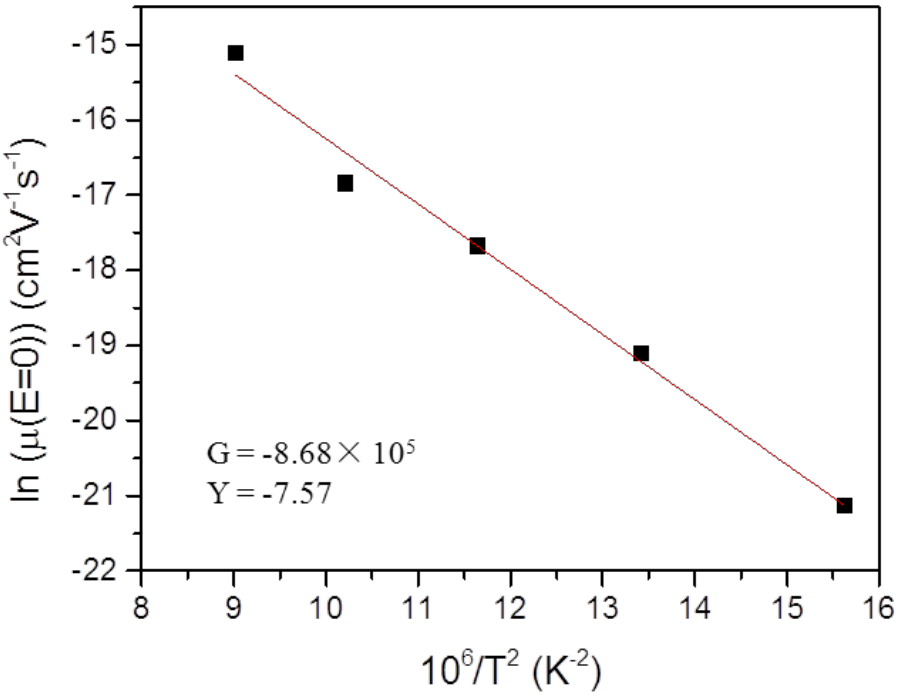

Figure 4.10: The logarithm of the zero field mobility versus T^{-2} for Alq_3. G and y represent the gradient and y-axis intercept of the linear fit respectively

From figure 4.10, we obtained

$$\left(\frac{2\sigma}{3k_B}\right)^2 = 8.68\times10^5 \pm 5.7\times10^4$$

$$ln\ \mu_0 = -7.5 \pm 0.7$$

Thus:

$$\sigma = 120 \pm 4\ meV$$

$$\mu_0 = (5.1 \pm 3.6)\times 10^{-4} cm^2/Vs$$

Values for spacial disorder (Σ) and empirical constant (C_0) are obtained via a plot of β versus $(\sigma/k_BT)^2$. The β is the Poole-Frenkel coefficient ($\frac{\partial ln\mu}{\partial\sqrt{E}}$) that represents the gradient of Poole-Frenkel plot in figure 4.9. By ignoring one abnormal point, an acceptable linear fit with gradient and y intercept is obtained in figure 4.11. The result of all the parameters is summarized in table 4.3.

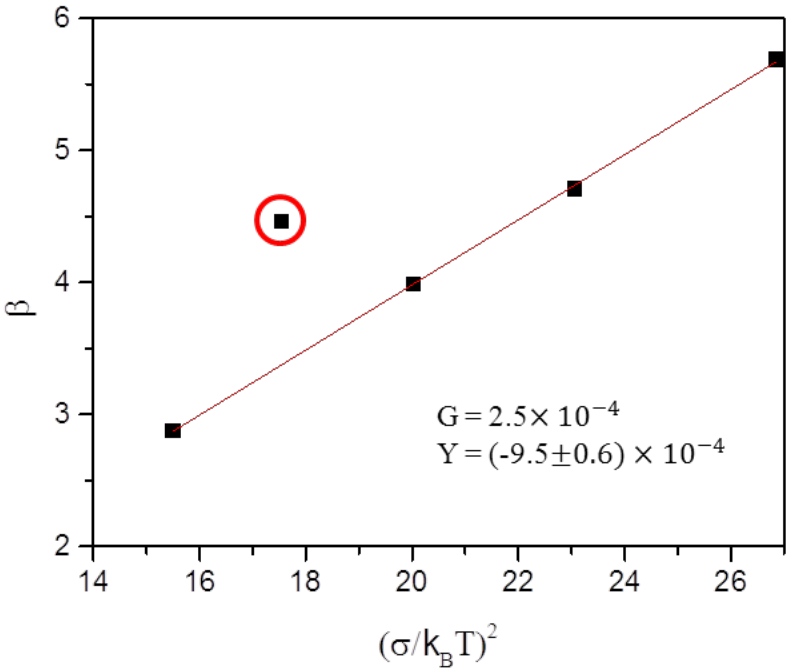

Figure 4.11: Extrapolation of spacial disorder (Σ) and empirical constant (C_0) for holes in Alq_3 via plot of β versus $(\sigma/k_BT)^2$, G and Y represent the gradient and y-axis intercept

Hence from figure 4.11:

$$C_0 = 2.5\times 10^{-4}\ (cm^{1/2}V)$$

$$-\Sigma^2 C_0 = (-9.5 \pm 0.6)\times 10^{-4} (cm^{1/2}V)$$

Thus

$$\Sigma = 1.9 \pm 0.1$$

Table 4.3. Summary of GDM parameters for holes in Alq_3.

Energetic Disorder σ (meV)	Spatial Disorder Σ	Pre-factor Mobility μ_0 ($cm^2\ V^{-1}s^{-1}$)	C_0 ($cm^{1/2}V$)
120±4	1.9±0.1	$(5.1 \pm 3.6)\times10^{-4}$	2.5×10^{-4}

4.5 Discussion and conclusion

By comparing with the DI data for NiFe and ITO, we found the evidence of HINTS in the NiFe and Alq_3 interface. In order to quantify the number of HINTS that are trapping the injected charges, we integrated the current with the respect to time over the trapping process and obtained the number of trapped charges that represent the number of HINTS. We are therefore able to estimate the charge stored in the HINTS. This charge must come from anode diffusion. As a result, a voltage drop must exist across the interface. Assuming an interface monolayer of ~1.4×10^{14} /cm^2 density (using a mass density of 1.2g/cm^3 and a molar mass of 459g/mol), given the area of the device (4mm^2) one can estimate the maximum amount of charge that can be present in the monolayer to be ~1.7×10^{-6} C. As shown in figure 4.12, the first molecular layer of Alq_3 with this sheet of excess electrons and the anode act as a

capacitor. Using Eq. 4.11, where C is the capacitance, d is the thickness of the capacitor, A is the area of the diode, V is the voltage across the capacitor, $\varepsilon_r = 3$ is the dielectric constant of the Alq_3 and ε_0 is the electric constant, the maximum potential difference of a few volts is obtained. This will effectively decrease the Fermi energy (or increase the working function) of NiFe electrode; hence the activation energy required for hole injection from NiFe into Alq_3 should be decreased.

$$q = VC = V \cdot \frac{\varepsilon_r \varepsilon_0 A}{d} \qquad 4.11a$$

Thus,

$$V = \frac{qd}{\varepsilon_r \varepsilon_0 A} \qquad 4.11b$$

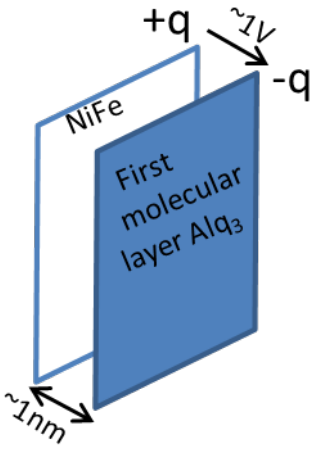

Figure 4.12: Schematic of a sheet of filled HINTS in the first molecular layer of Alq_3 acting as a capacitor that provide the voltage drop across the NiFe/Alq_3 interface

In order to obtain the thermal activation energy for hole injection the temperature dependent DI measurement was employed. By assuming the current density, charge

carrier mobility and charge carrier density are temperature dependent and follow simple Arrhenius behaviour, the thermal activation energy of these three parameters were obtained and summarized in table 4.2. As both current density activation energy ΔE_n and mobility activation energy ΔE_μ are obtained from DI data, the charge carrier density activation energy ΔE_n that represents charge carrier thermal injection barrier can be obtained. For the NiFe anode device ΔE_n is ~85meV. This small value is in disagreement with the theoretical estimation of the injection barrier ~1eV.

The implication of interfacial states on the charge transport and injection will depend of the position of the states relative to both the HOMO of the molecule and the Fermi level of the contact. It has been observed by Steil et al that there exist two states at the Alq3/Co interface[4]. One is unoccupied and lies above the cobalt Fermi level and the other is occupied and lies 0.8eV below the Co Fermi level. We propose the following mechanism, based on charge transfer, for the formation of an interface dipole between the electrode and organic. In figure 4.13b we represent the relative positions of the NiFe Fermi level and the Alq_3 HOMO in isolation and note that using literature values there ought to be an ~1eV difference between the two. If a pair of new states (HINTS) is produced when the NiFe and Alq_3 are brought into contact, one above and one below the NiFe Fermi level (as observed by Steil and co-workers in the case of Co), then the lower HINTS will be filled by electrons from the metal as it lies below the Fermi level of the contact (figure 4.13b). The process of electron transfer from the NiFe to the HINTS will lower the Fermi level of the NiFe and raise the energies of the

HINTS and Alq_3 HOMO (figure 4.13c). This process can continue as long as the HINTS remain energetically below the NiFe Fermi level, i.e. the interfacial potential due to any charge transfer is limited to $e\,\Delta V \leq E_{HINTS} - E_{Fermi}$. This process will result in a finite number of electrons being transferred into the HINTS, of total charge q. For an induced state above the Fermi level of the contact the state will, of course, remain empty. The occupied interfacial levels will form a dipole across the interface and result in a shift in the HOMO relative to the Fermi level of the contact (these effects are well understood in organic metal interfaces).

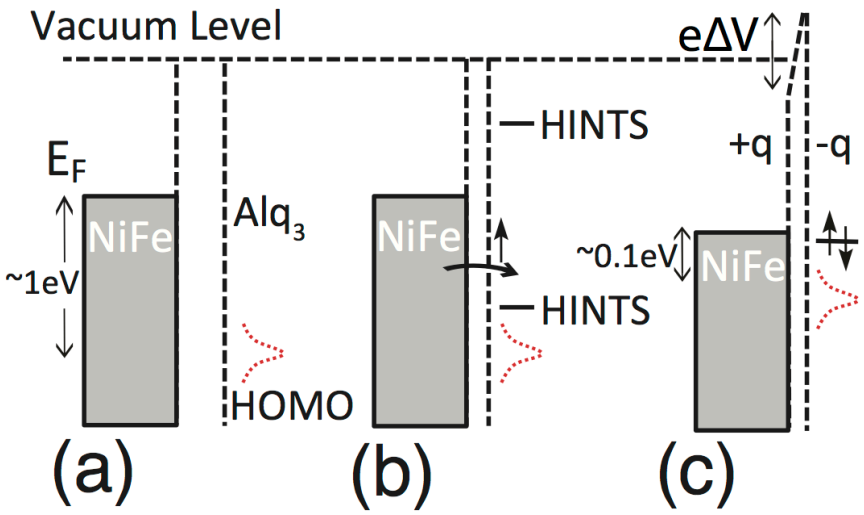

Figure 4.13: Energy diagrams showing the decrease of hole injection barrier due to the presence of HINTS in the first molecular layer of Alq_3

(a)NiFe/Alq_3 interface with no HINTS, (b) the introduction of HINTS and electron transfer, (c) reduction of hole injection barrier with the existence of occupied HINTS.

As shown in figure 4.14, in a real OSV, working at low temperature, with applied ~100mV, quantum tunnelling should dominate the hole injection. With the theoretical

estimated injection barrier, it is very hard to inject holes from ferromagnetic electrode into organic semiconductor. While the introduced electrons from the anode occupied in HINTS lead to a voltage drop ~1V at the interface that decreased the injection barrier. This result indicates the existence of HINTS decreased the injection barrier between FM/Alq_3 interfaces.

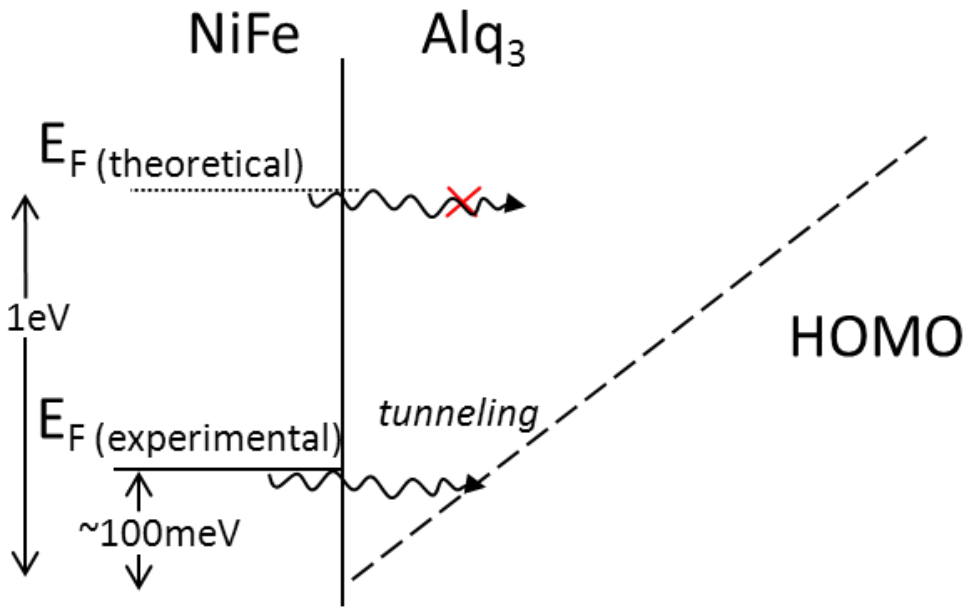

Figure 4.14: Energy diagrams of NiFe/Alq_3 interface in a OSV showing the quantum tunnelling process with applied bias

This also explains the trapping process of FM anode devices in the DI experiment. The holes are firstly injected and trapped in the HINTS, and result in the trapping decay (figure 4.15a). As soon as the HINTS are fully filled, the following injected

holes can hope to the subsequent sites leading to the space charge limited transport, which contribute to the appearance of transient peaks (figure 4.15a).

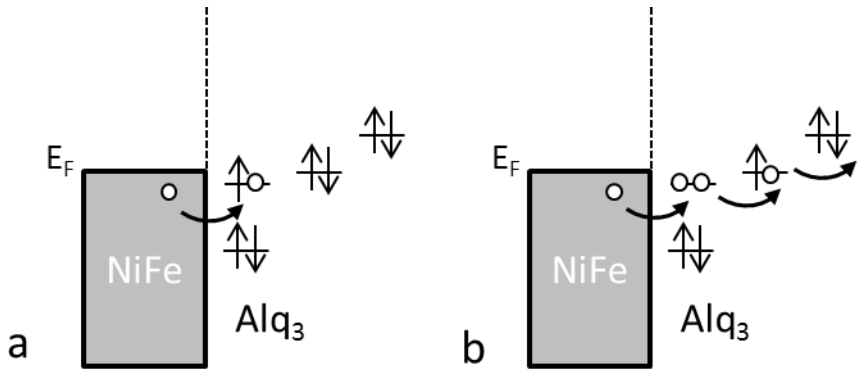

Figure 4.14: Energy diagrams showing the process of DI with trapping process, (a) trap filling, (b) trap filled and subsequent DI extraction

Finally hole transport in Alq_3 is investigated by temperature dependent ToF measurement and analysed with GDM model. The value for energetic disorder ~120meV is in good agreement with those reported in the literature for organic materials, typically range from 50meV to 150meV [5]. Usually the mobility activation energy corresponds, but is not necessary equal, to the energy disorder obtained from GDM, while the value of σ obtained for the ITO device agrees well with mobility activation energy obtained by DI in both ITO and NiFe devices.

References

[1] Y.S. Park, E. Kim, B. Hong, J. Lee, Characteristics of ITO films with oxygen plasma treatment for thin film solar cell applications, Mater. Res. Bull. , 48 (2013) 5115-5120.

[2] H.Z. Gao, L. He, Z.J. He, Z.B. Li, Z.H. Wu, W.H. Cheng, Q. Ai, X.X. Fan, Q.R. Ou, R.Q. Liang, Work Function Enhancement of Indium Tin Oxide via Oxygen Plasma Immersion Ion Implantation, Plasma Science & Technology, 15 (2013) 791-793.

[3] K. Sugiyama, H. Ishii, Y. Ouchi, K. Seki, Dependence of indium–tin–oxide work function on surface cleaning method as studied by ultraviolet and x-ray photoemission spectroscopies, J. Appl. Phys. , 87 (2000) 295-298.

[4] S. Steil, N. Großmann, M. Laux, A. Ruffing, D. Steil, M. Wiesenmayer, S. Mathias, O.L.A. Monti, M. Cinchetti, M. Aeschlimann, Spin-dependent trapping of electrons at spinterfaces, Nat. Phys. , 9 (2013) 242-247.

[5] H. Bässler, Charge transport in disordered organic photoconductors a Monte Carlo simulation study, physica status solidi (b), 175 (1993) 15-56.

Chapter 5 Conclusions and future work

This thesis aims to understand charge carriers injection from ferromagnetic materials (FMs) into organic semiconductors (OSCs) in OSVs. Motivated by comparing the electronic properties with OLED one of the other OSC based devices, the work has been divided into two parts: identifying the type of charge carriers that dominates injection and transport in OSVs, and investigating charge carriers injection with the assistance of interface sates or HINTS in FM/OSC interfaces.

In chapter 3, modified OLEDs with FM cathode were fabricated, the absence of light emitting comparing with the standard OLED, indicates FM contacts are poor electron injectors and Alq_3 is capable of hole transport. This result contradicted the previous understanding of Alq_3, that has been widely recognized as an 'n type semiconductor' and ignored the fundamental difference of semiconducting nature between traditional inorganic semiconductors and organic semiconductors.

In order to identify the type of injected charge carriers in OSVs, mobility measurement techniques ToF and DI were employed. ToF is measuring the mobility of photocurrent introduced in the device. By choosing the irradiation electrode, the type of introduced charge carriers is selected. From the dispersive photocurrent transient in Alq_3, the upper limit of mobilities of both electrons and holes were obtained. The mobility of electrons is about two orders of magnitude higher than that of electrons, which well agrees with literature results using either the same or other mobility measurement techniques. However, the preferred type of charge carriers

been injected into a OSC is not decided by its higher transport mobility in this OSC but the lower injection barrier of this type of charge carriers between electrodes and OSC spacer. Therefore DI was used to measure the mobility of injected charge carriers from FM electrodes into OSC Alq_3. DI is a space charge limited charge carrier mobility measurement, which is only valid when sufficient charge carriers are injected. Same as ITO anode sample (ITO-Alq_3-Al), for the FM anode (FM-Alq_3-Al) devices with diode like IV characteristics, the DI transient peaks were observed only when forward bias was applied (positive bias on ITO or FM electrode). This indicates mobilities of either holes injected form anode or electrons injected from cathode were obtained. Comparing the DI mobility with hole and electron mobilities obtained from ToF measurements， the conclusion that it is holes that dominate the charge carrier injection from FM into OSC spacer is finally made. This conclusion was further confirmed by the DI measurement on real OSV structure devices with two FM electrodes.

Even though the DI mobilities obtained from both ITO-Alq_3-Al and FM-Alq_3-Al devices were hole mobilities, an obvious difference in the DI transient response was observed (figure 4.1). In the ITO anode devices, typical trap-free DI transient responses were obtained that transient peaks appeared followed by sharp RC displacements, while for the FM anode samples, long-time decays (two orders of magnitude larger than RC time constant) which are due to hole trapping were observed. As these two types of devices only differ in their bottom anode, the

observation of trapping decay in the FM anode devices indicate the introduction of HINTS the in the FM/Alq_3 interfaces acting as the trapping states. The HINTS are originated from chemical absorption between the first layer of Alq_3 molecules and surface of FM atoms. The number of trapped charges estimated in the HINTS is equivalent to a potential difference of over one volt between the first layer of Alq_3 and anode. This potential drop can effectively decreased the hole injection barrier in FM/Alq_3 interface that enables the OSV working at low bias.

In order to support this assumption, temperature dependent DI were used to extract the value of carrier density thermal activation energy $\Delta E_{\mu.}$ As injection is the only source that contributes carrier density without doping in OSC. ΔE_{μ} represents the hole injection barrier. While the value of the hole injection barrier between NiFe/Alq_3 is theoretically estimated to be ~1eV, the obtained ~85meV of ΔE_{μ} in NiFe anode devices indicate that the barrier is effectively reduced in the real devices. This ~1eV reduction is in agreement with our previous calculation that the sheet of excess charges stored in HINTS act like a capacitor that decreased the Fermi level of Fe electrode. Furthermore, this value of energy barrier is also consistent with the fact that the OSVs are normally working at low bias (~100meV) and low temperature, where holes are theoretically estimated to be hardly injected via either tunnelling or thermal injection.

In summary, by using several complementary techniques, we proved that it is the

holes that dominated the spin transport in the Alq_3 based OSVs. The presence of HINTS reduced the hole injection barrier between FM/Alq_3 interfaces that enables Alq_3 based OSVs working at low bias.

In this thesis, we only studied OSVs with transition metals and their alloys as the electrodes, and small molecule OSC Alq_3 as the spacer. Half metal oxide FM material such as LSMO and other OSCs including polymers are worth investigating using similar techniques.

Further more, the HINTS investigated in this thesis has been recognized as the spin filter, which prefer to trap charges with certain spin orientation. In this case, it is interesting if we can use DI to investigate the trapping charge with different spin orientation with an applied magnetic field.